Institut für Theoretische Physik III
Universität Stuttgart
Pfaffenwaldring 57
70550 Stuttgart

Quantum many-body physics with strongly interacting Rydberg atoms

Von der Fakultät Mathematik und Physik der Universität Stuttgart zur Erlangung der Würde eines Doktors der Naturwissenschaften (Dr. rer. nat.) genehmigte Abhandlung

Vorgelegt von

Hendrik Weimer

aus Stuttgart

Hauptberichter:	Prof. Dr. Hans Peter Büchler
Mitberichter:	Prof. Dr. Günter Mahler
Tag der mündlichen Prüfung:	21. Juli 2010

Institut für Theoretische Physik der Universität Stuttgart

2010

(Dissertation Universität Stuttgart)

List of previous publications

[1] H. Weimer and H. P. Büchler. Two-stage melting of strongly interacting rydberg atoms in one-dimensional lattices. *submitted to Phys. Rev. Lett.* (2010). ArXiv:10xx.xxxx.

[2] J. Honer, H. Weimer, T. Pfau, and H. P. Büchler. Collective many-body interaction in rydberg dressed atoms. *submitted to Phys. Rev. Lett.* (2010). ArXiv:1004.2499.

[3] H. Weimer, M. Müller, I. Lesanovsky, P. Zoller, and H. P. Büchler. A rydberg quantum simulator. *Nature Phys.*, **6**, 382 (2010).

[4] R. Löw, H. Weimer, U. Krohn, R. Heidemann, V. Bendkowsky, B. Butscher, H. P. Büchler, and T. Pfau. Universal scaling in a strongly interacting rydberg gas. *Phys Rev. A*, **80**, 033422 (2009).

[5] U. Raitzsch, R. Heidemann, H. Weimer, B. Butscher, P. Kollmann, R. Löw, H. P. Büchler, and T. Pfau. Investigation of dephasing rates in an interacting rydberg gas. *New J. Phys.*, **11**, 055014 (2009).

[6] M. Müller, I. Lesanovsky, H. Weimer, H. P. Büchler, and P. Zoller. Mesoscopic rydberg gate based on electromagnetically induced transparency. *Phys. Rev. Lett.*, **102**, 170502 (2009).

[7] H. Weimer, R. Löw, T. Pfau, and H. P. Büchler. Quantum critical behavior in strongly interacting rydberg gases. *Phys. Rev. Lett.*, **101**, 250601 (2008).

Contents

Part I

Introduction

> If you wish to make an apple pie from scratch, you must first invent the universe.
>
> Carl Sagan

1 Preliminary remarks

Acheiving coherent control of many-body quantum systems is currently one of the most active areas of research in both atomic and condensed matter physics. Towards the long-term goal of scalable quantum computing [Nielsen2000] there are many other intermediate milestones to reach until complete coherent control is reached.

An important step on the way to controlled coherent manipulation of quantum systems is the possibility to tailor interaction potentials. Currently, the prevalent form of interaction studied in ultra-cold atoms is a short-range contact interaction that can be widely tuned via Feshbach resonances [Bloch2008]. However, long-range dipolar forces found between atoms with high magnetic moments [Stuhler2005] or polar molecules [Ni2008] are rapidly gaining traction. There, the interactions take place within the atomic ground state manifold, resulting in particularly stable experimental setups with lifetimes up to several seconds.

Highly excited Rydberg atoms offer a different road to controlling the form of interaction potentials. Exciting ultra-cold atoms to Rydberg states allows for an enormous degree in tunability of their atomic properties and interaction strengths [Gallagher1994]. The dramatic scaling of the van der Waals or dipole potentials with the principal quantum number can result in interaction energies up to several GHz, which by far exceeds any other energy scale at microkelvin temperatures. The intrinsic decoherence mechanism due to radiative decay of the Rydberg state requires experiments to be done on a shorter timescale.

Rydberg atoms can be created coherently by photoexcitation using a two-photon process. However, for two spatially close atoms only one can be excited as the strong Rydberg-Rydberg interaction shifts the doubly excited state out of resonance. This phenomenon is known as the "dipole blockade" and has been proposed as a key ingredient for quantum information processing with Rydberg atoms [Jaksch2000, Lukin2001].

For coherent applications the "frozen Rydberg" regime [Anderson1998] is of special interest; here both motion of the atoms and radiative decay of the Rydberg states can be neglected on the typical timescale of an experiment. Rapid experimental progress in recent years has pushed the field from single-atom physics into an area where strong many-body effects are impor-

tant [Heidemann2007, Younge2009, Pritchard2009, Schempp2010] and where new theoretical concepts and tools are required, taking elements of different areas such as atomic physics, condensed matter theory, quantum optics and quantum information theory. At the same time the advances in the coherent manipulation of Rydberg atoms create novel possibilities for engineering complex many-body states.

This thesis covers both aspects. Following the intoductory remarks of Part I, in Part II a thermodynamic interpretation of the excitation dynamics in strongly interacting Rydberg gases is presented. Within mean-field theory it is possible to describe both the ground state properties and the dynamics of the system after a sudden switching on of the excitation lasers. The obtained effective description is in excellent agreement both with numerical simulations of small-scale systems and with experimental observations. The results open the possibility of realizing novel crystalline phases consisting of Rydberg excitations, which is investigated in detail for one-dimensional lattice systems, where two different kinds of quantum melting transitions can be studied.

Part III discusses the systematic creation of strongly correlated states using the strong interactions found between Rydberg atoms. A mesoscopic quantum gate for the single step preparation of highly entangled states is presented. This gate is then used to construct a universal quantum simulator for many-body spin interactions, allowing to study exotic quantum phases such as a quantum spin liquid. The presented approach is not limited to the simulation of coherent Hamiltonian dynamics, but also allows for a dissipative preparation of strongly correlated ground states. The combination of both coherent and dissipative dynamics allows for an investigation of the complete phase diagram of the simulated system via adiabatic variations of the simulated Hamiltonian. Finally, Part IV presents a summary of the results and an outlook towards future research.

2 Basic concepts

2.1 Rydberg atoms

Rydberg atoms are atoms with one or more electrons in a highly excited state, having a principle quantum number $n^* \geq 10$ [Gallagher1994]. In such a state close to the ionization threshold the electron is only very loosely bound, resulting in extreme properties of Rydberg atoms.

2.1.1 General properties

In many situations it is sufficient to treat the Rydberg atom as hydrogenic. However, the inner electrons do not perfectly shield the electric charge of the nucleus. A phenomenological but very successful approach is quantum defect theory, which essentially replaces the principle quantum number of the hydrogen problem by a non-integer effective quantum number n^*. The difference accouting for the quantum defect δ only depends on the element and the angular momentum quantum numbers. A few values of δ are shown in Tab. 2.1. Solving the Schrödinger equation for non-integer quantum numbers is possible using semiclassical approximation methods.

Nevertheless, the general scaling properties of Rydberg atoms can be derived by treating them as hydrogenic. The scaling of some important properties for studying Rydberg atoms is shown in Tab. 2.2.

Atom	State	δ
^{7}Li	ns	0.399
	np	0.473
	nd	0.002
^{85}Rb	$ns_{1/2}$	3.13
	$np_{3/2}$	2.64
	nd	1.35

Table 2.1: Values of the quantum defect δ for different elements and angular momentum quantum numbers [Gallagher1994].

Property	$(n^*)^x$	^{87}Rb(43s)
Binding energy	$(n^*)^{-2}$	2.07 THz
Level spacing	$(n^*)^{-3}$	110 GHz
Orbital radius	$(n^*)^2$	2380 a_0
Polarizability	$(n^*)^7$	8.06 MHz $(\mathrm{V/cm})^{-2}$

Table 2.2: Scaling behavior of selected properties of Rydberg atoms with the effective quantum number n^* with numerical values for the $43s$ state of ^{87}Rb [Heidemann2008a].

Dipole matrix elements Calculating the dipole matrix elements between a Rydberg state and a low-lying level requires some more care. The eigenfunctions of the hydrogen problem are given by [Merzbacher1970]

$$\begin{aligned}\psi(r,\vartheta,\varphi) &= \sqrt{\left(\frac{2}{na_0}\right)^3 \frac{(n-l-1)!}{2n[(n+l)!]^3}}\exp(-r/na_0)(2r/na_0)^l \\ &\quad \times L_{n-l-1}^{2l+1}(2r/na_0)Y_{lm}(\vartheta,\varphi). \end{aligned} \tag{2.1}$$

For s states with $l = 0$ the normalization of the associated Laguerre polynomials leads to

$$L_{n-1}^{2l+1}(0) = (n-1)!. \tag{2.2}$$

For large $n \gg n'$ the dipole matix element $\langle n'p|er|ns\rangle$ essentially depends on the value of the Rydberg wave function at the origin as the overlap is exponentially suppressed at larger distances. Consequently, its scaling takes the form

$$\langle n'p|er|ns\rangle \sim (n^*)^{-3/2}. \tag{2.3}$$

Natural lifetime The radiative decay of a Rydberg state nl can be understood using Fermi's golden rule, which couples the transition rate γ to the corresponding dipole matrix element and the density of states in the final level,

$$\gamma_{nl,n'l'} = \frac{2\pi}{\hbar}|\langle nl|V|n'l'\rangle|^2 g(n'l'). \tag{2.4}$$

The density of states increases quadratically with frequency of the emitted photon [Walls1994]. Furthermore the dipole operator depends on the photon frequency like $V \sim \sqrt{\omega}$, thus the most probable decay channel is to the energetically lowest state that is allowed by selection rules. For such a transition we

have seen that $V \sim (n^*)^{3/2}$, and consequently the lifetime $\tau = 1/\gamma$ scales like $\tau \sim (n^*)^3$, with the value for the $|43s\rangle$ state being $\tau = 99\,\mathrm{s}$ [Heidemann2008a].

At finite temperatures there is also a decay mechanism via the absorption and emission of blackbody radiation photons [Gallagher1994]. The blackbody limited lifetime τ_{bb} scales quadratically in n^* according to

$$\tau_{bb} = \frac{3(n^*)^2}{4\alpha^3 k_B T}, \tag{2.5}$$

where $\alpha \approx 1/137$ is the fine structure constant.

2.1.2 Interactions

Interactions between two Rydberg atoms are mostly governed by couplings to the nearest state. Hence, two atoms in the state $|n_1 s, n_2 s\rangle$ predominantly couple to the states $|n_1 p, n_2 p\rangle$, $|n_1 - 1s, n_2 p\rangle$, and $|n_1 s, n_2 - 1p\rangle$. If the interparticle separation R is much larger then the LeRoy radius

$$R_{LR} = 2\left(\sqrt{\langle n_1 s|r^2|n_1 s\rangle} + \sqrt{\langle n_2 s|r^2|n_2 s\rangle}\right), \tag{2.6}$$

then the overlap of the wave function may be neglected [LeRoy1974]. In this case one may write the interaction energy as a power series in $1/R$,

$$V(R) = \sum_{k=1}^{\infty} \frac{C_k}{R^k}. \tag{2.7}$$

In the following we will concentrate on the case where $n_1 = n_2 \equiv n$.

As Rydberg atoms are neutral objects the first nonzero term is the C_3 coefficient, which is related to the corresponding dipole matrix element according to

$$C_3 = \frac{1}{4\pi\varepsilon_0}|\langle ns|er|n'p\rangle|^2, \tag{2.8}$$

which can be computed numerically within quantum defect theory [Singer2005]. In a two-level approximation the interaction Hamiltonian reads

$$H = \begin{pmatrix} \delta_F & \frac{C_3}{R^3}\sqrt{D_\varphi} \\ \frac{C_3}{R^3}\sqrt{D_\varphi} & 0 \end{pmatrix}, \tag{2.9}$$

where the Förster defect δ_F accounts for the energy difference of the two states and D_φ contains the angular momentum properties [Walker2008]. The eigenvalues are given by

$$V_\pm(R) = \frac{\delta_F}{2} \pm \frac{1}{2}\sqrt{\delta^2 + 4\frac{C_3^2 D_\varphi}{R^6}}. \tag{2.10}$$

At large distances the Förster defect δ will be the dominant energy scale and the second eigenvalue reduces to

$$V_-(R) = -\frac{C_3^2 D_\varphi}{\delta R^6}, \tag{2.11}$$

which describes a van der Waals interaction. Note that δ may be negative for certain combination of states, in this case the van der Waals interaction is repulsive. Consequently there is is a crossover from a resonant dipole interaction at short distances to a van der Waals interaction at large distances taking place at $R_c = \sqrt[6]{4C_3^2/\delta^2}$. The behavior of the interaction energy depending on the interatomic separation is shown in Fig. 2.1.

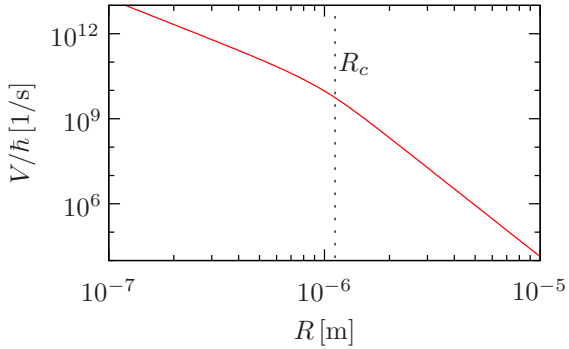

Figure 2.1: Dependence of the interaction potential V on the interatomic separation R for the $|43s\rangle$ state. The crossover from a dipolar to a van der Waals interaction takes place at R_c.

The van der Waals interaction found at large distances scales dramatically with the principle quantum number like $C_6 \sim n^{11}$. For Rubidium the interaction is always repulsive for sufficiently large n [Singer2005].

2.1.3 Coherent production

Rydberg excitations are created in a fully coherent way via two-photon processes. The excitation lasers are far detuned from the intermediate P level,

such that it can be adiabatically eliminated, see Fig. 2.2. Consequently, the internal structure of the atoms can be effectively reduced to a single hyperfine ground state $|g\rangle$ and a single Rydberg level $|e\rangle$, giving rise to a spin 1/2 description. In the following we identify the spin up state with the Rydberg state, $|\uparrow\rangle = |e\rangle$ and analogously $|\downarrow\rangle = |g\rangle$.

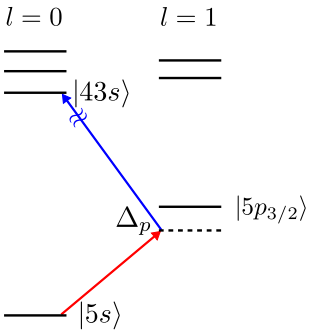

Figure 2.2: Level scheme for the coherent production of Rydberg atoms for ^{87}Rb. The first photon couples the atomic $|5s\rangle$ ground state to the intermediate $|5p_{3/2}\rangle$ state, which is coupled to a Rydberg state (here: $|43s\rangle$). The frequencies of the excitation photons are chosen such that the detuning Δ_p from the intermediate level is large; hence it can be adiabatically eliminated.

2.2 Phase transitions

The basic idea behind classical thermodynamics is to describe the properties of a macroscopic system with a large number of particles using only a few relevant observables such as energy, temperature, or volume. Depending on the values of these quantities the same system may show dramatically different macroscopic behavior, which allows us to classify the system in terms of different thermodynamic phases. Often one phase is in a more ordered state than another, e.g., in a crystal the atoms are arranged in a regular pattern that is not present in the liquid phase.

2.2.1 Classical and quantum phase transitions

Classical systems In a classical thermodynamics a phase transition occurs when the free energy

$$F = E - TS \tag{2.12}$$

shows nonanalytic behavior. In thermal equilibrium the realized macrostate with internal energy E and entropy S is chosen such that F is minimal. The competition between energy and entropy can be controlled by changing the temperature, which can lead to qualitatively different behavior in different phases. If we consider a transition from an ordered to a disorderd phase the transitions happens when the thermal fluctuations overcome the energy cost associated with breaking the ordered state. In this sense we can speak of classical phase transitions being driven by thermal fluctuations.

Quantum systems In quantum systems at $T = 0$ there are no thermal fluctuations. Hence, the only possibility for a phase transition to occur is when the energy of the system itself is nonanalytic. As at $T = 0$ the system is in its ground state a quantum phase transition occurs when the macroscopic observables of the ground state change due to a parameter change in the Hamiltonian.

There are basically two ways in which a quantum phase transition can take place. Let us consider a Hamiltonian of the form

$$H = H_0 + \lambda H_1. \tag{2.13}$$

When λ passes some critical value λ_c the transition will take place. The first possibility is when H_0 and H_1 commute, and we thus have a real level crossing between the macroscopically different ground states. The other possibility

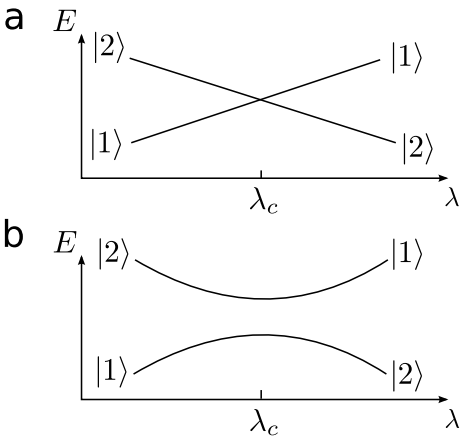

Figure 2.3: Energy levels across a quantum phase transition at $\lambda = \lambda_c$. (a) Level crossing. (b) Avoided crossing.

occurs when $[H_0, H_1] \neq 0$, then there is an avoided crossing with an energy gap that vanishes for $\lambda = \lambda_c$ in the thermodynamic limit [Sachdev1999]. Then, we may speak of the transition being driven by quantum fluctuations. Fig. 2.3 shows a graphical sketch of the two different realizations.

There is also the possibility of a combination of classical and quantum phase transitions within the same phase diagram, see Fig. 2.4. A prominent example is the Bose-Hubbard model [Fisher1989], which has been studied extensively in cold atomic gases both from a theroretical and experimental perspective [Jaksch1998, Greiner2002]. At low temperatures and weak interparticle repulsion the system is in a superfluid phase, and the zero temperature phase diagram exhibits a continuous phase transition to a Mott insulator for stronger interactions. At higher temperatures, the Mott insulator is continuously connected to a normal liquid.

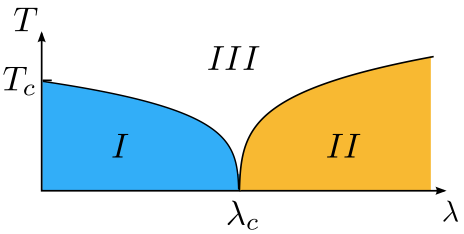

Figure 2.4: Combination of classical and quantum phase transitions with three distinct phases. At zero temperature there is a quantum phase transition between two quantum phases I and II, while at finite temperatures a transition to the normal phase III is present.

2.2.2 Classification

While any phase transition, classical or quantum, is accompanied by non-analytic behavior of the free energy F, there are important aspects where the nature of phase transitions can differ in a substantial way. Considering a system with generalized couplings $\{K_i\}$, then the F is always a continous function of all K_i. Phase transitions fall into two different classes related to the nature of the non-analycity of F [Goldenfeld1992]:

1. One or more $\partial F/\partial K_i$ is discontinuous across the phase boundary. Then the transition is called a "first-order phase transition".

2. When all $\partial F/\partial K_i$ are continuous across the phase boundary the transistion is refered to as a "continuous phase transition". Often one or

more of the second derivatives $\partial^2 F/\partial K_i^2$ is discontinuous, but this is not neccessarily the case. Sometimes these transitions are also called "second order phase transitions" because of this.

It might be tempting to associate the level crossing of Fig. 2.3 with a first order transition and the avoided crossing with a continuous transition. However, as Fig. 2.3 illustrates, this is not the case. A series of level crossing can lead to a continuous transition if the distance between the crossing points becomes infinitesimally small in the thermodynamic limit and the envelope of the crossings has a continuous derivative at the critical point.

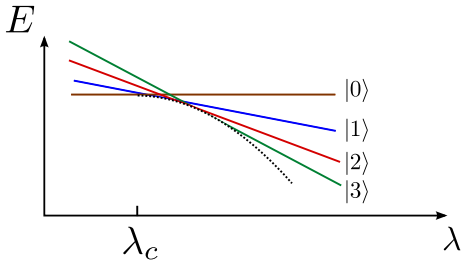

Figure 2.5: Continuous quantum phase transition by a series of level crossings. The envelope shown as a dotted line has a continuous derivative at $\lambda = \lambda_c$

As already mentioned, phase transition often involve a transformation from a disordered to an ordered state, which is a reduction of symmetry of the system. Because of this reduction an additional parameter is needed to describe the properties of the ordered phase [Huang1987]. This parameter is called "order parameter" as it quantifies the amount of order present in the system.

While the ordered phase is often characterized by an extensive thermodynamic variable like the magnetization, there are exceptions to this rule. In two-dimensional systems, where the Mermin-Wagner theorem forbids the continuous breaking of a symmetry, there is the possibility of a Kosterlitz-Thouless transition, where the correlation functions decay algebraic in one phase and exponentially in the other [Kosterlitz1973]. The absence of an order parameter implies that all derivatives of F have to be continuous. Hence, these transitions are sometimes named "infinite order transitions".

The presence of a phase transition without a local order parameter can be further generalized towards lattice gauge theories, where the Hamiltonian is invariant under quasi-local symmetry transformations [Kogut1979]. There, thedifferent phases are characterized in the way elementary excitations interact. One can have a confined phase with an interaction potential increasing

with distance as in quark physics. In the deconfined phase the excitations are asymptotically free, e.g., they exhibit an interaction potential that decays with distance of the excitations like a coulombic $1/r$ power law.

2.2.3 Universality classes

Near the critical point of a continuous transition the system becomes scale invariant. This means that microscopic details of the system become irrelevant, and the macroscopic behavior is dominated by its long-range physics, associated with a diverging length scale ξ. Mathematically, a function $f(s)$ is called scale-invariant, if it satisfies the equation

$$f(\lambda s) = c(\lambda) f(s). \tag{2.14}$$

Performing a series expansion around $\lambda = 1$ given by

$$f(\lambda s) = f(s) + \frac{\mathrm{d}f}{\mathrm{d}s} s(\lambda - 1) + O\left((\lambda - 1)^2\right) = c(\lambda) f(s), \tag{2.15}$$

one can see that the resulting differential equations has solutions in terms of power laws $f \sim s^\kappa$ with $c(\lambda) = \lambda^\kappa$. Hence, near the critical point all observables can be described by power laws of the diverging scale ξ. Since ξ itself depends on the generalized couplings K_i, we may equally express the scaling of an observable O as

$$O = O_0 |K - K_c|^\kappa. \tag{2.16}$$

The critical exponent κ does not need to be a simple rational number. However, it was discovered that critical exponents are identical for systems completely different on the microscopic level. For example, the scaling with temperature of both the magnitization near the ferromagnetic transition and the density difference between the liquid and gas phase have the same highly nontrivial exponent. This equivalence allows for the classification of phase transitions into universality classes with identical critical exponents, while the physical mechanism behind it became apparent with the advent of the renormalization group [Fisher1998]. Generally speaking, the universality class only depends on the dimension and symmetries of the order parameter, the spatial dimension of the system and the range of interparticle forces. The Ising universality class for the fermomagnetic and liquid-gas transitions mentioned above has a scalar order parameter with a Z_2 symmetry in three spatial dimensions with short-range forces.

For each universality class one can specify two critical dimensions, where the properties of the phase transition change dramatically [Goldenfeld1992].

Above the upper critical dimension mean-field theory predicts the correct critical exponents. Below the lower critical dimension the phase transition disappears as fluctuations are stronger in low-dimensional systems and can lead to a breakdown of the ordered phase.

The concept of universality is not limited to phase transitions. Likewise, it is found to occur in different fields of physics [Goldenfeld1992], biology [West2004], and economics [Stanley1996], particularly in dynamical systems. In all these areas universality serves as a powerful tool allowing to describe the behavior of a system without actually knowing all the microscopic details of its state.

2.3 Quantum master equations

2.3.1 Open quantum systems

In fully coherent systems the dynamics is governed by the Schrödinger equation,

$$\mathrm{i}\hbar\frac{\mathrm{d}}{\mathrm{d}t}|\psi(t)\rangle = H|\psi(t)\rangle. \tag{2.17}$$

By unwanted or controlled interactions with external degrees of freedom the description in terms of pure states $|\psi(t)\rangle$ is no longer applicable. Instead, the state of the system is being represented by its density operator,

$$\rho = \sum_i p_i|\psi_i\rangle\langle\psi_i|, \tag{2.18}$$

where p_i is the probability to find the system in the pure state $|\psi_i\rangle$. ρ is a semi-positive operator with unit trace. The dynamical behavior of the system without external couplings is then given by the Liouville-von Neumann equation,

$$\frac{\mathrm{d}}{\mathrm{d}t}\rho = -\frac{\mathrm{i}}{\hbar}[\hat{H},\rho]. \tag{2.19}$$

Sometimes, one is not interested in the properties of the state corresponding to the full Hilbert space of the system, but merely some part of it. The properties of a single subsystem of a composite Hilbert space consisting of two subsystems $\mathcal{H}_1$ and $\mathcal{H}_2$ are given by the reduced density operator

$$\rho_1 = \mathrm{Tr}_2\{\rho\} = \sum_{i,i'}\sum_j \langle ij|\rho|i'j\rangle|i\rangle\langle i'|, \tag{2.20}$$

where ρ_1 is the reduced density operator of subsystem $\mathcal{H}_1$. The sum over i and i' runs over states in $\mathcal{H}_1$, while the sum over j is associated with $\mathcal{H}_2$.

2.3.2 Markovian master equations and the Lindblad formalism

In many cases the coupling to the external degrees of freedom constituting the environment E of the system under consideration S can be described following a few simple assumptions. For an intial state of the total system ρ the reduced density operator for the subsystem S is given by $\rho_S = \mathrm{Tr}_E\{\rho\}$. On the level of the total sytem $S + E$ the dynamics is still fully coherent as we take all interactions between system and environment into account. Consequently, the state of the total system at time t is given by

$$\rho(t) = U(t)\rho(0)U(t)^\dagger. \tag{2.21}$$

. After performing the trace over the environment, we may write this as

$$\rho_S(t) = \mathrm{Tr}_B\left\{U(t)\rho(0)U(t)^\dagger\right\} = \mathcal{V}(t)\rho_S(0). \tag{2.22}$$

Here, we have introduced the dynamical map $\mathcal{V}(t)$, which is a superoperator that transforms the state $\rho_S(0)$ into $\rho_S(t)$.

In many situations, correlations in the environment decay much faster than the characteristic time scale of the evolution of the system S. Consequently, memory effects can be neglected and the system is Markovian. The dynamical map $\mathcal{V}(t)$ then statisfies the semigroup property

$$\mathcal{V}(t_1 + t_2) = \mathcal{V}(t_1)\mathcal{V}(t_2) \quad t_1, t_2 \geq 0. \tag{2.23}$$

Note that contrary to the time evolution operator for coherent dynamics the semigroup properties imply that the dynamical map does not have an inverse. The generator of the semigroup is given by $\mathcal{V}(t) = \exp(\mathcal{L}t)$, and thus the dynamics of the system S follows the differential equation

$$\frac{\mathrm{d}}{\mathrm{d}t}\rho_S = \mathcal{L}\rho_S(t), \tag{2.24}$$

which is a Markovian master equation. The most general form of the Liouvillian $\mathcal{L}$ is the Lindblad form, which is given by

$$\mathcal{L}\rho_S = -\frac{\mathrm{i}}{\hbar}[H_S, \rho_S] + \sum_{k=1}^{N^2-1} \gamma_k \left(A_k \rho_S A_k^\dagger - \frac{1}{2}A_k^\dagger A_k \rho_S - \frac{1}{2}\rho_S A_k^\dagger A_k\right), \tag{2.25}$$

where $N = \dim \mathcal{H}_S$ is the size of the Hilbert space $\mathcal{H}_S$, on which the Hamiltonian H_S acts [Breuer2002]. The rates γ_k and the jump operators A_k can be deduced from a concrete microscopic model of the reservoir couplings.

2.3.3 Projection operator techniques for non-Markovian master equations

While Markovian master equations have a broad range of applications, in some situations the assumption of rapidly decaying correaltions in the environment is not valid. In particular, this is the case for isolated homegenous quantum many-body systems, where the equillibration of local observables can only occur due to interaction with its surroundings. The complete dynamics is governed by the Liouville-von Neumann equation of the full system according to

$$\frac{\mathrm{d}}{\mathrm{d}t}\rho = -\mathrm{i}[\hat{H},\hat{\rho}] = \mathcal{L}(t)\hat{\rho}. \tag{2.26}$$

Here, we aim at deriving a closed reduced dynamical equation for the subunit under consideration. This is done by introducing a projection superoperator $\mathcal{P}$ that projects onto the relevant part of the full density operator ρ [Breuer2002]. The dynamics of the reduced system is no longer unitary, but described by

$$\mathcal{P}\frac{\mathrm{d}}{\mathrm{d}t}\rho = \mathcal{P}\mathcal{L}(t)\rho. \tag{2.27}$$

While in many cases $\mathcal{P}$ defines a projection onto a tensor product state of one subsystem and a reference state ρ_E of the environment acoording to

$$\mathcal{P}\rho = \mathrm{Tr}_E\{\rho\} \otimes \rho_E, \tag{2.28}$$

this approach has recently been generalized to a broader class of projection superoperators [Breuer2007].

In order to obtain a closed equation for the relevent part, we define another projection superoperator $\mathcal{Q}$ projecting on the irrelevant part of the full density matrix ρ, i.e.,

$$\mathcal{Q}\rho = \rho - \mathcal{P}\rho, \tag{2.29}$$

leading to the dynamics described by

$$\mathcal{Q}\frac{\mathrm{d}}{\mathrm{d}t}\rho = \mathcal{Q}\mathcal{L}(t)\rho. \tag{2.30}$$

Being projection operators onto different parts of the system, $\mathcal{P}$ and $\mathcal{Q}$ have to satisfy the relations

$$\mathcal{P} + \mathcal{Q} = I \tag{2.31}$$

$$\mathcal{P}^2 = \mathcal{P} \tag{2.32}$$

$$\mathcal{Q}^2 = \mathcal{Q} \tag{2.33}$$

$$\mathcal{P}\mathcal{Q} = \mathcal{Q}\mathcal{P} = 0, \tag{2.34}$$

where I is the identity operation. Then, we can derive a set of differential equations describing the dynamics,

$$\mathcal{P}\frac{\mathrm{d}}{\mathrm{d}t}\rho = \mathcal{P}\mathcal{L}(t)\mathcal{P}\rho + \mathcal{P}\mathcal{L}(t)\mathcal{Q}\rho \tag{2.35}$$

$$\mathcal{Q}\frac{\mathrm{d}}{\mathrm{d}t}\rho = \mathcal{Q}\mathcal{L}(t)\mathcal{P}\rho + \mathcal{Q}\mathcal{L}(t)\mathcal{Q}\rho. \tag{2.36}$$

One possibility to tackle these equations is to formally solve (2.36) for $\mathcal{Q}\rho$, resulting in

$$\mathcal{Q}\rho(t) = \int_{t_0}^{t} \mathrm{d}s\, \mathcal{G}(t,s)\mathcal{Q}\mathcal{L}(s)\mathcal{P}\rho(s), \tag{2.37}$$

with an appropriate propagator $\mathcal{G}(t,s)$, while assuming factorizing initial conditions, i.e., $\mathcal{Q}\rho(t_0) = 0$. Inserting Eq. (2.37) into the differential equation for the relevant part (2.35) leads to a closed integro-differential equation known as the Nakajima-Zwanzig equation [Breuer2002]. Although it allows for a systematic perturbation expansion its structure is usually very complicated because every order requires the integration over superoperators involving the complete history of $\mathcal{P}\rho$. Therefore, its applicability to many-body problems is rather limited.

A different approach tries to explicitly avoid the integral over the complete history by looking at the inverse of the time evolution. We replace the $\rho(s)$ in Eq. (2.37) by

$$\rho(s) = G(t,s)(\mathcal{P}+\mathcal{Q})\rho(t), \tag{2.38}$$

where $G(t,s)$ is the backward propagator of the full system, i.e., the inverse of its unitary evolution. We then can write (2.37) as

$$\mathcal{Q}\rho(t) = \Sigma(t)(\mathcal{P}+\mathcal{Q})\rho(t), \tag{2.39}$$

where we have introduced the superoperator

$$\Sigma(t) = \int_{t_0}^{t} \mathrm{d}s\, \mathcal{G}(t,s)\mathcal{Q}\mathcal{L}(s)\mathcal{P}G(t,s). \tag{2.40}$$

We then move all occurrences of $\mathcal{Q}\rho(t)$ in (2.39) to the left-hand side. The superoperator $1-\Sigma(t)$ may be inverted for small times or weak interactions with the irrelevant part[Breuer2002], leading to

$$\mathcal{Q}\rho(t) = [1-\Sigma(t)]^{-1}\mathcal{P}\rho(t). \tag{2.41}$$

Inserting this result into Eq. (2.35) yields a differential equation for the relevant part of the system,

$$\mathcal{P}\frac{\mathrm{d}}{\mathrm{d}t}\rho(t) = \mathcal{P}\mathcal{L}(t)[1-\Sigma(t)]^{-1}\mathcal{P}\rho(t). \tag{2.42}$$

Since this differential equation for the relevant part does not involve a convolution integral as in the Nakajima-Zwanzig equation, it is called the time-convolutionless (TCL) master equation [Breuer2002].

The TCL generatior is defined as

$$\mathcal{K}(t) = \mathcal{P}\mathcal{L}(t)[1-\Sigma(t)]^{-1}\mathcal{P}. \tag{2.43}$$

In order to perform a perturbation expansion of $\mathcal{K}(t)$ we rewrite $[1-\Sigma(t)]^{-1}$ as a geometric series, allowing to write the TCL generator as

$$\mathcal{K}(t) = \sum_n \mathcal{P}\mathcal{L}(t)\Sigma(t)^n\mathcal{P} \equiv \sum_n \lambda^n \mathcal{K}_n(t), \tag{2.44}$$

where λ is the coupling constant in which the series expansion is performed. One may then use (2.40) and the series expansion of $\mathcal{G}(t,s)$ and $G(t,s)$ to compute the $\mathcal{K}_n$. In many situations, the odd terms of the series expansion vanish [Breuer2002], and the leading term given by the second order expansion is

$$\mathcal{K}_2 = \int_0^t \mathrm{d}t_1 \mathcal{P}\mathcal{L}(t)\mathcal{L}(t_1)\mathcal{P}, \tag{2.45}$$

leading to the second-order TCL master equation

$$\mathcal{P}\frac{\mathrm{d}}{\mathrm{d}t}\rho = \int_0^t \mathrm{d}t_1 \mathcal{P}\mathcal{L}(t)\mathcal{L}(t_1)\mathcal{P}\rho. \tag{2.46}$$

Part II

Quantum phases of driven strongly interacting Rydberg atoms

> Essentially, all models are wrong, but some are useful.
>
> George E. P. Box

3 Mean-field theory for driven Rydberg atoms

In the past many experiments have been performed to investigate the dipole blockade [Tong2004, Singer2004, Vogt2006, Heidemann2007]. The theoretical treatment of these systems has so far been largely limited to numerical simulations of small systems [Robicheaux2005b], modelling in terms of phenomenological scaling relations [Heidemann2007], and quantum master equation approaches in the limit of strong dissipation [Ates2007]. In contrast to the previous analyses studying the time evolution, the approach for the study of strongly interacting Rydberg gases presented in this chapter is based on the observation that the driven system relaxes into an equilibrium state. This equilibrium state is dominated by the thermodynamic phases of the Hamiltonian describing the driven system, which exhibits a continuous quantum phase transition in the detuning Δ. The experimentally relevant resonant regime with $\Delta = 0$ is determined by the critical properties of the phase transition.

3.1 Hamiltonian of the system

Typical timescales for an experiment are on the order of a few microseconds [Heidemann2007]; the much slower thermal motion can be neglected. Therefore the positions $\mathbf{r}_i$ of the atoms are "frozen" [Anderson1998] with the positions $\mathbf{r}_i$ being randomly distributed according to the distribution function of a thermal gas. Furthermore, radiative decay of the Rydberg state occuring on a timescale of 100 s [Gallagher1994] and thus can also be ignored. Other processes that might harm the coherent evolution of the system are collective ionizations of the Rydberg atoms [Robicheaux2005a]; however for S states interacting via a repulsive interaction described by a generalized coefficient C_p ionization processes are slowed down significantly [Amthor2007]. Consequently, the dynamics on the timescale of the experiment is well described by the Hamiltonian in the rotating frame of the laser excitation with the Rabi

frequency Ω and the detuning Δ,

$$H = -\frac{\Delta}{2}\sum_i \sigma_z^{(i)} + \frac{\hbar\Omega}{2}\sum_i \sigma_x^{(i)} + C_p \sum_{j<i} \frac{P_{ee}^{(i)} P_{ee}^{(j)}}{|\mathbf{r}_i - \mathbf{r}_j|^p}, \tag{3.1}$$

where the counter-rotating terms have been dropped.

3.2 Phase transition in the classical limit

It is instructive to first look at the Hamiltonian in the classical limit, i.e., $\Omega = 0$. While in this limit the Hamiltonian has no direct physical realization as the rotating frame is not properly defined, the ground state for finite Ω is dominated by the ground state properties at $\Omega = 0$.

For negative detuning Δ the ground state is a paramagnet with all spins pointing down since adding a Rydberg excitation will cost energy. However, for positive Δ the many-body ground state will have some Rydberg excitations present. For a fixed number of Rydberg excitations in the system, the energy will be minimal when the interaction energy is minimized, which is the case in a crystalline arrangement. Tab. 3.1 shows the interaction energy for different lattice configurations. Consequently, the ground state will have a hexogonal close-packed lattice structure. At $\delta = 0$ there is a continuous phase transition from the paramagnetic to the crystalline phase.

Lattice	$E/V[C_6/a_R^9]$
Simple cubic	0.479
Body-centered cubic	0.488
Face-centered cubic	0.446
Hexagonal close-packed	0.412

Table 3.1: Interaction energies per volume for three different crystal lattice configurations with lattice spacing a_R.

The lattice spacing of the Rydberg excitations a_R can be calculated in the continuum limit. For simplicity, we assume an underlying 1D lattice with spacing a and later generalize the result to higher dimensions. The interaction energy takes the form

$$E_{\text{int}} = \frac{Na}{a_R}\sum_i \frac{C_6}{a_R^p i^p} = \frac{C_6 N a \zeta(p)}{a_R^{p+1}}. \tag{3.2}$$

The Zeeman energy of the σ_z term is

$$E_Z = -\frac{Na}{a_R}\Delta. \tag{3.3}$$

Summing both energies and minimzing with respect to a_R leads to

$$a_R = \sqrt[p]{\frac{(p+1)C_p\zeta(p)}{\Delta}}, \tag{3.4}$$

i.e., the Rydberg fraction scales as $f_R \sim \Delta^{1/6}$. In d dimensions the total energy takes the form

$$E = -\frac{Na^d}{a_R^d}\Delta + \frac{zNa^dC_p}{a_R^{d+p}}, \tag{3.5}$$

where $z_d = \sum_j 1/(r_j/a_R)^p$ is the effective coordination number in d dimensions, which also includes effects beyond nearest neighbor interactions. This results in

$$a_R = \sqrt[p]{\frac{(d+p)z_dC_p}{d\Delta}} \tag{3.6}$$

and $f_R \sim \Delta^{d/p}$, respectively.

3.3 Mean-field theory for strong blockade

3.3.1 Blockade mechanism

In the case of finite Ω, some important features of the Hamiltonian (3.1) can already be learned from a two-atom calculation. A small spatial separation between the atoms results in a blockade of the doubly excited state due to the strong interaction between the Rydberg states, see Fig. 3.1. This phenomenon is known as the "dipole blockade" and has been proposed as a key ingredient for quantum computing with Rydberg atoms [Jaksch2000, Lukin2001].

For a system of two atoms, the state space can be separated into a symmetric subspace containing the states $\{|gg\rangle, (|ge\rangle + |eg\rangle)/\sqrt{2}, |ee\rangle\}$ and the antisymmetric subspace consisting of the state $(|ge\rangle - |eg\rangle)/\sqrt{2}$ only. As the Hamiltonian is invariant under particle exchange, the two subspaces are not coupled, with the antisymmetric state having zero energy.

At short distances the interaction energy is large and thus the number of Rydberg excitations is a good quantum number. For weak interactions at large

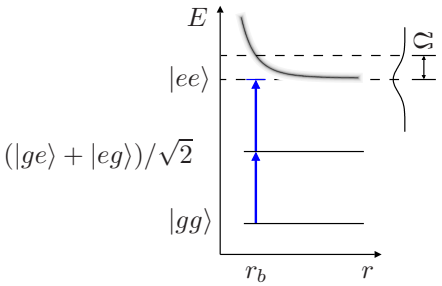

Figure 3.1: For two spatially close atoms only one can be excited as the strong interaction shifts the doubly excited state out of resonance.

distances the eigenstates correspond to the dressed atom states according to the Rabi frequency Ω and the detuning Δ. The crossover between these two regimes occurs at the two-atom blockade radius

$$r_b = \sqrt[p]{\frac{C_p}{\hbar\sqrt{\Omega^2+\Delta^2}}}. \tag{3.7}$$

If the typical inter-particle distance a is much larger then r_b, then the eigenstates of the many-body Hamiltonian (3.1) are essentially uncorrelated with the Rydberg interaction being a small perturbation. In the limit of large detuning the Rydberg state can be adiabatically eliminated, leaving the possibility to convey interactions between ground state atoms by weak Rydberg dressing [Honer2010]. Conversely, in the regime $a \ll r_b$ strong many-body effects will arise that require new concepts and tools to deal with. As we have seen in Sect. 3.2 the strongly interacting system is close to a continuous phase transition; in this critical regime there is no well-defined energy gap and thus perturbation theory is not applicable.

In the strongly interacting limit it is convenient to use the interaction energy $E_0 = C_p n^{p/d}$ as the global energy scale and express the Rabi frequency and the detuning as dimensionless quantities, i.e.,

$$\alpha = \frac{\hbar\Omega}{C_p n^{p/d}} \quad \text{and} \quad \gamma = \frac{\Delta}{C_p n^{p/d}}. \tag{3.8}$$

3.3.2 Ground state properties

The most straightforward choice to deal with a system close to a continuous phase transition is mean-field theory. The order parameter of the phase

transition is the fraction of Rydberg excited atoms f_R. However, we cannot simply apply conventional Landau theory, i.e, performing a taylor expansion of the energy in f_R, as there are no correlations in Landau theory, which is incompatible with the dipole blockade. Instead, we make an explicit ansatz for the pair-correlation function

$$g_2(\mathbf{r}_i - \mathbf{r}_j) = \frac{\langle P_{ee}^{(i)} P_{ee}^{(j)} \rangle}{f_R^2}, \tag{3.9}$$

where $g_2(\mathbf{r})$ vanishes in the blockaded region for $|\mathbf{r}| \ll a_R$, while at large distances $|\mathbf{r}| \gg a_R$ the correlation disappears and $g_2(\mathbf{r}) = 1$. The transition from a strong suppression to the uncorrelated regime is very sharp due to the van der Waals repulsion [Robicheaux2005b], and the pair correlation function is well described by a step function $g_2(\mathbf{r}) = \Theta(|\mathbf{r}| - a_R)$. Then, the mean field theory is obtained by replacing the microscopic interaction by the mean interaction of the surrounding atoms

$$P_{ee}^{(i)} P_{ee}^{(j)} \approx \left[P_{ee}^{(i)} f_R + P_{ee}^{(j)} f_R - f_R^2 \right] g_2(\mathbf{r}_i - \mathbf{r}_j), \tag{3.10}$$

which neglects the quadratic fluctuations around the mean field and reduces the Hamiltonian to a sum of single site Hamiltonians. In the strongly interacting regime with $a \ll r_b$, the number of atoms in the blockaded regime is large, i.e., $a_R^d n \gg 1$, which allows us to replace the summation over the surrounding atoms j by an integral over space with a homogeneous atomic density n, i.e,

$$\sum_j \frac{C_p}{|\mathbf{r}_i - \mathbf{r}_j|^p} = A_d n \int_0^\infty \mathrm{d}^d r \, r^{d-1} g_2(r) \frac{C_p}{r^p} = \frac{A_d}{p-d} n C_p a_R^{p-d}, \tag{3.11}$$

where A_d is the surface area of the d-dimensional unit sphere. Then, we obtain the Hamiltonian for the i^{th} atom,

$$\begin{aligned} \frac{H_{\text{MF}}^{(i)}}{E_0} &= \frac{\gamma}{2}\sigma_z^{(i)} + \frac{\alpha}{2}\sigma_x^{(i)} + \frac{A_d}{p-d} \frac{f_R}{n^{p/d-1} a_R^{p-d}} P_{ee}^{(i)} - \frac{A_d}{2(p-d)} \frac{f_R^2}{n^{p/d-1} a_R^{p-d}} \\ &= \mathbf{h} \cdot \boldsymbol{\sigma}^{(i)} + h_0. \end{aligned} \tag{3.12}$$

In the limit of strong blockade the correlation length ξ is equal to a_R as this will minimize the interaction energy for a given Rydberg fraction. The correlation function $g_2(\mathbf{r})$ thus satisfies the normalization condition

$$n f_R \int d\mathbf{r} \, [1 - g_2(\mathbf{r})] = 1, \tag{3.13}$$

which provides the relation

$$a_R = (V_d f_R n)^{-1/d}, \tag{3.14}$$

with V_d being the volume of the d-dimensional unit sphere. The effective Hamiltonian is equivalent to a spin in a magnetic field $\mathbf{h}$, which posseses both a transverse component $h_x \sim \alpha$ and a longitudinal component $h_z \sim f_R^{p/d}$, and a constant energy offset $h_0 = h_z(1 - f_R)$. Using a spin rotation, we can diagonalize the Hamiltonian $H_{\mathrm{MF}}^{(i)} = h\sigma_{z'}^{(i)} + h_0$ with $h = \sqrt{h_x^2 + h_z^2}$. Here, $\sigma_{z'}^{(i)} = \cos\theta\sigma_z^{(i)} + \sin\theta\sigma_x^{(i)}$ denotes the Pauli matrix in the new basis with the rotation angle $\tan\theta = h_x/h_z$. The ground state of the system is then given by $\langle\sigma_{z'}\rangle = -1$, leading to the self-consistant equation

$$\alpha = \frac{1}{p-d}|4A_d V_d^{p/d-1} f^{p/d+1/2} - p\Delta f^{1/2}|. \tag{3.15}$$

This equation can be cast into the form

$$\alpha \sim f_R^{\delta}|B - \Delta/f_R^{1/\beta}|, \tag{3.16}$$

from which the critical exponents $\delta = p/d + 1/2$ and $\beta = d/p$ can be determined. Solving the mean-field equation for f_R leads to the equation of state shown in Fig. 3.2, with the limiting cases $f_R \sim \gamma^{d/p}$ for $\alpha = 0$ as in the exact result and

$$f_R \sim \alpha^{2d/(2p+d)} \tag{3.17}$$

for $\gamma = 0$.

3.3.3 Sudden increase of the Rabi frequency

So far, the mean-field analysis was centered onto the ground state properties of the system. However, in typical experiments the Rabi frequency is not varied adiabatically such that the system follows its many-body ground state; instead, the driving lasers are switched to full power instantaneously, leading to a complex excitation dynamics. Nevertheless, it is possible to capture most aspects of the dynamical behavior by mean-field theory. Here, the idea is that in a strongly interacting system the energy deposited into the system by the sudden increase of the Rabi frequency is small compared to the global energy scale E_0. Consequently, the system remains close to its ground state and the dynamically properties are governed by its critical behavior.

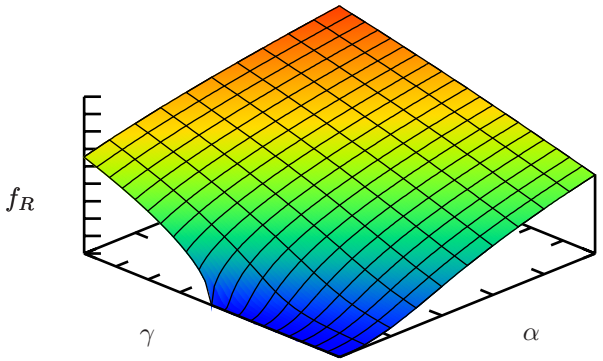

Figure 3.2: Excited state fraction f_R of a strongly interacting Rydberg gas according to mean-field theory ($d = 3$, $p = 6$). The nonanalytic behavior of the order parameter at the critical point with $\alpha = \gamma = 0$ is apparent.

Stationary state In the following we will concentrate on a resonant driving with $\gamma = 0$ and a van der Waals interaction (p=6) in three spatial dimensions as this is the experimentally most relevant case. Then, the dynamics follows a relaxation to a stationary equilibrium state [Heidemann2007, Robicheaux2005b], which we want to describe quantitatively. The derivation of the mean-field Hamiltonian works in the same way as for the ground state. However, after applying the spin rotation the state of the system is no longer characterized by the relation $\langle \sigma_{z'} \rangle = -1$. Instead the density matrix of the equilibrium state is determined by energy conservation: the energy of the equilibrated state is equal to the energy of the initial state, which is the state of all spins pointing down. Therefore, we have

$$\sum_i \mathrm{Tr}\left\{ H_{\mathrm{MF}}^{(i)} \rho^{(i)}(t=\infty) \right\} = \langle \psi(t=0)|H|\psi(t=0)\rangle = 0. \tag{3.18}$$

Furthermore, the density matrix will be diagonal in the eigenbasis of the mean-field Hamiltonian; this corresponds to a microcanonical equilibrium state. The mean-field solution for this state reduces to $\rho^{(i)} = \left[1 - (h_0/h)\sigma_{z'}^{(i)}\right]/2$, and a transformation into the original coordinates yields the self-consistency relation

$$f_R = \langle \hat{P}_{ee}^{(i)} \rangle = \frac{1}{2} \frac{(4\pi)^4 f_R^5 + (9\alpha)^2}{(4\pi f_R)^4 + (9\alpha)^2}. \tag{3.19}$$

The solution in the limit $\alpha \ll 1$ provides the same critical exponent $1/\delta = 2/5$ as for the ground state with the prefactor $c = (9/16\pi^2)^{2/5}$.

Relaxation dynamics Finally, we are interested in a description of the time evolution and derive a master equation with the mean-field solution as its stationary state. First note that the self-consistent time evolution of $\rho^{(i)}$ with the mean field Hamiltonian $H_{\mathrm{MF}}^{(i)}$ exhibits undamped coherent oscillations. The natural mechanisms for for the decoherence of these oscillations and the equilibration into a stationary state are the residual interactions between the atoms, which go beyond the mean-field description. We write the exact Hamiltonian (3.1) as a sum of the mean-field terms and the remaining fluctuations

$$H = \sum_i H_{\mathrm{MF}}^{(i)} + \Delta H. \tag{3.20}$$

The derivation of the master equation from the microscopic Hamiltonian uses the time-convolutionless projection operator method with an extended projection operator [Breuer2007]: we select a single site i, which will play the role of the system with the Hamiltonian $H_{\mathrm{MF}}^{(i)}$, while the surrounding atoms act as the bath coupled to the system state by the Hamiltonian ΔH. The role of the pair-correlation function is to enforce the blockade regime. Here, we are not interested in determining the pair-correlation function self-consistently, but rather assume the pair-correlation function to be fixed during the time evolution. Then, its influence is well accounted for by expressing the remaining interactions as

$$\Delta H = \sum_{i<j} g_2(\mathbf{r}_i - \mathbf{r}_j)\, \frac{C_6}{|\mathbf{r}_i - \mathbf{r}_j|^6} \left(P_{ee}^{(i)} - f_R\right)\left(P_{ee}^{(j)} - f_R\right). \tag{3.21}$$

The projection operator consistent with our mean-field theory, i.e., $\mathcal{P}\Delta H\rho = 0$ reduces to $\mathcal{P}\rho = \bigotimes_i \rho^{(i)}$. Here, $\rho^{(i)}$ denotes the reduced density matrix defined by the partial trace $\rho^{(i)} = \mathrm{Tr}_i\{\rho\}$, which performs the trace over all atomic states except of the i^{th} atom. Next, it is useful to express the operator

$$\hat{P}_{ee}^{(i)} = \hat{A}_{-\omega_0}^{(i)} + \hat{A}_0^{(i)} + \hat{A}_{\omega_0}^{(i)} \tag{3.22}$$

in terms of the projections onto the eigenstates of $H_{\mathrm{MF}}^{(i)}$, where $\hbar\omega_0 = 2h$ denotes the energy splitting of the mean-field Hamiltonian. Introducing the interaction picture with respect to $\sum_i H_{\mathrm{MF}}^{(i)}$ the interaction Hamiltonian $H_{\mathrm{int}}^{(i,j)}(t)$ within the rotating wave approximation reduces to

$$H_{\mathrm{int}}^{(i,j)}(t) = \sum_{\omega=0,\pm\omega_0} \frac{C_6}{|\mathbf{r}_i - \mathbf{r}_j|^6} \hat{A}_\omega^{(i)} \otimes \hat{A}_\omega^{(j)\dagger}. \tag{3.23}$$

Using the eigenstates of the mean-field Hamiltonian (i.e., $\sigma_{z'} = |\nearrow\rangle\langle\nearrow| - |\swarrow\rangle\langle\swarrow|$) the terms $\hat{A}_{\pm\omega_0}$ given by

$$\hat{A}_{+\omega_0} = \hat{A}_{-\omega_0}^{\dagger} = |\swarrow\rangle\langle\swarrow|\uparrow\rangle\langle\uparrow|\nearrow\rangle\langle\nearrow| \tag{3.24}$$

describe the exchanges of an excitation between the system $\rho^{(i)}$ and the surrounding bath and is relevant for the equilibration of the time evolution, while the terms with $\hat{A}_0$ given by

$$\hat{A}_0 = |\swarrow\rangle\langle\swarrow| \uparrow\rangle\langle\uparrow |\swarrow\rangle\langle\swarrow| + |\nearrow\rangle\langle\nearrow| \uparrow\rangle\langle\uparrow |\nearrow\rangle\langle\nearrow| \tag{3.25}$$

account for a dephasing. The second order time-convolutionless master equation [Breuer2002, Breuer2007] for the reduces density matrix $\rho^{(i)}(t)$ takes the form

$$\frac{\mathrm{d}}{\mathrm{d}t}\rho^{(i)} = \sum_{\omega,\omega'} \gamma_{\omega\omega'} \left(\hat{A}^{(i)}_{\omega} \rho^{(i)} \hat{A}^{(i)\dagger}_{\omega'} - \frac{1}{2} \left\{ \hat{A}^{(i)\dagger}_{\omega'} \hat{A}^{(i)}_{\omega}, \rho^{(i)} \right\} \right), \tag{3.26}$$

with the rates

$$\gamma_{\omega\omega'} = \frac{512\pi^4 nt}{27\hbar^2} \frac{1}{a_R^9} \langle \hat{A}^{(i)}_{\omega'} \hat{A}^{(i)\dagger}_{\omega} \rangle. \tag{3.27}$$

Here, we have again used the translation invariance of the system in the critical region $\alpha \ll 1$ allowing us to replace the average over the j^{th} atom, with the local density matrix $\rho^{(i)}(t)$. Note that although the projection $\mathcal{P}$ does not commute with the time derivative the master equation is still valid up to second order as deviations only appear in higher orders. Furthermore, the linear time-dependence of the rates indicates that the master equation is only valid in the quadratic regime; afterwards the rates will saturate to the value given by Fermi's golden rule [Weimer2008b]. Here, the crossover to the linear regime governed by Fermi's golden rule occurs at a time

$$t_c = \frac{\pi}{\omega_0}, \tag{3.28}$$

which corresponds to a timescale where the system is already close to its equilibrium state, see Fig. 3.3. The obtained master equation is a highly nonlinear equation for the local density $\rho^{(i)}(t)$, where at each time step the mean-field $f_R = \mathrm{Tr}\{\rho^{(i)} \hat{P}^{(i)}_{ee}\}$ and the rates $\gamma_{\omega,\omega'}$ have to be determined. We would like to stress that the master equation conserves energy with the above mean-field solution as a stationary state. The master equation can be efficiently solved numerically after a transformation back into the Schrödinger picture, see Fig. 3.3.

3.3.4 Derivation of the superatom model

The superatom model is a phenomenological approach to describe the properties of strongly interacting Rydberg gases. The idea behind it is that in

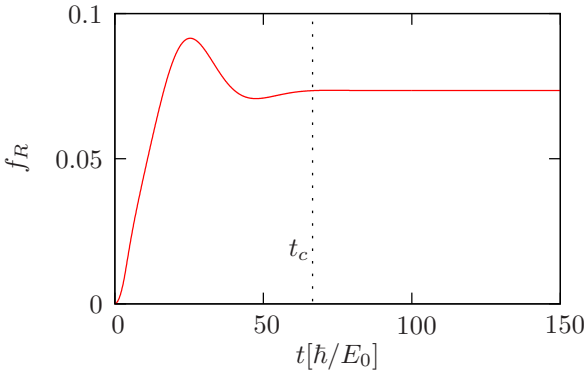

Figure 3.3: Solution of the quantum master equation ($\alpha = 1/36$). The crossover time t_c according to (3.28) is shown as a dotted line, i.e., the relaxation takes place in the quadratic regime.

a blockaded region containing N atoms only a single atom can be excited [Heidemann2007]. This excitation has a collective nature that is shared among all atoms in the blockade region and is described by the symmetric state

$$|S_1\rangle = \frac{1}{\sqrt{N}} \sum_i |g_1 \dots e_i \dots g_N\rangle. \tag{3.29}$$

Rabi oscillations between this state and the ground state $|S_0\rangle = |g_1 \dots g_N\rangle$ are governed by the collective Rabi frequency $\sqrt{N}\Omega$. In the superatom picture this energy scale is then set equal to the interaction energy, i.e,

$$\sqrt{N}\Omega = \frac{C_6}{a_R^6}, \tag{3.30}$$

and the value of $N = \int d^3 r n(\mathbf{r})$ is determined in a self-consistent way similar to mean-field theory [Heidemann2008b].

As the superatom model predicts the same exponent $1/\delta$ as mean-field theory, it should be possible to derive the superatom model on the basis of the mean-field Hamiltonian (3.12) with $\Delta = 0$. The characteristic frequency then reduces to

$$h = \sqrt{h_x^2 + h_z^2} \sim \sqrt{c\alpha^2 + f_R^4}. \tag{3.31}$$

In the scaling limit $\alpha \to 0$ only the second term is relevant and we thus find after using the scaling relation (3.17)

$$h \sim f_R^2 \sim f_R^{-1/2}\Omega = \sqrt{N}\Omega \tag{3.32}$$

as in the superatom model. This relation also allows us to determine the dynamical critical exponent z defined as $h \sim a_R^{-z}$. Here, we find for a generalized interaction described by the coefficient C_p for the dynanucak critical exponent $z = p$.

3.4 Universal scaling theory

An entirely different way to derive the critical exponents that does not rely on a self-consistent approach is to use a universal scaling function. We know already that close to the critical point the system becomes scale invariant and the scaling of all observables only depends on the two dimensionless quantities α and γ. We therefore express the Rydberg fraction as

$$f_R = \alpha^\nu \chi\left(\frac{\Delta}{\alpha^\kappa}\right), \tag{3.33}$$

where we have introduced the universal scaling function $\chi(y)$. We have seen that in the limit of $\alpha = 0$ this expression has to reduce to $f_R \sim \gamma^{d/p}$. The only possibility for this to happen is when $\chi(y) \sim y^{d/p}$ and the α dependence cancels out, i.e.,

$$\nu = -\kappa\frac{d}{p}. \tag{3.34}$$

The second known limit can be derived deep in the paramagnetic phase. For $\gamma \gg \alpha$ perturbation theory is applicable, resulting in $f_R \sim \alpha^2/\gamma^2$. Again, this is only possible for $\chi \sim 1/y^2$ and

$$\nu + 2\kappa = 2. \tag{3.35}$$

Solving these two equations for ν and κ leads to

$$f_R = \alpha^{2d/(2p+d)} \chi\left(\frac{\gamma}{\alpha^{2p/(2p+d)}}\right), \tag{3.36}$$

which is nothing but the inverse of the mean-field equation (3.16). Equivalently, one can say that the only value for the critical exponent that is consistent with these limits is correctly given by mean-field theory. This produces strong evidence that the system belongs to a universal class where the upper and lower critical dimension are identical, i.e., if there is a phase transition the critical exponents are correctly given by mean-field theory.

Furthermore, this scaling ansatz also makes a prediction for occurence of the melting transition of the crystalline phase. The transition line can only depend

on the argument of $\chi(y)$, i.e., the critical detuning for the phase transition is given by

$$\gamma_c \sim \alpha^{2p/(2p+d)}. \tag{3.37}$$

The resulting phase diagram according to universal scaling theory is shown in Fig. 3.4.

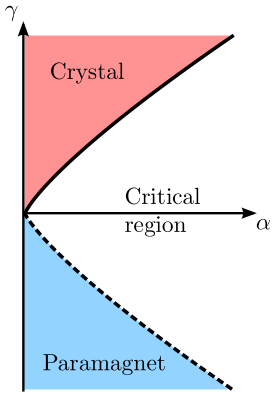

Figure 3.4: Phase diagram according to universal scaling theory ($p = 6$, $d = 3$) with a crystal and a paramagnetic phase. For negative detuning there is a crossover from the paramagnet to the critical region, while for positive detuning there is a true phase transition.

3.5 Validity of mean-field theory

While we have seen that we can successfully derive mean-field results for strongly interacting Rydberg atoms, but we have yet to determine the validity of the results. The accordance of mean-field theory with the the universal scaling ansatz discussed in the previous section already presents strong evidence that mean-field theory produces reliable results, however a deeper understanding and a quantitative assessment are still lacking. Especially in low dimensional systems, mean-field predictions can be questionable, however, at the same time systems with long-range interactions typically tend to have more mean-field-like character. In the following we give analytical, numerical, and experimental evidence on which of these two competing factors will finally determine the critical properties of strongly interacting Rydberg atoms.

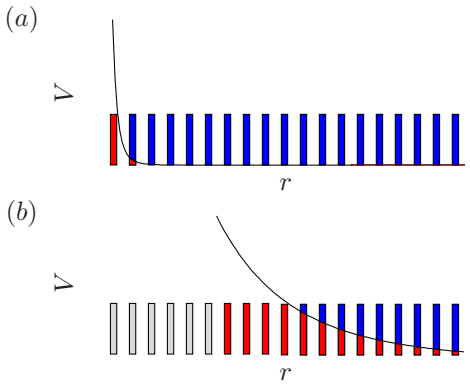

Figure 3.5: Interaction strength V in terms of the global energy scale E_0 over distance r. (a) A symmetric interaction decays rapidly, leading to an effective description in terms of a nearest-neighbor coupling. (b) An asymmetric interaction potential leads to a large blockaded region (grey particles), but the effective number of interaction partners diverges in the scaling limit.

The standard approach to determine the limits where mean-field predictions are justified is the Ginzburg criterion. It essentially states that for mean-field theory to be applicable, fluctuations around the mean field must happen on a small scale compared to the correlation length ξ [Goldenfeld1992]. However, here the fluctuations

$$\Delta P = |P_{ee}^{(i)} P_{ee}^{(j)} = \left[P_{ee}^{(i)} f_R + P_{ee}^{(j)} f_R - f_R^2 \right] g_2(\mathbf{r}_i - \mathbf{r}_j)| \tag{3.38}$$

cannot be determined self-consistently as we made an explicit ansatz for the pair-correlation function $g_2(\mathbf{r})$. Therefore, we have to resort to other approaches to determine the validity of mean-field theory.

3.5.1 Heuristic arguments

Generally speaking, mean-field theory becomes exact when the number of interaction partners z diverges. There are two different ways this can happen, either by increasing the dimensionality of the system, or by increasing the range of the interaction potentials. For a symmetric interaction $\sigma_z \sigma_z$ a van der Waals interaction can be effectively reduced to a nearest-neighbor coupling. However, Rydberg atoms interact via an asymmetric $P_{ee} P_{ee}$ interaction. In the scaling limit with $\alpha \ll 1$ this leads to a divergence of z, see Fig. 3.5.

3.5.2 Numerical simulations

To get a more quantitative assesment of the validity of mean-field results it is instructive to obtain exact numerical results on the basis of the full spin Hamiltonian (3.1). For a system with N atoms the dimension of the full Hilbert space grows exponentially like 2^N; therefore, the exact behavior can only be calculated for a relatively small number of atoms [Robicheaux2005b]. However, the strong van der Waals repulsion suppresses the occupation probabilities of many basis states, which allows us to significantly reduce the Hilbert space: for each basis state we compute the van der Waals energy and remove the state if its van der Waals energy is larger than a cutoff energy E_C. This reduction leads for $N = 100$ to approximately 10^6 relevant basis states compared to the 10^{30} basis states of the full Hilbert space. Convergence of this method can be been checked by increasing E_C.

Within mean-field theory we have already seen that the critical properties are identical whether we study ground state properties or the relaxation to a stationary state after a sudden increase of the Rabi frequency. As we are also interested in dynamical properties we perform a numerical integration of the time-dependent Schrödinger equation with the initial state being the product state of all spins pointing down. We place the atoms randomly according to a uniform distribution into a box of unit volume having periodic boundary conditions. Then, the resulting dynamics obtained using a fourth-order Runge-Kutta method is shown in Fig. 3.6. One can see the expected relatation towards a stationary state, although for $N = 50$ atoms there are considerable finite-size effects present in the system, especially concerning the saturation value of the Rydberg fraction f_R. However, these can be reduced by averaging over many different initial positions of the atoms according to the same distribution function. Using our numerical simulation we can also test the validity of our modelling of the pair correlation function as a step function. As can be seen from Fig. 3.7 the assumption is qualitatively correct although deviations can be clearly seen. First, there is a pronounced peak near the correlation length ξ and also the normalization constraint of (3.13) leading to $\xi = a_R$ is also slightly violated.

We can now investigate how the scaling of the saturated Rydberg fraction f_{sat} changes when the dimensionless parameter α is varied. For this, the value of f_{sat} was averaged over 50 different initial conditions. Fig. 3.8 shows the scaling of f_R in a three- and one-dimensional system, respectively. As α has been varied both by changing the density n and the Rabi frequency Ω, we see in both cases a clear data collapse to a single line. Moreover, the numerically obtained critical exponents are in excellent agreement with mean-field results (0.404 versus 0.400 and 0.150 versus 0.154).

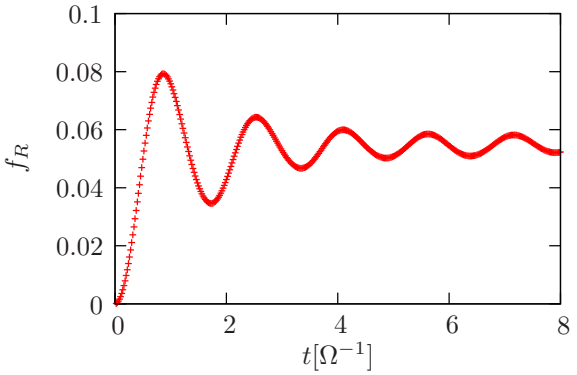

Figure 3.6: Relaxation dynamics of the Rydberg fraction f_R ($p = 6$, $d = 3$, $N = 50$, $\alpha = 1/25$, $\Delta = 0$).

After having confirmed that mean-field theory gives the correct critical exponents, we proceed on investigating the relaxation dynamics of the system. However, while the scaling of the stationary state is well predicted by mean-field theory, the prefactor is not due to our rather crude choice of the pair correlations in terms of a step function. The relevant quantity is the integral over the interaction energy weighted by the pair correlation, i.e.,

$$n \int \mathrm{d}^3 r \frac{C_6}{r^6} g_2(r) \equiv \gamma \frac{16}{9} \pi^2 f_R C_6 n^2, \tag{3.39}$$

where we have introduced the parameter γ that accounts for the deviation from the step function. There are now two possibilities to obtain γ from the numerical data. First, we can directly evaluate the integral with the numerical values of $g_2(r)$ (cf. Fig. 3.7), yielding $\gamma = 2.5$. Alternatively, we can compute its value by fitting the mean-field result for the stationary Rydberg fraction by explicitely including γ in the mean-field equation, which results in $\gamma = 3.1$. When studying relaxation dynamics the distance to equilibrium is usually more relevant than the precise form of correlations in the system; therefore, in the following we choose γ to reproduce the correct saturated Rydberg fraction. We can now compare the numerically obtained time evolution with the solution to our quantum master equation (3.26). However, we have also account for that fitting the value of f_{sat} will lead to a different intrinsic time scale. In Sect. 3.3.4 we have seen that the effective Rabi frequency scales like $f_{sat}^{-1/2}\Omega$. Rescaling the time scale accordingly, the comparison between both methods is shown in Fig. 3.9. As can be seen there is excellent agreement between the exact numerical results and the solution of the quantum master equation. The

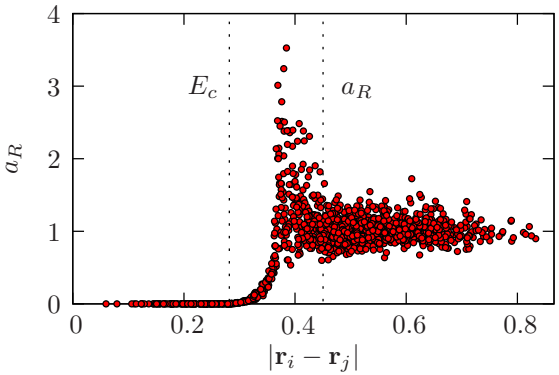

Figure 3.7: Pair correlation function $g_2(r)$ in the stationary state ($p = 6$, $d = 3$, $N = 50$, $\alpha = 1/25$, $\Delta = 0$). The lengthscale corresponding to the cutoff energy E_c and the mean Rydberg spacing a_R are shown as vertical lines.

remaining oscillations at large times still present after averaging are further suppressed for larger system sizes, and therefore represent a finite size effect.

3.5.3 Experimental results

Experimentally, Rydberg excitations are created by two-photon processes via an intermediate atomic level that can be adiabatically eliminated. The densities required for reaching the strongly interacting limit can be realized in a magnetic trap [Heidemann2007, Raitzsch2008, Heidemann2008b] or in an optical diplole trap [Raitzsch2009]. By varying the Rabi frequency Ω or the density n one has the possiblity to vary the dimensionless parameter α in two independent ways. However, when comparing theoretical predictions to experimental results one has to account for the inhomogeneity of the density due to the trapping potential. In a harmonic trap the three dimensional density distribution of the N ground state atoms has a Gaussian shape with radii given by the standard deviations $\sigma_{x,y,z} = \sqrt{k_B T/2m\omega_{x,y,z}}$, which are determined by the trapping frequencies $\omega_{x,y,z}$, the mass m of the atoms, and the temperature T of the cloud,

$$n(\mathbf{r}) = \frac{N}{(2\pi)^{3/2}\sigma_x\sigma_y\sigma_z} \exp\left(-\frac{x^2}{2\sigma_x^2} - \frac{y^2}{2\sigma_y^2} - \frac{z^2}{2\sigma_z^2}\right). \tag{3.40}$$

Note, that the temperature T associated with the kinetic energy of the atoms is decoupled from the dynamics of the Rydberg excitations in the frozen Rydberg gas. Within the local density approximation, we can describe the properties

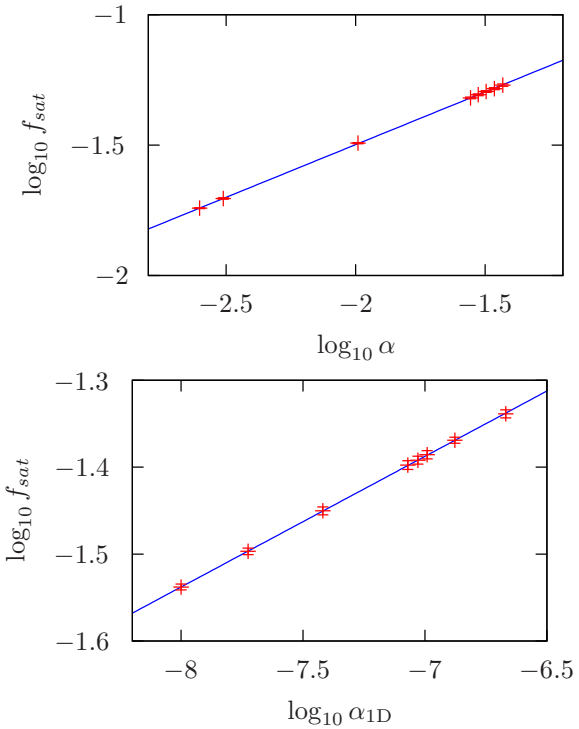

Figure 3.8: Numerical results for the saturated Rydberg fraction f_R in a 3D and a 1D setup: the system exhibits an algebraic behavior $f_R \sim \alpha^\nu$ with $\nu_{3D} \approx 0.404$ and $\nu_{1D} \approx 0.150$.

of the system by a local parameter $\alpha(\mathbf{r}) = \hbar\Omega/C_6 n(\mathbf{r})^2$ and the total Rydberg fraction f_R is given by ($d = 3$, $p = 6$)

$$f_R = \frac{1}{N}\int dr^3 f_R(\mathbf{r}) n(\mathbf{r}) \sim \frac{1}{(-2/\delta + 1)^{3/2}} \alpha^{1/\delta}. \tag{3.41}$$

Here, α is the peak value in the trap center $\alpha = \hbar\Omega/C_6 n(\mathbf{0})^2$. Consequently, we find that the critical exponent δ is not modified by the harmonic trapping potential within the local density approximation, and reduces to the value given in the thermodynamic limit.

As shown in Fig. 3.10 the saturated Rydberg fraction of the data presented in [Heidemann2007] also exhibits a data collapse to a single line, no matter whether the Rabi frequency Ω or the density n is varied. The obtained critical

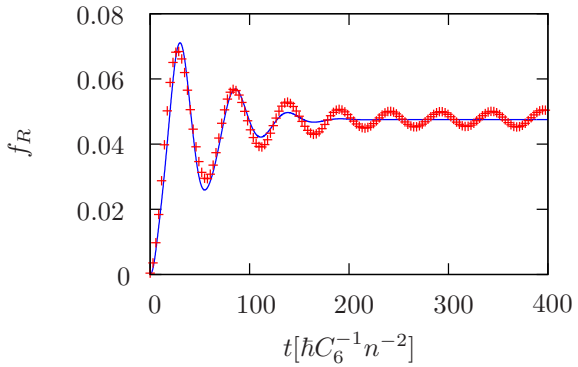

Figure 3.9: Numerical integration of the full Hamiltonian (crosses) for $\alpha = 1/36$, $N = 60$ and averaged over 50 different initial conditions. The remaining oscillations at large times are finite size effects. The solution of the master equation is shown as solid line.

exponent $\nu = 0.45 \pm 0.01$ is also in good agreement with mean-field theory and numerical simulations [Löw2009]. Furthermore, there is also a qualitative agreement of the prefactors between theory and experiment.

A similar analysis can be performed for the relaxation behavior to the stationary state. The inital increase in the number of Rydberg atoms is well described by a rate R, and this relaxation time is experimentally deduced by a fit of the time-evolution of the Rydberg excitation $N_R(t) = N f_R(t)$ by an exponential saturation function

$$N_R(t) = N_{sat}(1 - e^{-R\,t/N_{sat}}), \tag{3.42}$$

where N_{sat} is the equilibirum value of $N_R(t)$. In the strongly blocked regime ($\alpha \ll 1$) the rate R is determined by the collective Rabi frequency $f^{-1/2}\Omega$. For the dimensionless rate

$$g_R = \frac{\hbar R}{N C_p n^{p/d}} \tag{3.43}$$

mean-field theory predicts a scaling of the form $g_R \sim \alpha^{6/5}$. Note that the solution of the quantum master equation correctly reproduces this scaling behavior. As for the stationary state the initial $R \sim \alpha^\kappa$ also needs to be rescaled by a factor of $1/(-2\kappa + 3)$ to account for the inhomogeneity of the trapping potential. Fig. 3.11 presents the comparison between numerical simulations and experimental results. Again, there is a data collapse in both cases with

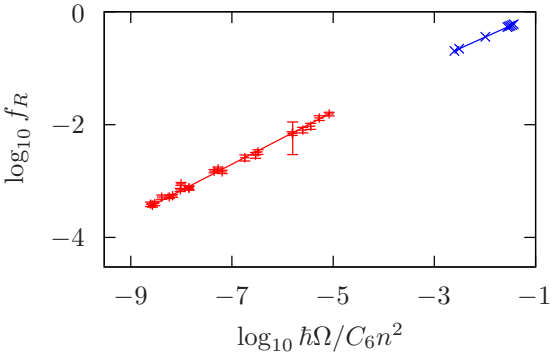

Figure 3.10: Universal scaling of the Rydberg fraction in the saturated excitation regime. The experimental data from [Heidemann2007] and numerical data are fitted (solid lines) to power laws of the form $f_R \sim \alpha^{1/\delta}$ from which the critical exponents $1/\delta = 0.45 \pm 0.01$ (exp.) and $1/\delta = 0.404$ (num.) are extracted.

the resulting critical exponents being close to the mean-field theory prediction.

Rotary echo Another possibility to compare theoretical predictions with experimental results are rotary echo sequences, where the coherence time of the system subject to internal and external dephasing processes is investigated. Examples of external dephasing are spontaneous emission and a finite laser linewidth, whereas the dephasing of the single particle coherence due to the van der Waals interaction acts as an internal dephasing mechanism. In such an echo setup the Rabi frequency changes sign at some time τ_p and the Rydberg fraction at the time τ is measured. In absence of any internal or external dephasing mechanisms the dynamics would be reversed, leading to $f_R(\tau = 2\tau_p) = 0$. Consequently, the Rydberg fraction serves as a good indicator of the coherence properties of the system. In the presence of dephasing the time τ can be chosen such that $f_R(\tau)$ is at a minimum. Defining the Rydberg fraction for the dynamics without flipping the Rabi frequency as f'_R we can define the visibility

$$v = \frac{f'_R(\tau) - f_R(\tau)}{f'_R(\tau) + f_R(\tau)}. \tag{3.44}$$

From mean-field theory we can expect v to be a function depending only on the intrinsic timescale $\alpha^{-2/5}\tau$. However, we cannot use the solution of

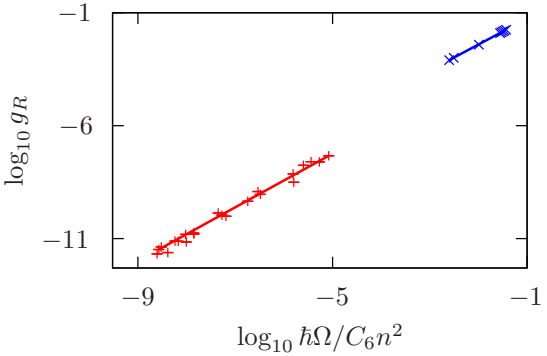

Figure 3.11: Universal scaling behavior of the excitation rate. The rescaled excitation rate g_R for a three dimensional density distribution is shown for experimental data taken from [Heidemann2007] and the corresponding numerical simulation. A linear fit to a power law $g_R \sim \alpha^\gamma$ results in a critical exponent of $\gamma = 1.25 \pm 0.03$ (exp) and $\gamma = 1.15$ (num).

the quantum master equation (3.26) as the short time behavior of the pair correlation is not modeled correctly. Fig. 3.12 shows the time evolution of a typical echo sequence and the scaling behavior of the visibility. As predicted by mean-field theory there is a data collapse when the visibility is expressed as a function of the intrinsic timescale.

The concept of the visibility can also be used to determine a (possibly time-dependent) dephasing rate γ_d, defined by the rate equation

$$\frac{\mathrm{d}}{\mathrm{d}\tau} v(\tau) = -\gamma_d(\tau) v(\tau). \tag{3.45}$$

Assuming $\gamma_d(\tau)$ to be a power law in τ we can directly express the rate up to a constant factor as

$$\gamma_d = -\frac{\log v}{\tau}. \tag{3.46}$$

The scaling of γ_d with the peak number of Rydberg atoms $\max(N_R)$ can then be compared to experimental data. An additional way to probe γ_d is by using a rate equation model and measure N_R in an using Electromagnetically Induced Transparancy (EIT) [Raitzsch2009]. As can be seen in Fig. 3.13 there is excellent agreement in this scaling between theory and experiment.

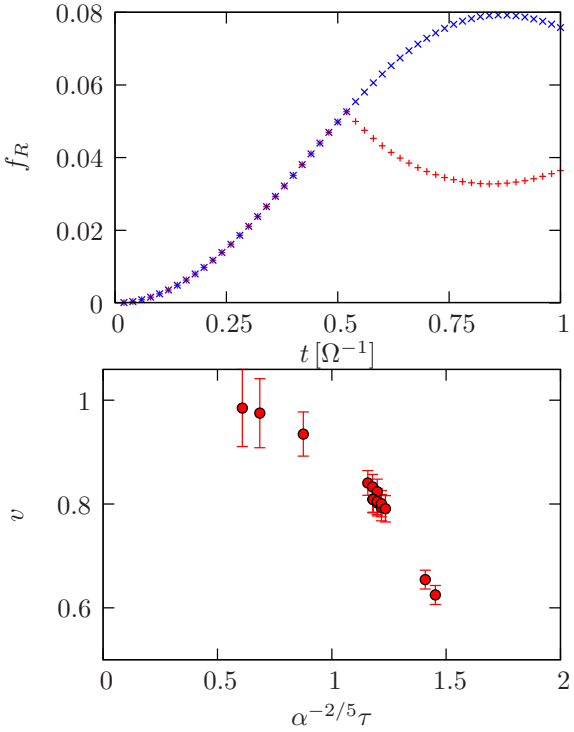

Figure 3.12: Numerical results for a rotary echo setup. (a) Time-evolution of the Rydberg fraction f_R with and without changing sign of the Rabi frequency at $t = 0.5\,\Omega^{-1}$. (b) Scaling of the visibility V for different times τ and different densities. As predicted by mean-field theory the visibility only depends on $\alpha^{-2/5}\tau$.

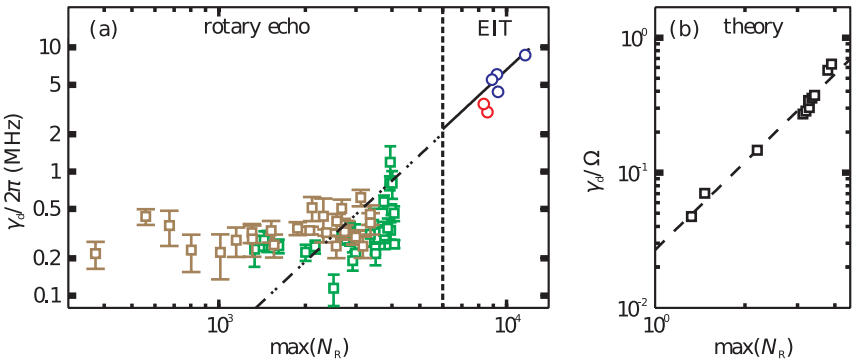

Figure 3.13: Comparison of the scaling of the dephasing rate γ_d with the maximum number of Rydberg atoms max(N_R) between theory and experiment (taken from [Raitzsch2009]. The experimental data was obtained both with a rotary echo and an EIT setup.

4 Strongly interacting Rydberg atoms in one dimension

Low-dimensional systems are often of special interest, for two reasons. First, the lower the dimension the stronger the effect of quantum fluctuations will be. Second, especially in one spatial dimensions many models become exactly solvable. In the case of strongly interacting Rydberg atoms studying one-dimensional systems is of particular interest, as the previous results hint at the possibility of a possible novel universality class with both a lower and upper critical dimension of one.

4.1 Rydberg excitations in one-dimensional lattices

One-dimensional lattices suitable for investigating Rydberg excitations can be created by standing laser waves forming an optical potential [Bloch2008], by magnetic trap arrays [Whitlock2009], or by building an array of micron-size thermal vapor cells [Kübler2010]. If the fluctuations around the lattice sites are much smaller than the blockade radius of the Rydberg interaction, it is possible to have N atoms per lattice site as one single superatom excitation [Olmos2009]. The only difference is that the Rabi frequency is enhanced by a factor of $\sqrt{N}$. Characteristic signatures of the different quantum phases can be detected by Bragg spectroscopy with a four-wave mixing technique [Brekke2008]. For a system with a lattice spacing a the Hamiltonian is given by

$$H = -\frac{\Delta}{2}\sum_i \sigma_z^{(i)} + \frac{\hbar\Omega}{2}\sum_i \sigma_x^{(i)} + \frac{C_p}{a^p}\sum_{j<i}\frac{P_{ee}^{(i)}P_{ee}^{(j)}}{(i-j)^p}. \tag{4.1}$$

4.2 Classical limit

4.2.1 Ground state properties

In the limit of vanishing Rabi frequency Ω the Hamiltonian (4.1) corresponds to a classical spin model, which in the case is an antiferromagnetic Ising chain

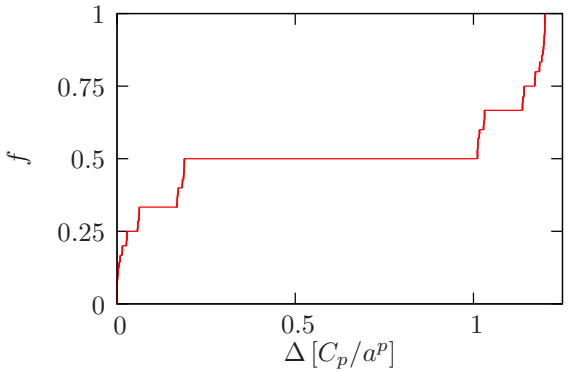

Figure 4.1: Ground state within the classical limit for a dipolar interaction ($p = 3$). Varying the detuning Δ leads to commensurate crystal fillings f according to a complete devil's staircase.

in a magnetic field. Such models have been studied extensively in the past and its ground state properties are exactly known [Bak1982]. In particular, the ground state is given by a complete devil's staircase of commensurable lattice fillings, see Fig. 4.1. The boundaries of one phase with filling factor $f = m/n$ is obtained by calculating the detuning for which the cost of adding or removing an excitation is zero. For x_i being the position of the ith Rydberg excitation the energy will be mimized if the separation of two excitations fulfills the relation

$$x_{q+i} - x_i = r_q \text{ or } r_q + 1, \tag{4.2}$$

with $r_q < nq/m < r_q + 1$ [Bak1982]. The boundary condititions furthermore require

$$\sum_i x_{q+i} = qN. \tag{4.3}$$

In the case of low fillings the quantity n/m can be well approximated by an integer value and we may write for the upper limit Δ_u

$$\Delta_u = \frac{C_p}{a^p} \sum_q \left[\left(\frac{n}{m}q + 1\right) \frac{1}{\left(\frac{n}{m}q\right)^p} - \frac{n}{m}q \frac{1}{\left(\frac{n}{m}q + 1\right)^p} + \frac{qn}{(qn-1)^p} - \frac{qn-1}{(qn)^p} - \frac{nq+1}{(nq)^p} + \frac{nq}{(nq+1)^p} \right] \tag{4.4}$$

Analogously, computing the lower boundary Δ_l yields

$$\Delta_l = \frac{C_p}{a^p}\sum_q \left[\left(\frac{n}{m}q+1\right)\frac{1}{\left(\frac{n}{m}q\right)^p} - \frac{n}{m}q\frac{1}{\left(\frac{n}{m}q+1\right)^p} + \frac{qn+1}{(qn)^p} - \frac{qn}{(qn+1)^p} - \frac{nq+1}{(nq)^p} + \frac{nq}{(nq+1)^p}\right] \tag{4.5}$$

The center of the phase is then given by $\Delta_0 = (\Delta_u + \Delta_d)/2$, which in the limit of low filling ($n \to \infty$) turns out to be

$$\Delta_0 = \frac{(p+1)\zeta(p)C_p}{a^p}\left(\frac{m}{n}\right)^p, \tag{4.6}$$

which is exactly the same result as obtained in the continuum limit. The width of the phase $\Delta_w = \Delta_u - \Delta_d$ is

$$\Delta_w = \frac{p(p+1)\zeta(p+1)C_p}{n^{p+1}a^p}. \tag{4.7}$$

Since Δ_w depends only on the denominator n for a given chemical potential the largest width will be found for $m = 1$. Then, by using Eq. (4.6) we can express Δ_w as

$$\Delta_w = A_p \frac{a}{C_p^{1/p}}\Delta_0^{1+1/p}, \tag{4.8}$$

with A_p being a numerical constant depending only on p.

4.2.2 Excitations: fractionalized defects

The energy cost associated with flipping a single spin is associated with a typical energy of Δ. However, we have already seen from the ground state calculations that the boundary of a commensurable phase is given by the much smaller energy scale Δ_w. Hence, spin flips correnspond to a high-energy excitations. The low-energy excitations are characterized by topological defects that are obtained when redistributing the spins after the spin flip such that the interaction energy is minimal. As can be seen in Fig. 4.2, flipping one spin in a system with filling fraction f creates $1/f$ defects, i.e., these excitations exhibit fractional statistics.

4.3 Phase diagram in one dimension

Next, we focus on the regime with a finite drive $\Omega \neq 0$, we derive an effective Hamiltonian describing the defect dynamics. The melting of the commensu-

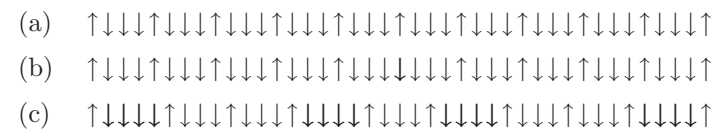

Figure 4.2: (a) Ground state of the system with $f = 1/4$. (b) High-energy excitation obtained by flipping a single spin. (c) Low-energy excitation consisting of $1/f$ topological defects.

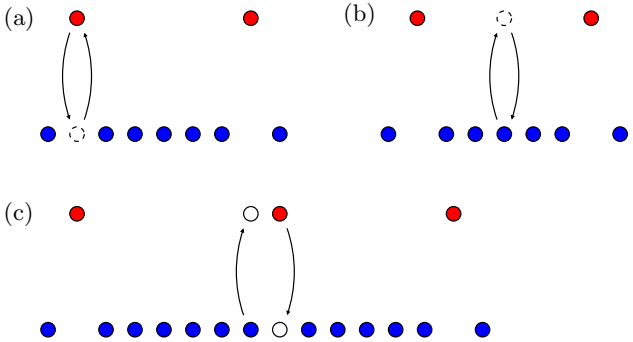

Figure 4.3: Processes in second order perturbation theory. (a) Virtual annihilation of a Rydberg excitation. (b) Virtual creation of a Rydberg excitation. (c) Hopping of a crystal defect.

rate crystals then arises naturally as the nucleation and subsequent condensation of defects. Here, it is important to stress that the driven dynamics is very different to a massive dynamics normally present due to the kinetic energy of the atoms. Nevertheless, we will demonstrate in the following, that the driven dynamics gives rise to a hopping of the defects. For a large detuning $\Delta \gg \Omega$ the system has a well-defined energy gap and we can derive an effective low-energy Hamiltonian for the defects within perturbation theory in Ω/Δ using canonical transformations [Klein1974]. For explicity, we focus on the case of a van der Waals interaction with $p = 6$.

4.3.1 Defect Hamiltonian

For simplicity, we first restrict our treatment to three states: (i) the crystalline ground state $|c\rangle$, (ii) the state $|p_i\rangle$ with a particle-like defect between the Rydberg excitation x_i and x_{i+1}, i.e., $x_{i+1}-x_i = 1/f-1$, and (iii) the analogous state $|h_i\rangle$ for a hole-like defect. In second order perturbation theory,

the effective Hamiltonian contains diagonal terms, shown in Fig. 4.3(a), and Fig. 4.3(b), while the particle (hole) defects also acquire a off-diagonal term corresponding to a hopping process of the defect, see Fig. 4.3(c). Adding a constant energy such that $E_c = 0$ the diagonal terms take the form

$$\langle\alpha|H_{\rm eff}|\alpha\rangle = E_\alpha + \sum_{x_i} \frac{\hbar^2\Omega^2}{E_\alpha - E_i^{(a)}} + \sum_{j\notin\{x_i\}} \frac{\hbar^2\Omega^2}{E_\alpha - E_j^{(b)}}. \tag{4.9}$$

Here, $E_j^{(a)}$ and $E_j^{(b)}$ correspond to the energies of the virtual levels depicted in Fig. 4.3(a-b), which take the form

$$\begin{aligned} E_i^{(a)} - E_\alpha &= -\frac{C_6}{a^6}\sum_{x_j\neq x_i}\frac{1}{|x_i - x_j|^6} + \hbar\Delta, \qquad (4.10)\\ E_j^{(b)} - E_\alpha &= \frac{C_6}{a^6}\sum_{x_i}\frac{1}{|x_i - j|^6} - \hbar\Delta. \end{aligned}$$

Consequently, the diagonal terms provide an additional shift in the excitation energy for the particles and holes,

$$\Delta E_p = \langle p_i|H_{\rm eff}|p_i\rangle - \langle c|H_{\rm eff}|c\rangle - E_p \tag{4.11}$$

$$\Delta E_h = \langle h_i|H_{\rm eff}|h_i\rangle - \langle c|H_{\rm eff}|c\rangle - E_h. \tag{4.12}$$

This energy shift can be evaluated to

$$\begin{aligned} \Delta E_p = \sum_j &\frac{\Omega^2}{\sum_q \frac{C_6}{(qa_R - ja - a)^6} + \frac{C_6}{[(q-1)a_R + ja]^6} - \Delta} \\ &- \frac{\Omega^2}{\sum_q \frac{C_6}{(qa_R - ja)^6} + \frac{C_6}{[(q-1)a_R + ja]^6} - \Delta}, \end{aligned} \tag{4.13}$$

and analogously for holes. For $f \ll 1$ we may replace the sum over j by an integral and expand this expression up to first order in a/a_R, which with the help of $\Delta = 7\zeta(6)C_6/a_R^6$ allows us to cast the energy shift into the form $\Delta E_p = -\Delta E_h = I_p\Omega^2/Delta$. The value of I_p can be computed numerically, e.g, up to the term with $q = 1$ of the rapidly converging series we find

$$I_p^{q=1} = \int_0^1 \frac{{\rm d}x\,\zeta(6)^{-2}6x^{12}(1-x)^5}{\left[(1-x)^6 + x^6\right]^2 - 7x^6(1-x)^6\left[2(1-x)^6 + 2x^6 - 7x^6(1-x)^6\right]}. \tag{4.14}$$

Including terms with $q > 1$ finally results in $I_p \approx 0.090$. On the other hand, the off-diagonal defect hopping for holes reduces to

$$J_h = \langle h_i | H_{\text{eff}} | h_{i\pm1} \rangle = \frac{\hbar^2\Omega^2}{E_h - E_i^{(c_1)}} + \frac{\hbar^2\Omega^2}{E_h - E_i^{(c_2)}}, \tag{4.15}$$

where the first process annihilates a Rydberg excitation at position x_i with the subsequent creation of the Rydberg excitation at position $x_i \pm 1$, while the second term reverses the order of creation and annihilation; the energies $E_i^{(c_1)}$ and $E_i^{(c_2)}$ of the virtual excitation are expressed in analogy to Eq. (4.10). Finally, the corresponding term J_p for the hopping of particle defects is obtained similarly, and the numerical evaluation of the second order processes provides $J_p = K_p\hbar\Omega^2/\Delta$ and $J_h = K_h\hbar\Omega^2/\Delta$ with $K_p \approx K_h \approx -7/5$. The hopping of the defects therefore leads to a delocalization and provides the dispersion relation $E_p(k) = E_p + \Delta E_p - 2J_p \cos ka$, and analogous for $E_h(k)$.

The on-site energy of a defect is given by $\mu_p = E_p + \Delta E_p$, which scales for multiple defects like $\mu_p n^2$. while the hopping matrix elements have the same strength $J = J_p$ in the limit $f \ll 1$. Note, that the power law decay of the microscopic interaction potential also gives rise to a defect interaction at larger distances. However, these terms are suppressed by a factor 1/64 compared to the on-site repulsion and can safely be ignored. In summary, the defect Hamiltonian is then given by

$$\begin{aligned} H_{\text{eff}} =& \mu_p \sum_i \sum_{n=0}^{\infty} n^2 |n\rangle\langle n|_i + \mu_h \sum_i \sum_{n=-\infty}^{0} n^2 |n\rangle\langle n|_i \\ & - J \sum_i \sum_{mnp} |n\rangle\langle n+p|_i \otimes |m+p\rangle\langle m|_{i+1}. \end{aligned} \tag{4.16}$$

4.3.2 Hard-core limit

Speaking in terms of the Bose-Hubbard model we have for the on-site repulsion $U = 2\mu$. In the limit of low defect densities particle and hole defects decouple and the effective Hamiltonian reduces to the hard-core limit of the Bose-Hubbard model,

$$H_{\text{eff}} = \frac{\mu}{2} \sum_i \sigma_z^{(i)} - J \sum_i \left(\sigma_+^{(i)} \sigma_-^{(i+1)} + \text{h.c.} \right). \tag{4.17}$$

Here, μ takes the role of a chemical potential. This Hamiltonian can be solved exactly by mapping the system onto free fermions by a Jordan-Wigner

transformation [Sachdev1999]. The defect density is then given by

$$n = \begin{cases} 0 & J \leq \mu/2 \\ \frac{1}{\pi} \arccos \frac{\mu}{2J} & J > \mu/2 \end{cases} . \tag{4.18}$$

From this we can see that there is a continuous quantum phase transition from a gapped commensurable crystal without defects to a gapless phase with a finite defect density, see Fig. 4.4.

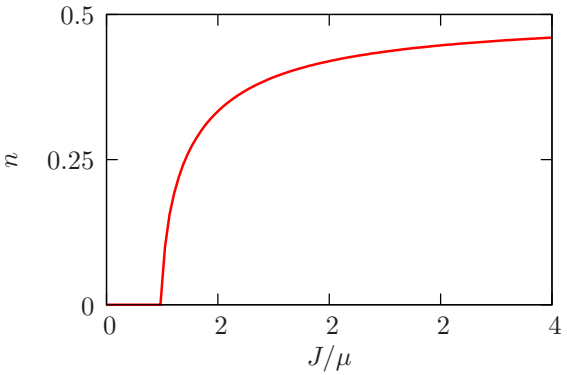

Figure 4.4: Quantum phase transition at the critical defect hopping $J_c = \mu/2$ from a gapped commensurate crystal to a gapless phase with finite defect density n.

To understand the properties of the gapless phase it is instructive to look at its correlation functions. The pair correlation of the defects is simply given by the correlation of free fermions, i.e.,

$$g_2(r_i - r_j) = 1 - \frac{\sin^2[k_F(r_i - r_j)]}{k_F^2(r_i - r_j)^2}, \tag{4.19}$$

with the Fermi wavevector $k_F = n\pi$. This clearly shows that the defects form a (quasi-)crystalline arrangement, with algebraic decay of the correlations.

However, it is important to stress that the physical quantity describing the properties of this novel phase is given by the spin-spin correlation $\langle P_{ee}^{(i)} P_{ee}^{(j)} \rangle$ rather than the defect correlations $\langle n_i n_j \rangle$. Consequently, we have to provide a mapping, which allows us to calculate the physical quantity from the effective fermionic model. The defect density n_i can be expressed in terms of the position of the Rydberg atoms as

$$n_i = x_{i+1} - x_i - \frac{1}{f}. \tag{4.20}$$

For simplicity we choose boundary conditions such that $x_0 = 0$. For $i \neq 0$ the position of the ith Rydberg excitation depends on the presence of defects at previous sites, therefore we introduce the total defect number $N_i = \sum_{j=0}^{i-1} n_j$. Then, a Rydberg excitation is found at site j when any multiple of the original spacing $1/f$ is equal to j after accounting for the defects, i.e.,

$$P_{ee}^{(j)} = \sum_k \delta_{j,k/f+N_k}. \tag{4.21}$$

Analytically obtaining the spin-spin correlations from the defect correlation function (4.19) and the defect-spin mapping s still a prohibitive task. However, it is possible to perform numerical simulations with correlated random numbers [Qaqish2003]. As can be seen from the results in Fig. 4.5 there is also an algebraic decay in the spin correlation function. This means that the gapless phase is characterized by an incommensurable crystal. Furthermore, this implies that the crystalline phase exists also in one spatial dimension, meaning that the previously discussed paramagnet-crystal phase transition belongs to a universality class with a lower critical dimension $d_c = 1$. The spin correlation oscillates on short scales with the original spacing a_R with superimposed oscillations with integer multiples of the effective lattice spacing $a/(1/f + n)$.

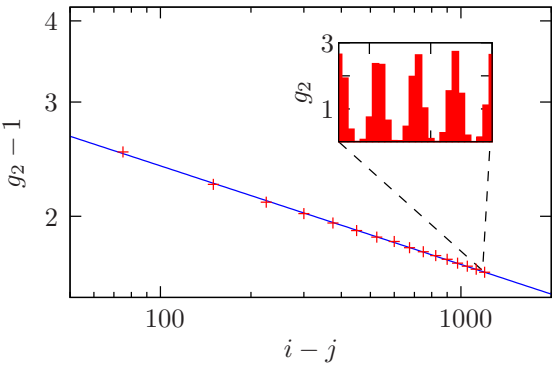

Figure 4.5: Algebraic decay of the spin correlations from Monte-Carlo simulations with up to 1200 lattice sites ($a_R = 6a, n = 0.25$). The inset shows the pair correlation at large distances with persistent strong oscillations.

4.3.3 Beyond the hard-core limit

Since the hard-core limit is only valid for small defect hopping J it is natural to ask what happens when the hopping becomes stronger. Physically, hopping gets larger when the Rabi frequency Ω is increased. For $\Omega \gg C_6/a^6 \gg \Delta$ the spin Hamiltonian (3.1) reduces to the Ising model in both a transverse and a longitudinal field. In the limit of large Ω the system is deep in the paramagnetic phase [Ovchinnikov2003], where the spin-spin correlations decay exponentially. Conversely, there exists a phase transition separating the incommensurate crystal and the paramagnet.

The defect Hamiltonian does not exhibit a quantum phase transition for large J. Therefore, the expected transition can only take place after the breakdown of the perturbation series leading to the effective Hamiltonian. This happens when the quadratic fluctuations around the lattice points $\langle n^2 \rangle$ become comparable to the lattice spacing a_R, which is nothing but the Lindemann criterion

$$\sqrt{\langle n^2 \rangle} a = \frac{a_R}{\tilde{L}} \tag{4.22}$$

with the constant $\tilde{L}$ being the Lindemann parameter [Kleinert1989]. To find the critical value of $\langle n^2 \rangle$ we employ a Gutzwiller ansatz of the form

$$|\psi\rangle = \prod_i \sum_n a_n |n\rangle_i, \tag{4.23}$$

leading to the variational energy

$$E_{var} = \mu \sum_n n^2 a_n^2 - J \sum_p \left(\sum_n a_{n+p} a_n \right)^2. \tag{4.24}$$

where the a_n are real numbers since the Perron-Frobenius theorem implies that adding any phase will result in a higher energy. Minimizing with respect to a_n under the constraint $\sum_n a_n^2 = 1$ yields

$$-4J \sum_p a_p + 2\mu n^2 a_n = \lambda a_n, \tag{4.25}$$

where λ is a Lagrange multiplier. In the following we treat n as a continuous variable and replace sums by integrals. We define $A_0 \equiv \int \mathrm{d}n a(n)$ and obtain by solving the last equation for $a(n)$,

$$a(n) = \frac{2A_0 \mu J}{\mu n^2 - \lambda}. \tag{4.26}$$

Comparing with the definition of A_0 thus yields

$$\lambda = -\frac{4\pi^2 J^2}{\mu}. \tag{4.27}$$

The value of A_0 is determined by the normalization constraint, i.e.,

$$A_0 = 2\pi\sqrt{\frac{J}{\mu}}. \tag{4.28}$$

Plugging all results together we finally arrive at

$$\langle n^2 \rangle = 4\pi^2 \frac{J^2}{\mu^2}. \tag{4.29}$$

This finally allows us to determine the scaling of the critical detuning

$$\Delta_c \sim \left(\frac{C_6}{a^6}\right)^{1/13} \Omega^{12/13}, \tag{4.30}$$

which is exactly the same result that was predicted previously using the universal scaling function in Sect. 3.4. This agreement between the two different approaches strongly supports that the mean-field predictions give the correct critical exponents and thus the transition belongs to a universality class with an upper critical dimension $d^c = 1$.

For quantum systems, we typically have a Lindemann parameter $\tilde{L} \approx 10$ [Kleinert1989], which allows us to determine the phase boundary. The complete phase diagram is shown in Fig. 4.6. In addition to the prediction by the universal scaling function we also find the commensurate crystal lobes due to the lattice spacing a constituting an additional length scale. Note that this phase diagram is also in good agreement with recent numerical results obtained for the spin Hamiltonian (3.1) at high fillings using the time-evolving block decimation algorithm [Schachenmayer2010].

4.3.4 Effects of disorder

As a final remark, we want to discuss the consequences for the phase diagram in the presence of disorder, i.e., when the system is not aligned on a perfect lattice. Qualitative results can be obtained by taking the continuum limit $a \to 0$ while keeping the hopping energy of a *particle* J/f fixed. For the commensurate-incommensurate transition we find due to the relation $J_c/f = \mu/(2f) \sim a$ that the commensurate crystals vanish in a disordered system. However, the Lindemann criterion is independent of a in the continuum limit and thus the phase boundary of the incommensurate crystal remains unchanged.

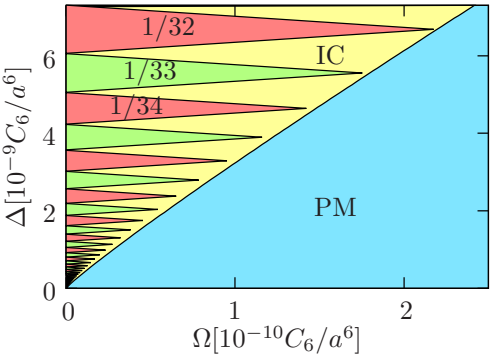

Figure 4.6: Phase diagram of strongly interacting Rydberg atoms in a one-dimensional lattice. There are three different phases: a commensurable crystal with different filling factors f, an incommensurable crystal (IC), and a paramagnet (PM).

Part III

Creating strongly correlated states with Rydberg atoms

What I cannot create, I do not understand.

Richard Feynman

5 Mesoscopic Rydberg gate based on Electromagnetically Induced Transaparency

Highly excited Rydberg atoms are a promising candidate for the controlled coherent manipulation of quantum systems due to their strong interactions and long coherence times [Saffmanto be published]. In this chapter, we propose a many-body quantum gate that in contrast to previous proposals involving Rydberg atoms [Jaksch2000, Lukin2001, Brion2007] allows to entangle a mesoscopic amount of qubits with a single laser pulse sequence. Our proposed method makes use of a two-photon interference phenomenon known as Electromagnetically Induced Transparancy (EIT) [Fleischhauer2005]. We discuss a possible application of the quantum gate as a single atom transistor.

5.1 Proposed setup

The general setup for the implementation of the quantum gate is shown in Fig. 5.1. We consider a single control atom and N ensemble atoms. For our proposal we need that the control atom can be addressed independently of the ensemble atoms, but we do not need individual addressing of the ensemble atoms. The required addressing can be acheived by spatial separation of control and ensemble atoms, by choosing a different atom species for the control atom, or by using different hyperfine ground states for the encoding of quantum information. Each atom posesses two hyperfine ground state, $|0\rangle$ and $|1\rangle$ for the control atom, $|A\rangle$ and $|B\rangle$ for the ensemble atoms, respectively. Then, by coupling to strongly interacting Rydberg states with external laser fields we realize a Controlled-NOT^N (CNOT^N) gate, defined by

$$\begin{aligned} |0\rangle|A^N\rangle &\rightarrow |0\rangle|A^N\rangle, \quad |0\rangle|B^N\rangle \rightarrow |0\rangle|B^N\rangle, \\ |1\rangle|A^N\rangle &\rightarrow |1\rangle|B^N\rangle, \quad |1\rangle|B^N\rangle \rightarrow |1\rangle|A^N\rangle, \end{aligned} \tag{5.1}$$

where $|A^N\rangle = \prod_i |A\rangle_i$ is the product state of all N ensemble atoms being in the $|A\rangle$ hyperfine state and $|B^N\rangle$ is defined analogously.

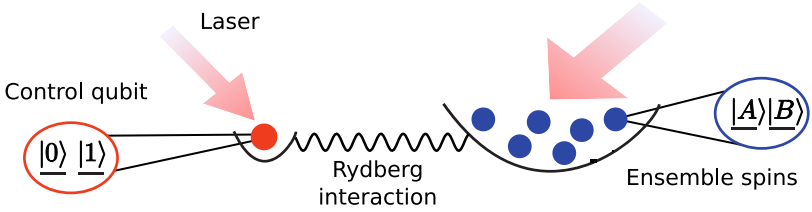

Figure 5.1: Proposed setup for the mesoscopic quantum gate. A single control atom can be addressed independently of N ensemble atoms. Laser excitations induce a Rydberg interaction between control and ensemble atoms, leading to the realization of a mesoscopic quantum gate.

5.2 Laser pulse sequence

For realizing the mesoscopic quantum gate we introduce additional internal levels in both control and ensemble atoms. The control atom has an auxillary Rydberg state $|r\rangle$ that can be coupled to the hyperfine state $|1\rangle$ by an external laser. In the ensemble atoms we employ two additional levels. First, there is a coupling characterized by a time-dependent Rabi frequency $\Omega_p(t)$ between the hyperfine ground states $|A\rangle$ and $|B\rangle$ and an intermediate non-Rydberg $|P\rangle$ level, which still has a low principle quantum number such that interactions with the $|r\rangle$ level of the control atom are negligible. Furthermore, we also use a Rydberg state $|R\rangle$ in each ensemble atom that can be coupled to the intermediate $|P\rangle$ state with a Rabi frequency Ω_c. The external laser fields are chosen such that there is a detuning Δ from the $|P\rangle$ level, however, the hyperfine ground states and the Rydberg state are on two-photon resonance. Fig. 5.2 shows a graphical representation of the internal atomic structure and the laser pulse sequence. The laser pulse sequence depicted in Fig. 5.3 starts with a π pulse on the control atom, transforming the state $\alpha|0\rangle + \beta|1\rangle$ to $\alpha|0\rangle + \beta|r\rangle$, followed by an adiabatic Raman transfer in which $\Omega_p(t)$ is varied according to

$$\Omega_p(t) = \Omega_{p,max} \sin^2\left(\frac{\pi t}{T}\right), \tag{5.2}$$

where the pulse time T in given by

$$T = \frac{16\pi}{3}\frac{\Delta}{\Omega_{p,max}^2}. \tag{5.3}$$

Finally, the initial π pulse is reversed by a second one.

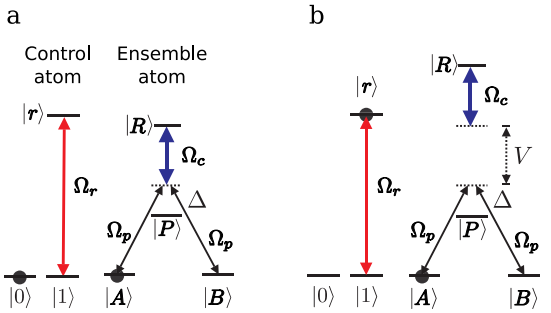

Figure 5.2: Atomic level structure and external laser couplings for the mesocopic gate. The states $|1\rangle$ and $|r\rangle$ in the control atom are coupled by a laser with Rabi frequency Ω_r. The weak laser fields $\Omega_p(t)$ drives a Raman transitions from $|A\rangle$ to $|B\rangle$ in the ensemble atoms. (a) For the control atom in $|0\rangle$ the Raman lasers and the strong coupling laser Ω_c coupling to the $|R\rangle$ state are on two-photon resonance. (b) For the control atom in $|r\rangle$ the Rydberg interaction shifts the $|R\rangle$ level away from the two-photon resonance.

In the following we study the consequences on the ensemble atoms in two cases, with the control atom being in $|0\rangle$ and $|r\rangle$, respectively. The full dynamics then follows by taking the superposition according to the coefficients α and β.

5.2.1 Effective single-atom Hamiltonian

Let us first assume that the ensemble atoms do not interact with each other; consequences of non-vanshing interactions will be discussed later. Then, the dynamics of the ensemble atoms reduces to the product of independent evolution of a single ensemble atom. For large detuning Δ we may adiabatically

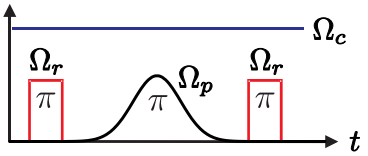

Figure 5.3: Laser pulse sequence for the mesoscopic gate consisting of an initial π pulse on the control atom, an adiabatic Raman transfer in the ensemble atoms, and a second π pulse on the control atom.

eliminate the $|P\rangle$ level and obtain the effective Hamiltonian

$$H_{\text{eff}} = \frac{\Omega_c^2}{4\Delta}\left[x^2\,|+\rangle\langle+| \;+\; (1+V)\,|R\rangle\langle R| \;+\; x\Big(\,|+\rangle\langle R| + \text{h.c.}\Big)\right]. \qquad (5.4)$$

Here, $|+\rangle = (|A\rangle+|B\rangle)/\sqrt{2}$ is the symmetric superposition of the two hyperfine ground states, $x(t) = \sqrt{2}\Omega_p/\Omega_c$ defines the relative strength of the proble laser Ω_p to the coupling laser Ω_c. The interaction term V accounts for the state of the control atom; in an ideal situation we have $V = 0$ for the control atom in $|0\rangle$ while for the control atom in $|r\rangle$ we have a dominant Rydberg interaction, i.e., $V = \infty$.

As the antisymmetric state $|-\rangle = (|A\rangle + |B\rangle)/\sqrt{2}$ is not present in the Hamiltonian we immediately see that this is a zero energy dark state, i.e, it will be unaffected by the dynamics.

5.2.2 Blockade of population transfer

For $V = 0$ we find a second zero energy dark state,

$$|d\rangle = (1+x^2)^{-1/2}[|+\rangle - x\,|R\rangle], \qquad (5.5)$$

which for $t = 0$ corresponds to the $|+\rangle$ state. The second eigenstate has the energy $E_2 = 1+x^2$, thefore the system will adiabatically follow the zero energy dark state for weak coupling lasers with $x \ll 1$ and smooth laser pulse shapes $\Omega_p(t)$. As the states $|+\rangle$ and $|-\rangle$ are both zero energy dark states the transfer of population from $|A\rangle$ to $|B\rangle$ via the Raman transition is blocked.

5.2.3 Lifting the blockade

In the case of $V = \infty$ the Rydberg level will be far off-resonant and hence it also does not take part in the dynamics. Then, the time evolution is trivial according to the Hamiltonian $H = \Omega^2/(4\Delta)x^2|+\rangle\langle+|$. Choosing the pulse shape of $\Omega_P(t)$ such that $\int x^2 = \pi$ the system will undergo the transformation

$$\begin{aligned} |-\rangle &\rightarrow |-\rangle \\ |+\rangle &\rightarrow -|+\rangle. \end{aligned} \qquad (5.6)$$

Expressing this transformation in the original states $|A\rangle$ and $|B\rangle$ results in

$$|A\rangle \rightarrow -|B\rangle \qquad (5.7)$$

$$|B\rangle \rightarrow -|A\rangle, \qquad (5.8)$$

which is the desired operation up to a trivial phase factor, which can be corrected by choosing suitable phases of the laser fields.

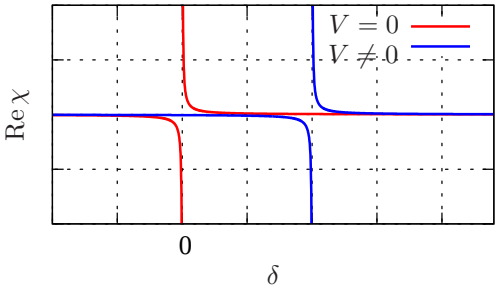

Figure 5.4: Real part of the linear susceptibility χ as a function of the detuning δ from the two-photon resonance. For $V = 0$ the system fulfills the EIT condition characterized by a pole in χ, while for $V \gg 1$ the EIT condition is shifted far away from the two-photon resonance.

Consequently, we have established a way to control a NOT operation in the ensemble atoms conditioned on the state of the control atom, thus implementing the CNOT^N gate. The observed blocking and enabling of population transfer can also be interpreted in terms of an EIT scenario. For $V = 0$ the two-photon resonance leads to an EIT condition where the system is 'transparent', i.e., it is unaffected by the photons of the probe laser field Ω_p driving the Raman transfer from $|A\rangle$ to $|B\rangle$. However, for large V this EIT condition is lifted and thus the tranfer may take place. Fig. 5.4 shows the linear susceptibility χ as a function of the detuning δ from the two-photon resonance.

5.3 Error sources

So far the discussion was concentrated on a perfect scenario. However, the usability of the proposed quantum gate for scalable quantum information processing crucially depends on the consequences of imperfections. As a measure of the consequences of errors, we consider the fidelity f for the preparation of a "Schrödinger cat" state, i.e.,

$$|\psi_{SC}\rangle = \frac{1}{\sqrt{2}}(|0\rangle|A^N\rangle + |1\rangle|B^N\rangle). \tag{5.9}$$

The fidelity is then given by $f = \mathrm{Tr}\{|\psi_{SC}\rangle\langle\psi_{SC}|\rho(T)\}$ with $\rho(T)$ being the state of the system at the end of the laser pulse sequence. For pure states $|\psi(T)\rangle$ this reduces to the well-known form $f = |\langle\psi_{SC}|\psi(T)\rangle|^2$.

5.3.1 Single atom errors

Radiative decay An obvious source of errors arises from radiative decay of the Rydberg level of the control atom. For a decay rate γ_r much smaller than the frequency of the gate operation $1/T$ the fidelity behaves like

$$f = 1 - \gamma_r T. \tag{5.10}$$

A similar type of error arises due to radiative decay of the intermediate $|P\rangle$ level in the ensemble atoms. Here, a decay rate of γ_P will result in the fidelity

$$f = 1 - N\pi\frac{\gamma_p}{2\Delta}. \tag{5.11}$$

The radiative decay of the Rydberg level $|R\rangle$ is supressed by a factor x_{max}^2 as the Rydberg state is never populated in the adiabatic limit.

Coherent error sources The errors arising from radiative decay contribute to the decoherence, i.e., the system can no longer be described in terms of a pure state. However, there is also the possibility of fully coherent imperfections, which we will discuss in the following. Important sources of such coherent errors are due to a finite interaction strength V, which can be studied in second order perturbation theory. The phase ϕ written on each ensemble atom during the time evolution according to the Hamiltonian (5.4) is given by

$$\phi = \pi\frac{V}{V+1}. \tag{5.12}$$

This allows us to compute the fidelity for the production of the target state

$$f = 1 - \frac{\pi^2}{8}\frac{N}{V^2}. \tag{5.13}$$

5.3.2 Ensemble-ensemble interaction

So far, the discussed errors were limited to single atom errors. However, many-body effects can be expected to play an important role as well. The second dark state $|d\rangle$ has a contribution from the Rydberg level $|R\rangle$. However, the Rydberg levels of the ensemble atoms will also exhibit strong interactions, meaning that the many-body state $|d^N\rangle$ is not a dark state of the full many-body Hamiltonian. If the control atom is in $|r\rangle$ this will not be a problem as a repulsive ensemble-ensemble interaction will only lead to an increase of the effective interaction V, thus making the gate even more reliable. Therefore,

we only need to concentrate on the case where the control atom is in $|0\rangle$ and we want the transfer to be blocked.

To quantify the relevance of this error, we perform a superatom calculation, similar to the one presented in Sect. 3.3.4. Mathematically, a superatom approach is essentially a truncation of the accessible Hilbert space to only a few relevant states. Such a truncation may be justified in the case of strong interactions of the type

$$\hat{V}^{(i,j)} = V_{ij} P^{(i)} P^{(j)}, \tag{5.14}$$

where $P^{(i)}$, $P^{(i)}$ are projection operators acting on atoms i and j, respectively. If the initial state of the system contains no excitations, i.e, $\sum_i \langle \psi(t = 0)|P^{(i)}|\psi(t = 0)\rangle = 0$, then we can expect that the states relevant for the dynamics are restricted to the state manifold with few excitations. Here, it is convenient to introduce the symmetric states $|S(N_R)\rangle$, which contain N_R Rydberg excitations, given by

$$|S(N_R)\rangle = \binom{N}{N_R}^{-1/2} \mathcal{S}|+^{N-N_R} r^{N_R}\rangle, \tag{5.15}$$

where $\mathcal{S}$ denotes the symmetric sum. In particular, we have

$$|S(0)\rangle = |+_1, +_2, \ldots, +_N\rangle \tag{5.16}$$

$$|S(1)\rangle = \frac{1}{\sqrt{N}} \sum_i |+_1, \ldots, r_i, \ldots, +_N\rangle \tag{5.17}$$

$$|S(2)\rangle = \sqrt{\frac{2}{N(N-1)}} \sum_{i=1}^{N} \sum_{j=1}^{i-1} |+_1, \ldots, r_i, \ldots, r_j, \ldots, +_N\rangle. \tag{5.18}$$

Additionally, one can compute the off-diagonal elements

$$\langle S(0)| \sum_i^N \sigma_x^{(i)} |S(1)\rangle = \sqrt{N} \tag{5.19}$$

$$\langle S(1)| \sum_i^N \sigma_x^{(i)} |S(2)\rangle = \sqrt{2(N-1)}. \tag{5.20}$$

After adiabtic elimination of the $|P\rangle$ levels of the ensemble atoms, we may write the many-body Hamiltonian as a sum of local terms and an interaction part,

$$H = \sum_i^N H_{\text{eff}}^{(i)} + \sum_{i,j} V_{ij} P^{(i)} P^{(j)}, \tag{5.21}$$

where $H_{\text{eff}}^{(i)}$ is given by Eq. (5.4) and $V_{ij} = |R\rangle\langle R|_i \otimes |R\rangle\langle R|_j$. In the following we take the interaction to be constant between all atoms, i.e., $V_{ij} = V_{ee}$. Then, we can write the superatom Hamiltonian H_S containing up to two excitations using only the states $\{|S(0)\rangle, |S(1)\rangle, |S(2)\rangle\}$ as all non-symmetric states are dark. This yields

$$H_S = \begin{pmatrix} Nx^2 & \sqrt{N}x & \\ \sqrt{N}x & 1+(N-1)x^2 & \sqrt{2(N-1)}x \\ & \sqrt{2(N-1)}x & V_{ee}+2+(N-2)x^2 \end{pmatrix}. \tag{5.22}$$

In leading order in x the ground state of H_S has the energy

$$E_0 = N(N-1)x^4\left(1-\frac{2}{V_{ee}}\right). \tag{5.23}$$

The same result can be obtained using a 'grey states' aproach [Müller2009]. Thus even in the limit $V_{ee} \to \infty$ the error is suppressed for small x, in which case the phase imprint is given by

$$\phi = \int_0^T \mathrm{d}t E_0 = N(N-1)\phi_0 = \frac{35}{48}\pi N(N-1)x_{\max}^2. \tag{5.24}$$

This expression gives the phase error in the worst case, which occurs for the state $|+^N\rangle$. For each ensemble atom in the $|-\rangle$ state this phase error is reduced as the $|-\rangle$ state is still dark. The resulting phase error then depends number of atoms in the $|+\rangle$ state, e.g, the state $|-++-\rangle$ will pick up a phase error $\phi = N_+(N_+-1)\phi_0 = 2\phi_0$. For the preparation of $|\psi_{SC}\rangle$ we first consider the overlap with the state $|A^N\rangle$,

$$\langle A^N|\psi(T)\rangle = \frac{1}{2^N}\sum_{m=0}^{N}\binom{N}{m}\exp[-im(m-1)\phi_0]. \tag{5.25}$$

In the limits $N \gg 1$ and $Nx \ll 1$ we can simplify this expression with the help of the binomial theorem and a few lines of algebra (see App. A) to

$$\langle A^N|\psi(T)\rangle = \frac{1}{\sqrt{2}}\left[1 - iN(N+1)\frac{\phi_0}{4} - (N^4+6N^3)\frac{\phi_0^2}{32}\right], \tag{5.26}$$

which yields for the fidelity

$$f = 1 - N^3\frac{\phi_0^2}{8}. \tag{5.27}$$

5.4 A single-atom transistor

A possible application of the proposed many-body gate besides quantum computing is the amplification of a single atom signal, i.e, to use the control atom as a single-atom tranistor. The goal of this Rydberg transistor is to produce atoms in the $|B\rangle$ state if there is a Rydberg atom nearby, and to leave the atoms in $|A\rangle$ otherwise. Therefore, it is useful to use the N-atom visibility

$$v_N = N\frac{f_{\text{transfer}} - f_{\text{block}}}{f_{\text{transfer}} + f_{\text{block}}}, \tag{5.28}$$

as a measure of the amplification, where N denotes the number of transfered atoms, f_{transfer} and f_{block} the respective fidelities. Note that in this notation $f_{\text{block}} = 0$ implies perfect blocking.

Transfer fidelity As a simple estimate of N we can use the number of atoms within the sphere where the dimensionless interaction V is larger than one, i.e., for a van der Waals interaction described by a C_6 coefficient we have

$$N = 8\pi\frac{n_g}{\Omega_c}\sqrt{\frac{\Delta C_6}{\hbar}}. \tag{5.29}$$

If we also include radiative decay processes in both control and ensemble atoms we obtain for the transfer fidelity

$$f_{\text{transfer}} = 1 - \gamma_r T - \gamma_P\frac{\pi}{2\Delta}. \tag{5.30}$$

Blocking fidelity The blocking fidelity will be limited due to the ensemble-ensemble interaction. We can operate the system in two different regimes. First, we can try to make $N(N-1)\phi_0$ in (5.24) as small as possible. Then the transfer probability for each atom can be computed from its reduced density matrix,

$$\rho_1 = \text{Tr}_{N-1}\{\rho\} = \begin{pmatrix} \frac{1}{2} & \frac{1}{2^N}[1+\exp(-2\text{i}\phi_0)]^{N-1} \\ \frac{1}{2^N}[1+\exp(2\text{i}\phi_0)]^{N-1} & \frac{1}{2} \end{pmatrix}, \tag{5.31}$$

leading to

$$f_{\text{block}} = \frac{1}{2} + \text{Re}\,\frac{1}{2^N}\left(1+\exp(-2\text{i}\phi_0)\right)^{N-1}. \tag{5.32}$$

However, if $N(N-1)\phi_0$ is large, the expansion of the ground state energy of the superatom Hamiltonian breaks down. In this case we can expand the ground state for large N,

$$E_0 = N_+ x^2 - \sqrt{N_+}x - (x^2-1)/2, \tag{5.33}$$

where N_+ is the number of $|+\rangle$ bits in the binary representation of each state. Since the dynamical phase shift is only relevant up to multiples of 2π each state essentially picks up a random phase, leading to the reduced density matrix

$$\rho_1 = \begin{pmatrix} 1/2 & \\ & 1/2 \end{pmatrix}, \tag{5.34}$$

and therefore $f_{\text{block}} = 1/2$.

Detailed examples If we want a fully coherent amplifier (i.e., $N(N-1)\phi \ll 1$), experimentally achievable parameters according to [Heidemann2007] would be $n = 20$, $\Omega_c = 2\pi \times 60\,\text{MHz}$, $\Omega_p = 2\pi \times 12\,\text{MHz}$, $\Delta = 2\pi \times 100\,\text{MHz}$, $n_g = 4 \times 10^{18}\,\text{m}^{-3}$, which would finally result in $N \approx 10$ and an amplification of $v_N \approx 7$.

However, if we work in the incoherent regime ($N(N-1)\phi \gg 1$), a realistic parameter set is $n = 43$, $\Omega_c = 2\pi \times 20\,\text{MHz}$, $\Omega_p = 2\pi \times 10\,\text{MHz}$, $\Delta = 2\pi \times 200\,\text{MHz}$, $n_g = 2 \times 10^{19}\,\text{m}^{-3}$. This involves $N \approx 10^4$ transfered atoms and thus results in an amplification of $v_N \approx 5000$. Figure 5.5 illustrates the effect of this amplification in two dimensions.

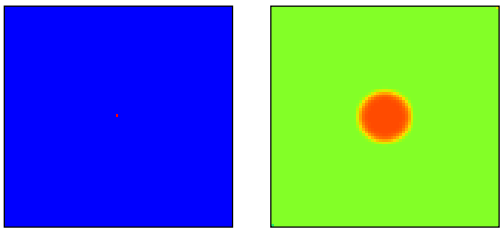

(a) (b)

Figure 5.5: Amplification of a single Rydberg excitation in a 2D plane. (a) At the beginning one single Rydberg atom sits at the center. (b) After the amplification scheme a large number of atoms have been transfered to the $|B\rangle$ state. Note that far away from the impurity there is a background noise of 50% coming from ensemble-ensemble interactions in the incoherent regime. The effect of finite control-ensemble interaction strength is also included.

6 Digital coherent and dissipative quantum simulations

Simulating quantum mechanics on classical computers is often a hard if not impossible task as the Hilbert space of the system grows exponentially with the number of particles. Therefore, in 1982, Richard Feynman came up with his famous idea to use a different quantum system to mimic the behavior of the simulated system [Feynman1982]. Of course, this requires that the quantum simulator is easier to implement experimentally than the simulated system and the simulator being tunable enough to truly reproduce the desired behavior. The requirements for the second aspect were discussed by Seth Lloyd a few years later [Lloyd1996], leading to the concept of a universal quantum simulator (UQS), which is a controlled quantum device that efficiently reproduces the dynamics of any other many particle quantum system with short range interactions. However, proposals for experimentally realistic quantum simulators have largely been focused on systems two-body interactions [Sørensen1999]. Here, we present a proposal for a UQS for spin models involving high order N-body interactions [Weimer2010]. The main building block for the quantum simulator is the mesoscopic Rydberg gate presented in the previous chapter.

6.1 Simulation of Hamiltonian dynamics

As a paradigmatic example, we want to focus on the simulation of a Hamiltonian involving four spin 1/2 particles given by

$$H = -E_0 \sigma_x^{(1)} \sigma_x^{(2)} \sigma_x^{(3)} \sigma_x^{(4)} \equiv -E_0 A_p. \tag{6.1}$$

The Hamiltonian has two distinct eigenenergies, which correspond to the eigenvalues $+1$ and -1 of the operator A_p. We introduce an additional control atom that is needed to mediate this four-body interaction using the mesoscopic Rydberg gate. The general approach then consists of three steps (see Fig. 6.1): (i) We first perform a gate sequence G which encodes the information whether the four spins are in a $+1$ or -1 eigenstate of A_p in the two internal states of the auxiliary atom. (ii) In a second step, we apply a gate operation that acts on the internal states of the control qubit. Due to the previous mapping

these manipulations of the control qubit are equivalent to manipulations on the subspaces with fixed eigenvalues of A_p. (iii) Finally, the mapping G is reversed, by which the control qubit is re-initialized coherently in its internal state $|0\rangle$. Optical pumping of the control atom can be included to perform this reinitialization incoherently in the presence of gate errors.

The mapping G is a sequence of three gate operations

$$G = R_y^{(c)}(\pi/2)^{-1} U_g R_y^{(c)}(\pi/2), \tag{6.2}$$

where $R_y^{(c)}(\pi/2) = \exp(-i\pi\sigma_y^{(c)}/4)$ is a standard $\pi/2$-single qubit rotation of the control qubit and the many-body Rydberg gate takes the form

$$U_g = |0\rangle\langle 0|_c \otimes \mathbf{1} + |1\rangle\langle 1|_c \otimes A_p. \tag{6.3}$$

For the control qubit initially prepared in $|0\rangle_c$, the gate G coherently transfers the control qubit into the state $|1\rangle_c$ ($|0\rangle_c$) for any system state $|\lambda, -\rangle$ ($|\lambda, +\rangle$), with $|\lambda, \pm\rangle$ denoting the eigenstates of A_p, i.e., $A_p|\lambda, \pm\rangle = \pm|\lambda, \pm\rangle$, see Fig. 6.1.

For the simulation of Hamiltonian dynamics, the application of a phase shift $\exp(i\phi\sigma_c^z)$ on the control qubit and the subsequent reversion of the gate, G^{-1}, implements the time evolution according to the many-body interaction A_p, i.e.,

$$U = \exp(i\phi A_p) = G^{-1} \exp(i\phi\sigma_c^z)\, G. \tag{6.4}$$

The control qubit returns to its initial state $|0\rangle_c$ after the complete sequence and therefore effectively factors out from the dynamics of the system spins. For small phase imprints $\phi \ll 1$, the mapping reduces to the standard equation for coherent time evolution

$$\partial_t \rho = -\frac{i}{\hbar} E_0 \; [-A_p, \rho] + o(\phi^2). \tag{6.5}$$

The energy scale for the four-body interaction A_p becomes $E_0 = \hbar\phi/\tau$ with τ the time required for the implementation of a single time step.

In our scheme the characteristic energy scale of the many-body interaction terms is essentially the same for two-body, four- or higher-order interaction terms, and mainly limited by the fast time-scale to perform the parallel mesoscopic Rydberg gate operations. We note that this is in contrast to the familiar analog simulation of Hubbard and spin dynamics of atoms in optical lattices [Anderlini2007, Trotzky2008]. where collisional interactions between atoms provide naturally two-body interactions, while higher order, small effective interactions and constraints are typically derived with perturbative arguments [Johnson2008].

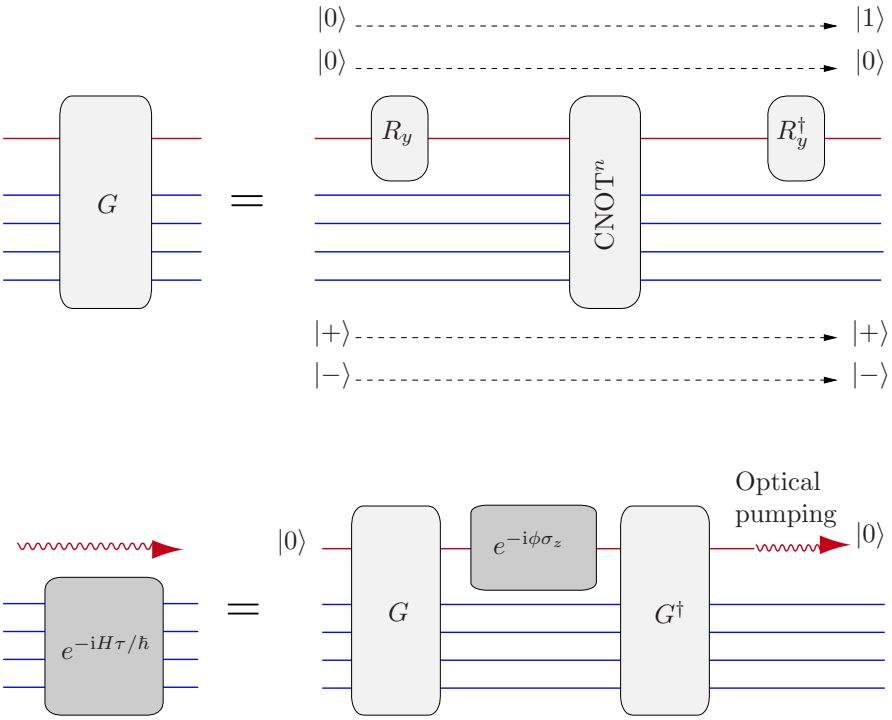

Figure 6.1: Gate sequences for the simulation of Hamiltonian dynamics. The eigenstates of the simulated many-body interaction are mapped onto the internal states of the control qubit. Using this mapping the phase ϕ written onto the control atom gets transfered onto the ensemble spins.

6.2 Dissipative state preparation

The proposed setup also allows for a realization of dissipative dynamics that can be used to efficiently cool into the many-body ground state of interacting spin systems. The main idea is to engineer the dynamics in a way that all states of the ground state manifold are dark state of the jump operators c_p of the arising quantum master equation, which is realized for the Hamiltonian (6.1) by the jump operator

$$c_p = \frac{1}{2}\sigma_z^{(i)}\left[1 - A_p\right], \tag{6.6}$$

where $\sigma_z^{(i)}$ acts on an arbitrary spin i. The jump operator is readily understood as an operator which pumps from -1 into $+1$ eigenstates of the stabilizer operators: the 'interrogation' part $(1-A_p)/2$ is a projector onto the eigenspace of A_p with -1 eigenvalue, while all states in the $+1$ eigenspace are dark states.

The choice of the jump operator follows the idea of reservoir engineering of interacting many-body systems as discussed in Ref. [Diehl2008, Kraus2008]. In contrast to alternative schemes for measurement based state preparation [Aguado2008], here, the cooling is part of the time evolution of the system.

The desired jump operator can be implemented by using the same mapping G as for the coherent simulation. However, instead of applying a phase rotation $\exp\left(i\phi\sigma_c^z\right)$ onto the control atom, we perform a controlled spin flip onto one of the four system spins,

$$U_{Z,i}(\theta) = |0\rangle\langle 0|_c \otimes \mathbf{1} + |1\rangle\langle 1|_c \otimes \Sigma \tag{6.7}$$

with $\Sigma = \exp(i\theta\sigma_i^z)$. As desired, the sequence $G^{-1}U_{Z,i}(\theta)G$ leaves the low energy sector $|\lambda,+\rangle$ invariant since these states are mapped onto $|0\rangle_c$ and are therefore unaffected by $U_{Z,i}(\theta)$. In contrast - with a certain probability - the sequence performs a controlled spin flip on the states $|\lambda,-\rangle$. Once a spin is flipped, the auxiliary qubit remains in the state $|1\rangle_c$, and optical pumping from $|1\rangle_c$ to $|0\rangle_c$ is required to re-initialize the system, guaranteeing that the control qubit again factors out from the system dynamics. The optical pumping constitutes the dissipative element in the system and allows one to remove entropy in order to cool the system. The two qubit gate $U_{Z,i}(\theta)$ is implemented in close analogy to the many-body Rydberg gate U_g. For small phases θ the operator Σ can be expanded, and the density matrix ρ of the spin system evolves in one dissipative time step according to the Lindblad form

$$\partial_t\rho = \kappa\left[c_p\rho c_p^\dagger - \frac{1}{2}\left\{c_p^\dagger c_p\rho + \rho c_p^\dagger c_p\right\}\right] + o(\theta^3) \tag{6.8}$$

with the jump operators c_p given in Eq. (6.6) and the cooling rate $\kappa = \theta^2/\tau$. Note, that the cooling also works for large phases θ, and therefore the most efficient dissipative state preparation is achieved with $\theta = \pi$.

6.3 Toolbox for quantum simulations

Let us now proceed to generalize the presented methods for coherent and dissipative quantum simulation. Besides the possibility to simulate arbitrary N-body interactions the most important application of the quantum simulator will come after scaling the system up to a lattice involving many quasi-local interaction of the form of A_p.

Competing interaction parts can be combined by a Trotter expansion

$$e^{-iH\tau/\hbar} \approx \prod_{\alpha} e^{-iH_\alpha \tau/\hbar} \tag{6.9}$$

and a certain error associated with the particular choice of operator splitting arising from the non-commutativity of the quasi-local interactions H_α. The concept of stroboscopic time evolution is readily adapted to the dissipative case by interspersing coherent propagation and dissipative time steps

$$e^{\mathcal{L}\tau} \approx \prod_{\beta} e^{\mathcal{D}(c_\beta)\tau}, \tag{6.10}$$

providing an overall simulation of the master equation by sweeping over the whole lattice with our coherent and dissipative operations. Many of these steps can in principle be done in a highly parallel way, rendering the time for a simulation step independent on the system size.

The implementation of the digital quantum simulations provides full control on the spatial and temporal interaction strengths. Therefore, if one wishes to analyze the quantum phases of a system for arbitrary interaction strenghts, there are two different strategies: (i) The possibility to vary the different coupling strengths in time allows us adiabatically explore the phase diagram of the simuklted system (ii) On the other hand, the spatial control of the coupling parameters allows us to divide the lattice into a system and a bath. The ground state of the bath is given by a state that can be continuously cooled via the dissipative terms, while the system part is sympathetically cooled due to its contact with the bath; in analogy to the cooling well known in condensed matter systems.

6.3.1 Framework for N-body interactions

We can readily include arbitrary many-body interactions between the system spins surrounding the control atom. Gate operations on single system spins allow to transform σ_i^x in σ_i^y and σ_i^z, while selecting only certain spins to participate in the many-body gate via local addressability gives rise to the identity operator for the non-participating spins. Consequently, we immediately obtain the implementation of the general many-body interaction and jump operators

$$A_\alpha = \prod_i W_i, \tag{6.11}$$

$$c_\beta = \frac{1}{2} Q_i \left[1 - \prod_j W_j \right] \tag{6.12}$$

with $W_i, Q_i \in \{1, \sigma_i^x, \sigma_i^y, \sigma_i^z\}$. Here, α and β stand for a collection of indices characterizing the position of the local interaction and the interaction type. Note that A_α also includes single particle terms, as well as two-body interactions.

6.3.2 Lattice systems

Extending the analysis to a large lattice system with different, possibly non-commuting interaction terms in the Hamiltonian, i.e., $H = \sum_\alpha E_\alpha A_\alpha$ and dissipative dynamics described by a set of jump operators c_β with damping rates κ_β, provides a complete toolbox for the quantum simulation of many-body systems. Each term is characterized by a phase ϕ_α (θ_β) written during a single time step determining its coupling energy $E_\alpha = \hbar\phi_\alpha/\tau$ and damping rate $\kappa_\beta = \theta_\beta^2/\tau$. For small phases $\phi_\alpha \ll 1$ and $\theta_\beta^2 \ll 1$, the sequential application of the gate operations for all interaction and damping terms reduces to the master equation of Lindblad form,

$$\partial_t \rho = -\frac{i}{\hbar}[H, \rho] + \sum_\beta \kappa_\beta \left[c_\beta \rho c_\beta^\dagger - \frac{1}{2}\left(c_\beta^\dagger c_\beta \rho + \rho c_\beta^\dagger c_\beta \right) \right]. \tag{6.13}$$

The choice of the different phases during each time step allows for the control of the relative interaction strength of the different terms, as well as the simulation of inhomogeneous and time dependent systems.

The characteristic energy scale for the interactions E_α and damping rates κ_β are determined by the ratio between the time scale τ required to perform a single time step, and the phase difference ϕ_α and θ_β written during these

time steps. It is important to stress that within our setup, the interactions are quasi-local and only influence the spins surrounding the control qubit. Consequently, the lattice system can be divided into a set of sublattices on which all gate operations that are needed for a single time step τ, can be carried out in parallel. Then, the time scale for a single step τ becomes independent on the system size and is determined by the product of the number z of such sublattices and the duration τ_s of all gate operations on one sublattice. In our setup, τ_s is mainly limited by the duration of the many-body Rydberg gate U_g, which is on the order of $\sim 1\mu$s (see Sect. 6.6 for details). We have to apply the many-body gate twice for every interaction term (see Fig. 6.1), and for a system consisting of two sublattices and two competing interaction terms with $z = 4$, we obtain $\tau \sim$ a few μs, resulting in characteristic energy scales and cooling rates of the order of hundred kHz. For the simulation of Hamiltonian dynamics this energy scale may be somewhat lower if Trotterization errors have to be taken care of. It is a crucial aspect of this quantum simulation with Rydberg atoms that it can be performed fast and is compatible with current experimental time scales of cold atomic gases [Bloch2008].

Finally, we would like to point out that imperfect gate operations provide in leading order small perturbations for the Hamiltonian dynamics and weak dissipative terms. However, the thermodynamic properties and the dynamical behaviour of a strongly interacting many-body system are in general robust to small perturbations in the Hamiltonian. In many cases these perturbations will be related to some effective temperature. Then the important question will be if this effective temperature of the system is lower than the critical temperature of the quantum phase under consideration. In this regime small imperfections in the implementation of the gate operations are tolerable. This is in strong contrast to quantum simulations using a quantum computer, where quantum error correction [Shor1995] is required.

6.3.3 Measurement of correlation functions

An important aspect for the characterization of the final state is the measurement of correlation functions $\chi = \langle A_{\alpha_1} \dots A_{\alpha_n} \rangle$, where A_{α_j} denote local, mutually commuting many-body observables. In our scheme, the observables A_{α_j} can be measured via the mapping G of the system information onto auxiliary qubits and their subsequent state selective detection. In analogy to noise correlation measurements in cold atomic gases [Fölling2005, Altman2004] the repeated measurement via such a detection scheme provides the full distribution function for the observables, and therefore allows to determine the correlation function χ in the system.

6.4 Implementation of spin models

In the following, we will present a detailed treatment of two many-body spin models as an illustration of the procedure for performing coherent and dissipative quantum simulations within the proposed method. The first model is Kitaev's toric code featuring anyonic excitations, whereas the second example presents an implementation of a $U(1)$ lattice gauge theory where a confinement-deconfinement transition can be studied.

6.4.1 Kitaev's toric code

The toric code is a paradigmatic spin model on a square lattice involving four-body interactions [Kitaev2003]. The Hamiltonian of the system is given by

$$H = -E_0 \left(\sum_i A_p^{(i)} + \sum_j B_s^{(j)} \right), \tag{6.14}$$

with the "site" term $B_s = \sigma_z \sigma_z \sigma_z \sigma_z$, see Fig. 6.2.

Ground state degeneracy As the Hamiltonian is a sum of mutually commuting stabilizer operators Σ_i [Gottesman1996], its ground state is simply given by the constraints $\langle \psi | \Sigma_i | \psi \rangle = 1 \; \forall i$, allowing to exactly solve the system. Flipping all spins of a plaquette (site) by a $\sigma_x \sigma_x \sigma_x \sigma_x$ ($\sigma_z \sigma_z \sigma_z \sigma_z$) operation

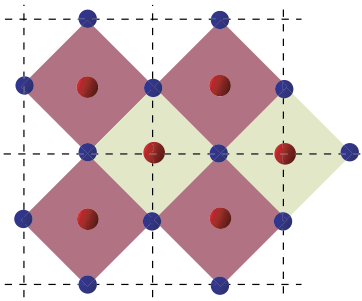

Figure 6.2: Lattice model for the implementation of the toric code with control atoms and ensemble atoms being represented by red and blue dots, respectively. The plaquettes involving the A_p are shown as red squares, while the site terms B_s act on the atoms on the edges of the green squares.

will not change the energy of the system, hence there is a $Z_2 \times Z_2$ lattice gauge symmetry. For periodic boundary conditions on a torus this results in the ground state being four-fold degenerate.

Anyons and the braid group Excitations of the toric code Hamiltonian are violations of the stabilizer constraints an have energy gap of $2E_0$ as every violation will affect two sites or plaquettes, respectively. There are two different types of excitations. Violations of a constraint involving A_p are called "magnetic charges", while excitations of the B_s operators are "electric charges". In the following we will illustrate these excitations for the magnetic charges, but due to the symmetry of the Hamiltonian the situation is identical for the electric charges.

Flipping a single spin will create two magnetic charges located on adjacent plaquettes, see Fig. 6.3. By flipping a different spin on one of the plaquettes the excitations can be effectively moved. The excitations are no longer quasi-local, but must be described by a string operator involving the path along which the charge has been moved. By flipping several spins we also may move a magnetic charge around an electric charge; due to the non-commutativity of σ_x and σ_z the state will eventually pick up a phase of π. This behavior shows that the quasiparticles describing magnetic or electric charges neither have bosonic nor fermionic character as in both cases one would expect to recover the identity once the particle had been returned to its initial position. Hence, one calls such particles with exotic statistics "anyons" related to their potential to pick up "any" phase under particle exchange.

The apparent contradiction to the proof that there can only be fermions

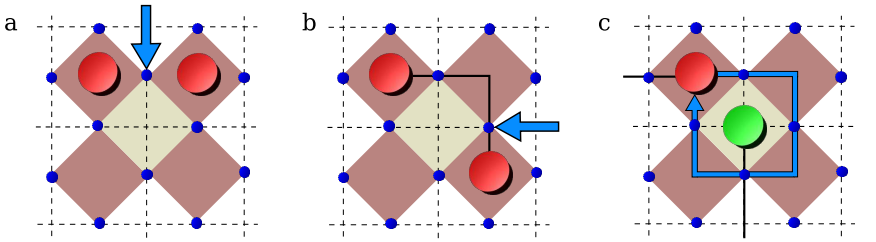

Figure 6.3: Excitations in the toric code. (a) Flipping the spin indicated by the arrow will create two magnetic charges on the adjacent plaquettes. (b) Charges can be moved around by flipping further spins on the plaquettes containing the charges. The string operator characterizing the non-local excitation is shown as a solid line. (c) Moving a magnetic charge around an electric charge.

and bosons stems from that we are working in three spacetime dimensions. In four spacetime dimensions moving one particle around the other can be reduced to the identity; therefore the permutation group is the correct group describing the process. However, this reduction is not possible in three spacetime dimensions, where the process must be described using the braid group. Then, the way of one particle around the other is relevant and the system can pick up a phase $e^{i\phi}$. Colloquially, this dependence on dimensionality is expressed as "there are no knots in four dimensions".

The toric code as a quantum memory The fourfold degeneracy of the ground state presents a possiblity to store two qubits. Furthermore, one ground state can only be transformed in another by applying a string operator that moves anyonic excitations around the whole torus. As the excitations are gapped, such a process is highly improbable and thus it was proposed to use the toric code as a self-correcting quantum memory. Unfortunately, the two-dimensional version of the toric code is not stable against thermal fluctuations, with a self-correcting memory only being possible in four dimensions and higher [Dennis2002, Alicki2009].

Dissipative ground state cooling We will now discuss how to employ the proposed method for dissipative state preparation for the ground state of the toric code. The auxillary control atoms are located in the center of the plaquettes and sites, respectively. Then, the dissipative state preparation is performed by sweeping alternately over all sites and plaquettes with operations involving different plaquettes or sites done in parallel. We may partition the system in four sublattices characterized by a checkerboard pattern of sites and plaquettes. As during each timestep the many-body gate has to be applied twice the total time for each timestep during is essentially given by $\tau = 8\tau_s$.

The jump operators give rise to a random walk of anyonic excitations on the lattice, and whenever two excitations of the same type meet they are annihilated, resulting in a cooling process. The resulting dynamics is shown in Fig. 6.4 for various system sizes with N atoms. For perfect many-body gates the system reaches the ground state in the long time limit, while for imperfect gates heating events can occur and a finite density of anyons n remains present. This finite anyon density corresponds to an effective temperature

$$T_{\text{eff}} = -\frac{E_0}{k_B \log n}. \tag{6.15}$$

Furthermore, the gate errors also result in additional terms in the Hamiltonian as discussed in Sect. 6.5, which correspond to a magnetic field and an Ising

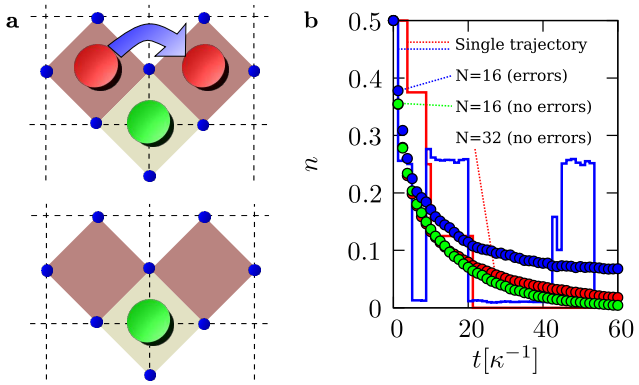

Figure 6.4: Cooling of the toric code: a) A dissipative time step moves one anyonic excitation (red dot) on top of a second anyon sitting on a neighboring plaquette, annihilating each other and thus lowering the internal energy of the system. The anyon of different type (green dot) is unaffected as moves of anyons occur only with a small probability. b) Numerical simulation of the cooling for N lattice sites (periodic boundary conditions). Single trajectories for the anyon density n over time are shown as solid lines. Filled circles represent averages over 1000 trajectories. The initial state for the simulations is the fully polarized, experimentally easily accessible state of all spins down. The difference between perfect and imperfect gates (blue circles) is apparent, with a finite anyon n remaining in the imperfect case. In this example the phase shift determining the cooling rate was set to $\theta = 1.25$.

interaction. For weak magnetic fields the stability of the toric code has recently been shown [Vidal2009].

Relation to other spin models The toric code can also be derived as a perturbative limit of a Hamiltonian with two-body interactions on a honeycomb lattice [Kitaev2006], of which implementations have been suggested both for cold atoms [Duan2003] and condensed matter systems [Jackeli2009]. In contrast to our approach, where the higher-order interactions arise in a non-perturbative way, the required interaction strengths typically raise severe constraints on the experimental feasibility of the setup. Additionally, our proposed escheme also allows for a direct preparation of the many-body ground state via dissipative cooling. Our proposed method can also be readily generalized to more complex stabilizer states and to setups in higher dimensions, as in, e.g., the color code [Bombin2006].

6.4.2 U(1) lattice gauge theory

In the second example we will show that our approach can also be extended to systems with non-commuting terms in the Hamiltonian. As an example, we focus on a three-dimensional $U(1)$-lattice gauge theory [Kogut1979], and show that dissipative ground state cooling can also be achieved in more complex models. Such models have attracted a lot of recent interest in the search for 'exotic' phases and spin liquids [Levin2005]. The three-dimensional setup consists of spins located on the links of a cubic lattice (see Fig. 6.5). The lattice structure for the spins can be viewed as a corner sharing lattice of octahedra with one site of the cubic lattice in the center of each octahedra. The Hamiltonian for the $U(1)$ lattice gauge theory takes the form

$$H = U \sum_o \left(S_o^z\right)^2 - J \sum_p B_p + V\, N_{RK}, \tag{6.16}$$

where the first term in the Hamiltonian defines a low energy sector consisting of allowed spin configuration with an equal number of up and down spins on each octahedron, i.e., spin configurations with vanishing total spin $S_o^z = \sum_{i\in o} \sigma_i^z$ on each octahedron. The second term denotes a ring exchange interaction on each plaquette with

$$B_p = S_1^+ S_2^- S_3^+ S_4^- + S_1^- S_2^+ S_3^- S_4^+, \tag{6.17}$$

here $S_i^{\pm} = \left[\sigma_i^x \pm i\sigma_i^y\right]/2$ and the numbering is clockwise around the plaquette. This correlated hopping term flips a state with alternating up and down spins on a plaquette, i.e., $|\uparrow,\downarrow,\uparrow,\downarrow\rangle_p \rightarrow |\downarrow,\uparrow,\downarrow,\uparrow\rangle_p$. The last term denotes the the so-called Rokhsar-Kivelson term, which counts the total number of flipable plaquettes $N_{RK} = \sum_p B_p^2$. While the ring exchange interaction commutes with the octahedron constraint, ring exchange terms on neighboring plaquettes are non-commuting. At the Rokhsar-Kivelson point with $J = V$, the system becomes exactly solvable [Rokhsar1988], and it has been proposed that in the regime $0 \leq V \leq J$ the ground state is determined by a spin liquid smoothly connected to the Rokhsar-Kivelson point [Hermele2004]: the properties of this spin liquid are given by an artificial 'photon' mode, gapped excitations carrying an 'electric' charge (violation of the constraint on an octahedron), which interact with a $1/r$ Coulomb potential mediated by the artificial photons, and gapped magnetic monopoles.

In the following, we present the implementation of this Hamiltonian within our scheme for the digital quantum simulation and demonstrate that dissipative ground state cooling can be achieved at the Rokhsar-Kivelson point. The control qubits reside in the center of each octahedron (on the lattice sites of

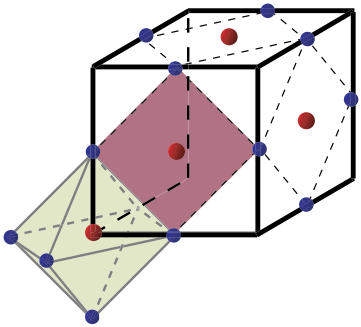

Figure 6.5: Spatial arrangement of control atoms (red dots) and ensemble atoms (blue dots) for the implemenatation of the $U(1)$ lattice gauge theory. An octahedron and a plaquette is shown as a green and red area, respectively.

the 3D cubic lattice) controlling the interaction on each octahedron, and in the center of each plaquette for the ring exchange interaction B_p, see Fig. 6.5. Then, the coherent time evolution of the Hamiltonian (6.16) can be implemented in analogy to the above discussion by noting that the ring exchange interaction B_p and N_{RK} can be written as a sum of four-body interactions of the form of Eq. (6.11), while the constraint on the octahedra can be expressed as a sum of Ising interactions,

$$(S_o^z)^2 = \sum_{i\neq j}^{6} \sigma_i^z \sigma_j^z + \text{const}, \tag{6.18}$$

which allow for an efficient implementation using the general toolbox for quantum simulation.

Cooling into the octahedron constraints The implementation for the jump operators for the octahedron constraint is obtained in analogy to the general jump operators with the many-body gate U_g replaced by the gate

$$U_g' = |0\rangle\langle 0|_c \otimes \mathbf{1} + |1\rangle\langle 1|_c \otimes \prod_i \exp(i\frac{\pi}{6}\sigma_i^z). \tag{6.19}$$

The cooling into the subspace with an equal number of up and down spins on each octahedron is then obtained by the jump operator

$$c_s = \frac{1}{4}\left[1 + \prod_j e^{-i\frac{\pi}{6}\sigma_j^z}\right]\sigma_i^x\left[1 - \prod_j e^{i\frac{\pi}{6}\sigma_j^z}\right], \tag{6.20}$$

where the product is carried out over the six spins located on the corners of the octahedron (see Fig. 6.5). The "interrogation" part $1 - \prod_j \exp(i\frac{\pi}{6}\sigma_j^z)$ of the jump operator vanishes if applied to any state with three up and three down spins, while in all other cases a spin is flipped. Then the cooling follows in analogy to the cooling in the toric code by the diffusion of the 'electric' charges.

Dissipative preparation of the Rokhsar-Kivelson state Identifying each spin up with a 'dimer' on the link, all states satisfying the constraints on the octahedra can be viewed as a dimer covering with three dimers meeting at each site of the cubic lattice. Within this description, the ground state at the Rokhsar-Kivelson point is given by the condensation of the dimer coverings [Levin2005], i.e., the equal weight superposition of all dimer coverings. The condensation of the dimer coverings is then achieved by the jump operator

$$c_p = \frac{1}{2}\sigma_i^z\left[1 - B_p\right]B_p. \tag{6.21}$$

This jump operator has two dark states, which are the 0 and +1 eigenstates of B_p. The 0 eigenstate corresponds to a non-flippable plaquette, e.g., a plaquette in the state $|\uparrow,\uparrow,\downarrow,\uparrow\rangle$. The +1 eigenstate is the equal weight superposition of the original dimer covering and the dimer covering obtained by flipping the plaquette [i.e., the state $(|\uparrow,\downarrow,\uparrow,\downarrow\rangle + |\downarrow,\uparrow,\downarrow,\uparrow\rangle)/\sqrt{2}$]. Finally, the jump operator c_p transforms the third eigenstate with eigenvalue -1 into the +1 eigenstate. After acting on all plaquettes, the system is cooled into the dark state which is the equal superposition of all dimer coverings, which can be reached by flipping different plaquettes.

For the actual implementation the ring exchange interaction can be written as a sum of commuting four-body interactions

$$\begin{aligned} B_p =& \frac{1}{8}\sum_{j=1}^{8} B_p^{(j)} = \frac{1}{8}(\sigma_1^x\sigma_2^x\sigma_3^x\sigma_4^x + \sigma_1^y\sigma_2^y\sigma_3^y\sigma_4^y + \sigma_1^x\sigma_2^x\sigma_3^y\sigma_4^y + \sigma_1^y\sigma_2^y\sigma_3^x\sigma_4^x \\ & - \sigma_1^x\sigma_2^y\sigma_3^x\sigma_4^y - \sigma_1^y\sigma_2^x\sigma_3^y\sigma_4^x + \sigma_1^x\sigma_2^y\sigma_3^y\sigma_4^x + \sigma_1^y\sigma_2^x\sigma_3^x\sigma_4^y). \end{aligned} \tag{6.22}$$

Likewise, the Rokhsar-Kivelson term can be decomposed into

$$B_p^2 = \frac{1}{8}\sum_{j=1}^{8} N_p^{(j)} = \frac{1}{8}(\sigma_1^0\sigma_2^0\sigma_3^0\sigma_4^0 - \sigma_1^0\sigma_2^0\sigma_3^z\sigma_4^z + \sigma_1^0\sigma_2^z\sigma_3^0\sigma_4^z - \sigma_1^0\sigma_2^z\sigma_3^z\sigma_4^0 - \sigma_1^z\sigma_2^0\sigma_3^0\sigma_4^z + \sigma_1^z\sigma_2^0\sigma_3^z\sigma_4^0 - \sigma_1^z\sigma_2^z\sigma_3^0\sigma_4^0 + \sigma_1^z\sigma_2^z\sigma_3^z\sigma_4^z), \tag{6.23}$$

where σ_i^0 is the identity matrix. Consequently, the coherent time evolution follows again from the general toolbox, while the jump operators for cooling into the ground state at the Rokhsar-Kivelson point effectively cool into the zero eigenvalue eigenstate of the operators

$$\frac{1}{2}[1 - B_p]B_p = \frac{1}{16}\sum_{j=1}^{16} C_p^{(j)} = \frac{1}{16}\left[\sum_{j=1}^{8} B_p^{(j)} - \sum_{j=1}^{8} N_p^{(j)}\right]. \tag{6.24}$$

This can be achieved by replacing the gate U_g with

$$\begin{aligned} U_B &= |0\rangle\langle 0|_c \otimes \mathbf{1} + |1\rangle\langle 1|_c \otimes \exp\left[i\frac{\pi}{2}(1 - B_p)B_p\right] \\ &= \prod_{j=1}^{16} U_c(\pi/2)^{-1} U_j U_c(\pi/2) \exp\left(i\pi/32\sigma_c^z\right) U_c(\pi/2)^{-1} U_j U_c(\pi/2), \end{aligned} \tag{6.25}$$

with $U_j = |0\rangle\langle 0|_c \otimes \mathbf{1} + |1\rangle\langle 1|_c \otimes C_p^{(j)}$. This gate operation leaves states with eigenvalue $0, +1$ of B_p invariant, while the -1 eigenvalue picks up a phase of π. It can be implemented as a product of many-body gates which derive directly from the standard gate U_g with the combination of spin rotations.

The cooling of these jump operators is demonstrated via a numerical simulation for a small system of four unit cells, see Fig. 6.6a. It is important to note that the ground state at the Rokhsar-Kivelson point is not a stabilizer state as the B_p operators acting on different plaquettes do not commute. Hence, the presented method for efficient ground state preparation in interacting spin systems appears to have a much wider range of application, although the exact limitations of the method remains an open question.

Away from the Rokhsar-Kivelson point Although the strongly correlated ground state at the Rokhsar-Kivelson point exhibits interesting properties, the most important aspects of the phase diagram are found for a smaller Rokhsar-Kivelson point with $0 \leq V \leq J$. There, one expects to find a quantum spin liquid with deconfined excitations according to a Coulombic $1/r$

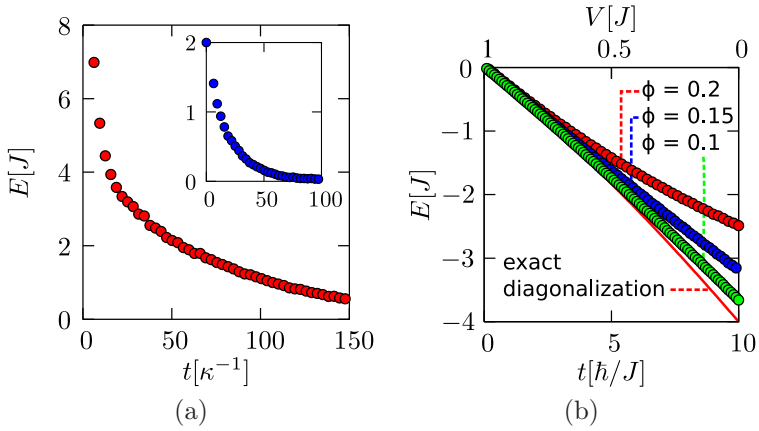

Figure 6.6: Numerical results for dissipative and coherent quantum simulation of a $U(1)$ lattice gauge theory for a system with four unit cells (12 spins). (a) Dissipative cooling into the Rokhsar-Kivelson point with energy $E = 0$. The inset shows the cooling into the equal superposition of all dimer coverings starting from an initial state satisfying the constraint on all octahedra, which can be prepared efficiently using single site addressability. (b) Coherent time evolution from the Rokhsar-Kivelson point with a linear ramp of the Rokhsar-Kivelson term $V(t) = J(1 - tJ/10\hbar)$: the solid line denotes the exact ground state energy, while the dots represent the digital time evolution during an adiabatic ramp for different phases ϕ written during each time step. The difference accounts for errors induced by the Trotter expansion due to the non-commutative terms in the Hamiltonian.

potential [Hermele2004]. As the proposed method does not achieve ground state preparation away from the Rokhsar-Kivelson point, we present a combination of dissipative cooling and the simulation of Hamiltonian dynamics in order to explore this exotic phase.

First, the system is cooled into the ground state at the Rokhsar-Kivelson as described above. Then, the gate sequence for dissipative cooling is replaced by the gate sequence corresponding to the coherent simulation of the Hamiltonian (6.16) at the Rokhsar-Kivelson point with $V = J$. Note that the term proportional to U giving rise to the octahedron constraint does not need to be implemented since the other terms leave the octrahedron constraint invariant. As the operators acting on different plaquettes do not commute it is neccessary to specify an operator splitting method that will give rise to Trotterization errors. We employ a Lie splitting of the form

$$U = \prod_p \exp(-iJB_p\tau)\exp(-iVB_p^2\tau) + O(\tau^2). \tag{6.26}$$

A symmetric Strang operator splitting would give a better accuracy up to $O(\tau^3)$, however, this would require many more gate operations, rendering this splitting inefficient.

Initially, the system is already in an eigenstate of the Hamiltonian, thus its state will remain unchanged. The Hamiltonian is then varied adiabatically according to

$$V(t) = J\left(1 - \frac{tJ}{10\hbar}\right). \tag{6.27}$$

As the Hamiltonian is now time-dependent the time evolution operator has to be time-ordered, i.e.,

$$\begin{aligned} U_V &= \mathcal{T}\exp\left(-\int_t^{t+\tau} V(t')B_p^2\right) = \exp\left[-i\int_t^{t+\tau} V(t')B_p^2\right] + O(\tau^2) \\ &= \exp\left[-iV(t+\tau/2)B_p^2\right] + O(\tau^2). \end{aligned} \tag{6.28}$$

The time evolution of the energy of the system is shown in Fig. 6.6b. Comparison with the ground state energy obtained by exact diagonalization shows that the system remains close to the ground state for small phases ϕ.

6.5 Error analysis

Let us now investigate in detail the effect of imperfect quantum gates on the performance of the coherent and dissipative quantum simulation. In both

cases, the state will have to be described by a density operator ρ, which undergoes an evolution according to the dynamical map

$$\rho' = A\rho A^\dagger + B\rho B^\dagger, \tag{6.29}$$

with appropriate choices for the non-Hermitian operators A and B.

6.5.1 Simulation of Hamiltonian dynamics

Errors in the many-body gate We consider a class of errors in the many-body gate U_g. The imperfect many-body gate operation can be written as

$$\tilde{U}_g = |0\rangle\langle 0|_c \otimes e^{i\phi Q} + |1\rangle\langle 1|_c \otimes A_p, \tag{6.30}$$

where the perfect gate U_g is recovered for $Q \to 0$ and the operator $Q = Q^\dagger$ acts on the system spins surrounding the control atom. This form of the error includes the case of unwanted ensemble-ensemble interaction discussed in Sect. 5.3.2. For the coherent time evolution, the imperfect gate gives rise to a finite amplitude for the control qubit to end up in the state $|1\rangle_c$. Consequently, optical pumping of the control qubit is required to reinitialize the system. Starting in the state $|0\rangle$ of the control atom, the pulse sequence results in

$$|0\rangle \overset{U_{\pi/2}}{\mapsto} \frac{1}{\sqrt{2}}(|0\rangle + |1\rangle) \tag{6.31}$$

$$\overset{\tilde{U}_g}{\mapsto} \frac{1}{\sqrt{2}}(\Theta|0\rangle + A_p|1\rangle) \tag{6.32}$$

$$\overset{U_x}{\mapsto} \frac{1}{\sqrt{2}}(u\Theta|0\rangle + v\Theta|1\rangle + uA_p|1\rangle + vA_p|0\rangle) \tag{6.33}$$

$$\overset{\tilde{U}_g}{\mapsto} \frac{1}{\sqrt{2}}(u\Theta^2|0\rangle + vA_p\Theta|1\rangle + uA_p^2|1\rangle + v\Theta A_p|0\rangle) \tag{6.34}$$

$$\overset{U_{\pi/2}}{\mapsto} \frac{1}{2}(u\Theta^2|0\rangle - u\Theta^2|1\rangle + v\Theta A_p|0\rangle - v\Theta A_p|1\rangle + vA_p\Theta|0\rangle + vA_p\Theta|1\rangle + uA_p^2|0\rangle) \tag{6.35}$$

Here, we have introduced for convenience the gate operation $U_x = R_x^{(c)}(\phi) = R_y^{(c)}(\pi/2)exp(i\phi\sigma_z^{(c)}R_y^{(c)}(-\pi/2)$ and the operator $\Theta = \exp(\mathrm{i}Q/\phi)$ including the error terms (e.g., due to ensemble-ensemble interactions), while A_p represents the desired gate operation. Furthermore, we have used $u = \cos\phi$, $v = \mathrm{i}sin\phi$. Then, the operators characterizing the dynamical map (6.29) can be identified

from the ampltidudes of the internal states of the control atom, i.e.,

$$A = \frac{1}{2}\left[(\Theta^2 + A_p^2)u + (\Theta A_p + A_p\Theta)v\right] \tag{6.36}$$

$$B = \frac{1}{2}\left[(\Theta^2 - A_p^2)u + (\Theta A_p - A_p\Theta)v\right]. \tag{6.37}$$

We now expand the operator $\exp[\mathrm{i}(\phi A_p + Q)]$ up to second order,

$$\exp[\mathrm{i}(\phi A_p + Q)] = 1 + \mathrm{i}\phi A_p + \mathrm{i}Q - \frac{1}{2}\phi^2 - \frac{1}{2}Q^2 - \frac{1}{2}\phi A_p Q - \frac{1}{2}\phi Q A_p, \tag{6.38}$$

since $A_p^2 = 1$. Note that this is identical to the second order expansion for A up to a $Q^2/2$ term, i.e.,

$$A = \exp[\mathrm{i}(\phi A_p + Q)] - \frac{1}{2}Q^2. \tag{6.39}$$

As the operator B apears quadratically in the dynamical map and its zeroth order vanishes, we only need to expand up to the linear term,

$$B = -\mathrm{i}Q. \tag{6.40}$$

Plugging these expansions into the dynamical map (6.29), we arrive at

$$\rho' = \rho + \mathrm{i}\phi\,[H, \rho] - \frac{1}{2}\,[H, [H, \rho]] + Q\rho Q - \frac{1}{2}\left\{Q^2, \rho\right\}, \tag{6.41}$$

with $H = A_p + Q$. The first terms describe unitary evolution, while the last two terms is a Lindblad superoperator giving rise to dissipation.

In the case of ensemble-ensemble interactions the form of Q can be calculated exactly and is given for $N = 4$ ensemble atoms by

$$Q = \frac{35}{96}\frac{\pi}{\phi}\left(\frac{\Omega_p}{\Omega_c}\right)^2\left(6 - 3\sum_{i=1}^{4}\sigma_x^{(i)} + \sum_{i<j}\sigma_x^{(i)}\sigma_x^{(j)}\right). \tag{6.42}$$

Errors in the single qubit gates Let us now assume the many-body gate can be implemented perfectly, however there is an imperfection in the single qubit gates. We investigate errors in the $\pi/2$ gate, i.e,

$$U_{\pi/2} = \Theta U^0_{\pi/2} = \Theta\frac{1}{\sqrt{2}}\begin{pmatrix} 1 & 1 \\ -1 & 1 \end{pmatrix}. \tag{6.43}$$

The most obvious case is when the error Θ represents a rotation about the x axis. Since in both applications of the gate during the pulse sequence $U =$

$U_{\pi/2}U_GU_xU_GU_{\pi/2}$ the control atom is in an x eigenstate, these imperfection will not have any effect on the system at all.

Next, we wil study errors in the z basis, i.e.,

$$\Theta = \begin{pmatrix} \Theta^* & \\ & \Theta \end{pmatrix}. \tag{6.44}$$

Then, we have the pulse sequence

$$\begin{aligned}
|0\rangle &\overset{U^0_{\pi/2}}{\mapsto} \frac{1}{\sqrt{2}}(|0\rangle + |1\rangle) && (6.45)\\
&\overset{\Theta}{\mapsto} \frac{1}{\sqrt{2}}(\Theta^*|0\rangle + \Theta|1\rangle) && (6.46)\\
&\overset{U_G}{\mapsto} \frac{1}{\sqrt{2}}(\Theta^*|0\rangle + \Theta A_p|1\rangle) && (6.47)\\
&\overset{U_x}{\mapsto} \frac{1}{\sqrt{2}}[(\Theta^* u + \Theta v)|0\rangle + (\Theta u A_p + \Theta^* v)|1\rangle] && (6.48)\\
&\overset{U_G}{\mapsto} \frac{1}{\sqrt{2}}[(\Theta^* u + \Theta v)|0\rangle + (\Theta u + \Theta^* v A_p)|1\rangle] && (6.49)\\
&\overset{U^0_{\pi/2}}{\mapsto} \frac{1}{2}[(\Theta^* u + \Theta v A_p + \Theta u + \Theta^* v A_p)|0\rangle \\
&\qquad + (\Theta u + \Theta^* v A_p - \Theta^* u - \Theta v A_p)|1\rangle] && (6.50)\\
&\overset{\Theta}{\mapsto} \frac{1}{2}[(\Theta^{*2} u + v A_p + u + \Theta^{*2} v A_p)|0\rangle \\
&\qquad + (\Theta^2 u + v A_p - u - \Theta^2 v A_p)|1\rangle]. && (6.51)
\end{aligned}$$

In lowest order we obtain for the operators A and B,

$$A \approx 1 - \mathrm{i}Q\frac{\phi^2}{2} + \mathrm{i}\phi A_p - Q^2 + \phi Q A_p \tag{6.52}$$

$$B \approx \mathrm{i}Q. \tag{6.53}$$

After inserting these operators into the dynamical map (6.29) results in

$$\rho' = \rho + \rho + \mathrm{i}\phi\,[A_p, \rho] - \frac{\phi^2}{2}\,[A_p, [A_p, \rho]]\,, \tag{6.54}$$

which describes the perfect evolution of the system without any errors.

Finally, we study errors in the y basis described by

$$\Theta = \begin{pmatrix} x & -y \\ y & x \end{pmatrix}, \tag{6.55}$$

with $x = \cos Q/\phi$ and $y = \sin Q/\phi$. After applying the gate sequence we have

$$|0\rangle \overset{U^0_{\pi/2}}{\mapsto} \frac{1}{\sqrt{2}}(|0\rangle + |1\rangle) \tag{6.56}$$

$$\overset{\Theta}{\mapsto} \frac{1}{\sqrt{2}}[(x-y)|0\rangle + (x+y)|1\rangle)] \tag{6.57}$$

$$\overset{U_G}{\mapsto} \frac{1}{\sqrt{2}}[(x-y)|0\rangle + (x+y)A_p|1\rangle)] \tag{6.58}$$

$$\overset{U_x}{\mapsto} \frac{1}{\sqrt{2}}\{[u(x-y)+v(x+y)A_p]|0\rangle + [u(x+y)A_p + v(x-y)]|1\rangle\} \tag{6.59}$$

$$\overset{U_G}{\mapsto} \frac{1}{\sqrt{2}}\{[u(x-y)+v(x+y)A_p]|0\rangle + [u(x+y)+v(x-y)A_p]|1\rangle\} \tag{6.60}$$

$$\overset{U^0_{\pi/2}}{\mapsto} (ux + vxA_p)|0\rangle + (uy - 2vyA_p)|1\rangle \tag{6.61}$$

$$\overset{\Theta}{\mapsto} (ux^2 - uy^2 + vx^2A_p + vy^2A_p)|0\rangle + 2uxy|1\rangle. \tag{6.62}$$

Expanding the operators A and B gives

$$A \approx 1 - \frac{\phi^2}{2} - 2Q^2 + \mathrm{i}\phi A_p \tag{6.63}$$

$$B \approx 2Q, \tag{6.64}$$

and after insertion into the map (6.29) the Q terms drop out again and we recover the perfect dynamics. Therefore, the setup is robust against single qubit errors up to a second order expansion.

6.5.2 Dissipative state preparation

For discussing the effects of errors on the dissipative time evolution, we use a slightly modified gate sequence, which gives rise to the same quantum master equation, but is conceptually slightly simpler as it involves only a single instance of the many-body gate. The modified gate sequence reads

$$U = U_{Z,i}U_xU_GU_x, \tag{6.65}$$

where U_x is a small rotation around the x axis of the control atom, i.e,

$$U_x = \begin{pmatrix} \cos\phi & \mathrm{i}\sin\phi \\ \mathrm{i}\sin\phi & \cos\phi \end{pmatrix}. \tag{6.66}$$

Errors in the many-body gate For the control atom starting in $|0\rangle$ the sequence results in

$$|0\rangle \overset{U_x}{\mapsto} u|0\rangle + v|1\rangle \tag{6.67}$$

$$\overset{U_G}{\mapsto} u\Theta|0\rangle + vA_p|1\rangle \tag{6.68}$$

$$\overset{U_x}{\mapsto} (u^2\Theta + v^2A_p)|0\rangle + uv(\Theta + A_p)|1\rangle \tag{6.69}$$

$$\overset{U_{Z,i}}{\mapsto} (u^2\Theta + v^2A_p)|0\rangle + uv(\Sigma\Theta + \Sigma A_p)|1\rangle. \tag{6.70}$$

Using the same notation as before, we therefore have when including optical pumping

$$A = u^2\Theta + v^2A_p \approx 1 + \mathrm{i}Q - \frac{Q^2}{2} - \phi^2 - \phi^2A_p \tag{6.71}$$

$$B = uv(\Sigma\Theta + \Sigma A_p) \approx \mathrm{i}\phi\Sigma(1 + A_p). \tag{6.72}$$

Inserting these operators into Eq. (6.29) yields

$$\begin{aligned}\rho' =&\rho + \mathrm{i}\,[Q,\rho] - \frac{1}{2}\,[Q,[Q,\rho]] - 2\phi^2\rho - \phi^2\,\{\Sigma,\rho\}\\ &+ \phi^2\Sigma(1+\Sigma)\rho(1+\Sigma)\Sigma \qquad (6.73)\\ =&\rho + \mathrm{i}\,[Q,\rho] - \frac{1}{2}\,[Q,[Q,\rho]] + \phi^2\Sigma(1+\Sigma)\rho(1+\Sigma)\Sigma\\ &- \frac{\phi^2}{2}\,\{(1+\Sigma)\Sigma\Sigma(1+\Sigma),\rho\}\,. \qquad (6.74)\end{aligned}$$

Therefore, we have a Lindblad form describing the cooling process, while the errors give rise to unwanted Hamiltonian dynamics.

Stationary state The relevant quantity for this master equation is the probability to find the system in a $+1$ eigenstate of A_p, i.e.,

$$P_+ = \mathrm{Tr}\,\{\Pi_+\rho\} = \sum_\lambda \mathrm{Tr}\,\{|+,\lambda\rangle\langle+,\lambda|\rho\}\,. \tag{6.75}$$

Multiplying the master equation (6.74) with Π_+ and performing the trace results in

$$P'_+ = P_+ + \mathrm{i}\mathrm{Tr}\,\{[\Pi_+,Q]\,\rho\} - \frac{1}{2}\mathrm{Tr}\,\{[Q,[Q,\Pi_+]]\,\rho\} + 2\phi^2P_-. \tag{6.76}$$

One immediately sees that we recover the unperturbed master equation for P_+ if $[\Pi_+,Q] = 0$, as it is the case for errors due to ensemble-ensemble interaction. This stems from our series expansion in ϕ in order to derive the

master equation. If Π_+ and Q commute and one wishes to cool the system in a single shot (i.e., $\phi = \pi/4$), one can go back to the exact expressions for A and B (6.71–6.72) and perform only a series expansion in Q. This eventually yields

$$\begin{aligned} P'_+ =& \frac{1}{2}\mathrm{Tr}\left\{\Pi_+\rho\right\} - \frac{1}{4}\mathrm{Tr}\left\{\Pi_+\Theta\Sigma\rho\right\} - \frac{1}{4}\mathrm{Tr}\left\{\Pi_+\Sigma\rho\Theta^\dagger\right\} \\ &+ \frac{1}{4}\mathrm{Tr}\left\{\Pi_+\Sigma(\Theta+\Sigma)\rho(\Theta^\dagger+\Sigma)\Sigma\right\}. \end{aligned} \tag{6.77}$$

Using the operator identities

$$\Pi_+\Sigma = -\Pi_+ \tag{6.78}$$

$$\Pi_-\Sigma = \Pi_- \tag{6.79}$$

$$\mathrm{Tr}\left\{\Pi_+\Sigma\cdot\Sigma\right\} = \mathrm{Tr}\left\{\Pi_-\cdot\right\}, \tag{6.80}$$

and expanding Θ up to second order results in

$$\begin{aligned} P'_+ &= \mathrm{Tr}\left\{\Pi_+\rho\right\} - \frac{1}{4}\mathrm{Tr}\left\{\Pi_+Q^2\rho\right\} + \mathrm{Tr}\left\{\Pi_-\rho\right\} - \frac{1}{4}\mathrm{Tr}\left\{\Pi_-Q^2\rho\right\} \\ &= 1 - \frac{1}{4}\mathrm{Tr}\left\{Q^2\rho\right\}. \end{aligned} \tag{6.81}$$

Let us now look in more detail at the case when $[\Pi_+, Q] \neq 0$. We are interested in the stationary state of the quantum master equation (6.74), given by $\rho' - \rho = 0$. If the errors are small we can assume the stationary state of the master equation being close to $\rho_0 = |+,\lambda\rangle\langle+,\lambda|$. Here, we assume that the system equilibrates into a unique $|+,\lambda\rangle$ eigenstate, e.g., due to the intitial conditions of the system. Then, we write the stationary state including errors as $\rho = \rho_0 + \Delta\rho$. Inserting this into Eq. (6.76) yields

$$\mathrm{i}\mathrm{Tr}\left\{[\Pi_+, Q]\,(\rho_0+\Delta\rho)\right\} - \frac{1}{2}\mathrm{Tr}\left\{[Q,[Q,\Pi_+]]\,(\rho_0+\Delta\rho)\right\} + 2\phi^2\Delta P_-. \tag{6.82}$$

where we have used that ρ_0 is an eigenstate of the dissipator. In lowest order we can ignore contributions in $Q\Delta\rho$ and $Q^2\Delta\rho$. Then one sees that the linear term vanishes and we obtain

$$-\frac{1}{2}\sum_\mu |\langle-,\mu|Q|+,\lambda\rangle|^2 + 2\phi^2\Delta P_- = 0, \tag{6.83}$$

which by using $\Delta P_- = -\Delta P_+$ finally results in

$$P_+ = 1 - \frac{1}{4\phi^2}\sum_\mu |\langle-,\mu|Q|+,\lambda\rangle|^2. \tag{6.84}$$

Other error sources In the following, we investigate how other error sources affect the dynamics of the system. A straightforward situation is that errors do not occur in the $|0\rangle\langle 0|$ branch of the gate, but in the $|1\rangle\langle 1|$ branch, i.e.,

$$U_G = |0\rangle\langle 0| + |1\rangle\langle 1|\Theta A_p. \tag{6.85}$$

Then, we have

$$A = u^2 + v^2\Theta A_p \approx 1 - \phi^2 - \phi^2 A_p \tag{6.86}$$
$$B = uv(\Sigma + \Sigma\Theta A_p) \approx \mathrm{i}\phi\Sigma(1 + A_p). \tag{6.87}$$

Therefore, such an error does not introduce any deviations from the perfect setup in second order.

Next, we study errors in the phase flip gate $U_{Z,i}$,

$$U_{Z,i} = |0\rangle\langle 0|\Theta + |1\rangle\langle 1|\Sigma. \tag{6.88}$$

This results in

$$A = \Theta(u^2 + v^2 A_p) \approx 1 + \mathrm{i}Q - \frac{Q^2}{2} - \phi^2 - \phi^2 A_p \tag{6.89}$$
$$B = uv(\Sigma + \Sigma A_p) \approx \mathrm{i}\phi\Sigma(1 + A_p), \tag{6.90}$$

which up to second order is identical to the expressions given in Eqs. (6.71–6.72). Again, if we instead introduce the errors in the $|1\rangle\langle 1|$ branch as in Eq. (6.85), we end up with no imperfections for the second order result.

A rather different error type occurs when the single qubit gate U_x is implemented imperfectly. Obviously, if we the error can be described by an additional x rotation, the only effect will be a renormalized rate ϕ'^2 in the master equation. However, if we have an error in the z basis of the control atom, i.e.,

$$U_x = \Theta U_x^0 = \begin{pmatrix} \Theta^* & \\ & \Theta \end{pmatrix} \begin{pmatrix} \cos\phi & \mathrm{i}\sin\phi \\ \mathrm{i}\sin\phi & \cos\phi \end{pmatrix}, \tag{6.91}$$

the gate sequence performs the operation

$$|0\rangle \overset{U_x^0}{\mapsto} u|0\rangle + v|1\rangle \tag{6.92}$$
$$\overset{\Theta}{\mapsto} \Theta^* u|0\rangle + \Theta v|1\rangle \tag{6.93}$$
$$\overset{U_G}{\mapsto} \Theta^* u|0\rangle + \Theta v A_p|1\rangle \tag{6.94}$$
$$\overset{U_x^0}{\mapsto} (\Theta^* u^2 + \Theta v^2 A_p)|0\rangle + uv(\Theta^* + \Theta A_p)|1\rangle \tag{6.95}$$
$$\overset{\Theta}{\mapsto} (\Theta^{*2} u^2 + v^2 A_p)|0\rangle + uv(1 + \Theta^2)|1\rangle. \tag{6.96}$$

From this we see that up to second order, we have the same form as in Eq. (6.70). However, since Θ is a scalar instead of an operator, the commutators in the master equation (3.26) vanish, and we recover the result without imperfections.

Similarly, we can study results of errors in the y basis,

$$U_x = \Theta U_x^0 = \begin{pmatrix} x & -y \\ y & x \end{pmatrix} \begin{pmatrix} \cos\phi & \mathrm{i}\sin\phi \\ \mathrm{i}\sin\phi & \cos\phi \end{pmatrix}, \tag{6.97}$$

with $x = \cos Q$ and $y = \sin Q$. Then the gate sequence results in

$$\begin{aligned}
|0\rangle &\overset{U_x^0}{\mapsto} u|0\rangle + v|1\rangle && (6.98)\\
&\overset{\Theta}{\mapsto} (ux - vy)|0\rangle + (vx + uy)|1\rangle && (6.99)\\
&\overset{U_G}{\mapsto} (ux - vy)|0\rangle + (xv + uy)A_p|1\rangle && (6.100)\\
&\overset{U_x^0}{\mapsto} (u^2x - uvy + v^2xA_p + uvyA_p)|0\rangle \\
&\quad +(uvxA_p + u^2yA_p + uvx - v^2y)|1\rangle && (6.101)\\
&\overset{\Theta}{\mapsto} [(ux - vy)^2 + v^2x^2A_p - u^2y^2A_p]|0\rangle + [uvx^2(1 + A_p) \\
&\quad +u^2xy(1 + A_p) + v^2xy(A_p - 1) + uvy^2(A_p - 1)]|1\rangle && (6.102)\\
&\overset{U_{Z,i}}{\mapsto} [(ux - vy)^2 + v^2x^2A_p - u^2y^2A_p]|0\rangle + \Sigma[uvx^2(1 + A_p) \\
&\quad +u^2xy(1 + A_p) + v^2xy(A_p - 1) + uvy^2(A_p - 1)]|1\rangle. && (6.103)
\end{aligned}$$

Expanding the A and B operators yields

$$\begin{aligned}
A &\approx 1 - Q^2 - \phi^2 - 2\mathrm{i}\phi Q - \phi^2 A_p - Q^2 A_p && (6.104)\\
B &\approx \Sigma(Q + \mathrm{i}\phi)(1 + A_p). && (6.105)
\end{aligned}$$

Finally, we arrive at the master equation for the system given by

$$\rho' = \rho + (\phi^2 + Q^2)\Sigma(1 + A_p)\rho(1 + A_p)\Sigma - \frac{1}{2}(\phi^2 + Q^2)\left\{(1 + A_p)\Sigma\Sigma(1 + A_p), \rho\right\}. \tag{6.106}$$

From this we see that we again have only a renormalization of the rate $\phi'^2 = \phi^2 + Q^2$. Again, the system is robust against single qubit errors.

6.6 Experimental parameters

Our setup consists of control and ensemble atoms trapped in large spacing optical lattices [Nelson2007] or magnetic trap arrays [Whitlock2009], so that

single site addressability can be achieved. In order to manipulate ensemble atoms independently, their spacing a must be larger than the wavelength λ_p of the Raman lasers for the many-body gate. Such a spatial resolution can be achieved by tightly focussing the laser beam, by employing superlattice beams for the gate pulses, or sub-wavelength addressing techniques based on magnetic field gradients [Stokes1991] or dark state resonances [Gorshkov2008]. Control and ensemble atoms can be distinguished spectroscopically, e.g., by using different hyperfine states in two state-dependent lattices. A suitable set of parameters is determined by balancing the need for sufficiently large lattice spacing with at the same time strong Rydberg interactions for a fast and high-fidelity many-body gate.

We require the ensemble atoms to be separated by $a = 3.5\lambda_p \approx 1.5\,\mu$m and a fast many-body gate with $T_{\text{gate}} = 1.5\,\mu$s (which is much shorter than decoherence times, e.g., due to radiative decay of the Rydberg states). For ^{87}Rb this is achieved by choosing $\Omega_p = 2\pi \times 67\,$MHz, $\Delta = 2\pi \times 2\,$GHz, $\Omega_c = 2\pi \times 1\,$GHz, an interaction strength of $V = 10\hbar\Omega_c^2/\Delta$, and using the Rydberg states $|r\rangle_c = |59s\rangle$ and $|R\rangle_i = |53s\rangle$, respectively.

An important challenge for an implementation lies with finding a suitable combination of states that produces the desired interaction shift. The description in terms of a van der Waals interaction is only valid if the dipolar coupling is smaller than the Förster defect, otherwise effects of resonant couplings have to be accounted for, see Sect. 2.1.2. Using different Rydberg states in control and ensemble atoms strongly increases the Förster defect while leaving the dipolar matrix elements largely unchanged. For the chosen Rydberg states the corresponding distances are still larger than the LeRoy radius [LeRoy1974], i.e., there is no overlap between the wavefunctions of the atoms. Using s states ensures that the interaction is isotropic. While at these distances there are correction to the van der Waals potentials by the C_8 term in the series expansion, this term is also repulsive and consequently enhances the effective interaction strength. For the chosen parameters, the errors due to ensemble-ensemble interactions result for $N = 4$ atoms in $\phi|Q| = 0.2$.

Further errors can arise from crosstalk between plaquettes being processed in parallel, i.e., when a control atom interacts with ensemble atoms of distant plaquettes. Due to the rapid decay of the van der Waals interaction the residual interaction is reduced by a factor of at least 125 on a square lattice. For $V = 10\hbar\Omega_c^2/\Delta$ the resulting error is of similar size as due to ensemble-ensemble interactions. This error can be further reduced by increasing the number of sublattices z such that only every second or third plaquette is processed in parallel.

Part IV

Conclusion

> Nichts ist getan, wenn noch etwas zu tun übrig ist.
>
> Carl Friedrich Gauß

7 Summary and outlook

This thesis presented a theoretical treatment of the many-body effects present in strongly interacting Rydberg atoms. Previous experimental results on the dipole blockade were successfully successfully explained by a thermodynamic approach, while pointing the way towards the realization of novel quantum phases with these driven systems. Strong interactions between Rydberg atoms were found to be a powerful ressource for the creation of strongly correlated states useful for the controlled coherent manipulation of quantum systems. As a result, the first proposal for a universal quantum simulator under experimentally realistic conditions has been conceived.

In contrast to previous studies of the complex many-body dynamics in driven strongly interacting Rydberg gases, the approach employed in this thesis is based on the observation that the driven system relaxes into a stationary state, which was found to be close to the many-body ground state of the system. This enabled to express the behavior of the system in terms of its thermodynamics phases, where a continuous phase transition from a paramagnetic to a crystalline phase has been discovered. The phase diagram was explored within a refined mean-field approach accounting for the blockade effects, which was found to be in excellent agreement with both numerical simulations and experimental data. Remarkably, this agreement has also been found for one-dimensional systems, which presents strong evidence that the transition between the paramagnetic and the crystalline phase belongs to a novel universality that has not been studied before. This interpretation has also been backed by an approach based on a universal scaling function.

For one-dimensional lattice systems we have found a second quantum melting transition of a commensurate solid, due to the lattice spacing introducing an additional length scale. The phase diagram has been explored by deriving an effective Hamiltonian within perturbation theory, which is valid away from the critical point of the paramagnet-crystal transition.

The ground state phase diagram was found to dominate the dynamical properties of the driven system if the excitation lasers are switched on instantaneously and consequently quenching the system to a non-equilibrium state. Then, the complex relaxation dynamics could be successfully reproduced in terms of a non-Markovian quantum master equation, while the stationary state could be explained within mean-field theory.

The strong interactions found between Rydberg atoms also allow for a systematic creation of correlated states and exotic quantum phases. In particular, it was shown that the combination of strong Rydberg interactions and a two-photon interference effect similar to Electromagnetically Induced Transparancy enables the realization of a many-body quantum gate that is able to entangle a mesoscopic number of qubits in a single step.

We have shown that the many-body can be used as a building block of a quantum simulator with many-body spin interactions, constitutes the first proposal of a universal quantum simulator realizable with current experimental methods. Within this approach, we have also shown that the quantum simuation is not limited to coherent Hamiltonian dynamics. Instead, it was possible to engineer the couplings to an external reservoir such that the stationary state of the arising quantum master equation corresponds to the ground state of a strongly interacting spin model. This dissipative state preparation has successfully been demonstrated for small model systems.

While this thesis presented an exhaustive analysis of the quantum phases in driven strongly interacting Rydberg atoms, the combination of the blockade effects established in this thesis with tailored interaction potentials by weak Rydberg dressing [Honer2010] opens additional possibilities towards the realization of novel quantum phases. Furthermore, the exploration of the possiblities using controlled many-body interactions and dissipative state preparation as provided by the proposed universal quantum simulator has only just begun [Gils2009, Augusiak2010].

Part V

Appendices

A Weighted sums of binomial coefficients

Let x, α be any complex numbers with $|x| < 1$.

Theorem A.1.

$$\sum_{k=0}^{\infty} \binom{\alpha}{k} k = \alpha 2^{\alpha-1}. \tag{A.1}$$

Proof. The binomial theorem allows to cast a weighted sum of the binomial coefficients into a closed form,

$$(1+x)^{\alpha} = \sum_{k=0}^{\infty} \binom{\alpha}{k} x^k. \tag{A.2}$$

Differentiating with respect to x and evaluating the equation at $x = 1$ completes the proof. □

Corollary A.2. *Differentiating multiple times with respect to x and using theorem A.1 consecutively yields*

$$\sum_{k=0}^{\infty} \binom{\alpha}{k} k^2 = \alpha(\alpha+1)2^{\alpha-2} \tag{A.3}$$

$$\sum_{k=0}^{\infty} \binom{\alpha}{k} k^3 = \alpha^2(\alpha+3)2^{\alpha-3} \tag{A.4}$$

$$\sum_{k=0}^{\infty} \binom{\alpha}{k} k^4 = \alpha(\alpha+1)(\alpha^2+5\alpha-2)2^{\alpha-4}. \tag{A.5}$$

B German Summary

Wissenschaftlicher Hintergrund

In der Vergangenheit hat der Fortschritt bei der Kontrolle ultrakalter Rydberg-Gase dazu geführt, dass Experimente im Regime starker Wechselwirkungen durchgeführt werden können [Heidemann2007, Younge2009, Pritchard2009, Schempp2010]. Von besonderem Interesse ist dabei die Dipol-Blockade, welche besagt, dass zwei eng benachbarte Atome nicht gleichzeitig angeregt werden können, da die starke Wechselwirkung zwischen den Rydberg-Zuständen den zweifach angeregten Zustand aus der Resonanz schiebt [Jaksch2000]. Als die ersten Experimente zur Dipol-Blockade durchgeführt wurden, war das theoretische Verständnis der starken Vielteilchen-Effekte beschränkt auf Simulationen von kleinen Systemen [Robicheaux2005b] und phänomenologische Skalierungsmodelle [Heidemann2007].

Quantenkritisches Verhalten in stark wechselwirkenden Rydberg-Gasen

Der erste Teil der Dissertation präsentiert eine thermodynamische Interpretation der Anregungssdynamik in stark wechselwirkenden Rydberg-Gasen. Experimente zeigen, dass eine resonante Anregung von Rydberg-Zuständen aus dem atomaren Grundzustand zu einem Gleichgewichtszustand führt. Durch eine Abbildung auf ein wechselwirkendes Spin-Modell kann gezeigt werden, dass dieser Gleichgewichtszustand im wesentlichen durch die Eigenschaften des Grundzustands bestimmt ist. Für verschwindende Rabi-Frequenz Ω wird das Spin-Modell klassisch und kann exakt gelöst werden. Daraus ergibt sich, dass der Grundzustand einen Phasenübergang zweiter Ordnung in der Verstimmung von der Resonanz aufweist und von einem Paramagneten zu einem Kristall übergeht [Weimer2008a]. Die kritischen Eigenschaften dieses Übergangs lassen sich mit einem Mean-Field-Ansatz beschreiben, wobei eine explizite Form der Paarkorrelationsfunktion gewählt wird, um die starken Blockade-Effekte zu berücksichtigen. Die so erhaltenen kritischen Exponenten sind in exzellenter Übereinstimmung sowohl mit numerischen Simulationen als auch

mit experimentellen Ergebnissen [Löw2009]. Überraschenderweise gilt dies auch in eindimensionalen Systemen, folglich ist die langreichweitige Wechselwirkung auch in diesem Fall hinreichend, um die Gültigkeit von Mean-Field-Resultaten herzustellen. Für die numerischen Simulationen lässt sich der Blockade-Effekt ausnutzen, um die Dimension des Hilbertraum drastisch zu verkleinern, wodurch Simulationen mit bis zu 100 Atomen möglich sind. Diese Technik kann auch verwendet werden, um die Dephasierungseigenschaften durch Rydberg-Wechselwirkungen in einer Rotary-Echo-Sequenz zu untersuchen [Raitzsch2009].

Um die volle Zeitentwicklung der Anregung zu beschreiben, wird die Dynamik als Relaxationsprozess hin zu dem durch Mean-Field-Theorie beschriebenen Gleichgewichtszustand interpretiert. Dabei wird ein einzelner Spin betrachtet, der von einem Bad der restlichen Spins umgeben ist. Durch Anwendung einer Projektionsoperator-Technik für die Behandlung der quadratischen Fluktuationen um das Mean-Field lässt sich eine nicht-markovsche Mastergleichung herleiten, deren Lösung exzellente Übereinstimmung mit der vollen Numerik zeigt.

Ein Quantensimulator mit Rydberg-Atomen

Der zweite Teil der Dissertation behandelt die systematische Erzeugung von stark korrelierten Zuständen durch die starken Wechselwirkungen zwischen Rydberg-Atomen. Die Kombination aus diesen Wechselwirkungen mit der relativ langen Lebensdauer macht Rydberg-Atome zu einem geeigneten Kandidaten für skalierbare Quanteninformationsverarbeitung. Um dies zu erreichen, wird ein mesoskopisches Controlled-NOT^N-Gatter vorgeschlagen, welches N Atome in einem Zeitschritt verschränkt [Müller2009]. Das Gatter benutzt einen Interferenzeffekt zwischen zwei Photonen, welcher der elektomagnetisch induzierten Transparenz ähnelt. Ohne Rydberg-Wechselwirkungen (Kontroll-Atom in $|0\rangle$) folgt das System adiabatisch einem Dunkelzustand mit Energie Null, wodurch der Zustand am Ende der Laserpuls-Sequenz unverändert bleibt. Im Falle vorhandener Rydberg-Wechselwirkungen (Kontroll-Atom in $|1\rangle$) ist diese Zweiphotonen-Resonanz aufgehoben und das System folgt nicht mehr dem Dunkelzustand: die Target-Atome werden von einem Hyperfein-Zustand in einen anderen überführt, wodurch das Controlled-NOT^N-Gatter realisiert wird.

Durch Verwendung des mesoskopischen Rydberg-Gatters kann ein universeller Quantensimulator für N-Teilchen-Wechselwirkungen aufgebaut werden [Weimer2010]. Dafür werden die Eigenzustände der simulierten Wechselwirkung durch das Gatter auf die internen Zustände des zusätzlichen Kontroll-

Atoms abgebildet. Nach einer Phasenrotation des Kontroll-Atoms und Ausführung der inversen Abbildung liegt eine digitale Simulation der Vielteilchen-Wechselwirkung vor. Zusätzlich erlaubt dieser Ansatz ein direktes Kühlen in den Grundzustand der simulierten Wechselwirkung. Dies wird erreicht, indem die Phasenrotation durch einen kontrollierten Spin-Flip in den Target-Atomen ersetzt wird, d.h. der vom Zustand des Kontroll-Atoms abhängt. Reinitialisierung des Kontroll-Atoms durch optisches Pumpen führt zu einer Kühldynamik, die durch eine Mastergleichung beschrieben werden kann.

Mit diesen Bausteinen ist es möglich, das System auf Atome in einem optischen Gitter hochzuskalieren. Beispiele, in denen Kühlung in den Grundzustand erfolgreich gezeigt wurde, sind Kitaevs Toric Code [Kitaev2003], der anyonische Anregungen besitzt, sowie eine $U(1)$-Gittereichtheorie [Hermele2004], in der ein Confinement-Deconfinement-Phasenübergang auftritt, der durch adiabatisches Ändern des simulierten Hamiltonians untersucht werden kann.

List of Symbols

a	Lattice spacing
a_R	Spacing of Rydberg excitations
β	Critical exponent
C_p	Coefficient of generalized power-law interaction
d	Spatial dimension
Δ	Detuning
δ	Critical exponent
$\|e\rangle$	Internal excited state
E	Energy
f_R	Rydberg fraction
$\|g\rangle$	Internal ground state
g_2	Pair-correlation function
γ	Decay rate
$\mathcal{H}$	Hilbert space
H	Hamiltonian
h	Effective magnetic field
$\hbar$	Planck's constant
H_{eff}	Effective Hamiltonian
J	Hopping matrix element
k_B	Boltzmann's constant
$\mathcal{L}$	Liouvillian
μ	Chemical potential
N	Particle number
n	Density
n^*	Effective quantum number
$\mathcal{P}$	Projection superoperator
p	Exponent of power-law interaction
P_{ee}	Projection onto excited state
$\mathbf{r}$	Position
r	Distance
r_b	Two-atom blockade radius
ρ	Density operator
ρ_i	Reduced density operator of subsystem i
σ_α	Pauli matrix

T	Temperature
U	On-site interaction
V	Interaction potential
v	Visibility
Ω	Rabi frequency
ω	Angular frequency
ξ	Correlation length
ζ	Riemann zeta function

Bibliography

[Aguado2008] M. Aguado, G. K. Brennen, F. Verstraete, and J. I. Cirac. Creation, Manipulation, and Detection of Abelian and Non-Abelian Anyons in Optical Lattices. *Phys. Rev. Lett.*, **101**, 260501 (2008).

[Alicki2009] R. Alicki, M. Fannes, and M. Horodecki. On thermalization in Kitaev's 2D model. *J. Phys. A*, **42**, 065303 (2009).

[Altman2004] E. Altman, E. Demler, and M. D. Lukin. Probing many-body states of ultracold atoms via noise correlations. *Phys. Rev. A*, **70**, 013603 (2004).

[Amthor2007] T. Amthor, M. Reetz-Lamour, S. Westermann, J. Denskat, and M. Weidemüller. Mechanical Effect of van der Waals Interactions Observed in Real Time in an Ultracold Rydberg Gas. *Phys. Rev. Lett.*, **98**, 023004 (2007).

[Anderlini2007] M. Anderlini, P. J. Lee, B. L. Brown, J. Sebby-Strabley, W. D. Phillips, and J. V. Porto. Controlled exchange interaction between pairs of neutral atoms in an optical lattice. *Nature*, **448**, 452 (2007).

[Anderson1998] W. R. Anderson, J. R. Veale, and T. F. Gallagher. Resonant Dipole-Dipole Energy Transfer in a Nearly Frozen Rydberg Gas. *Phys. Rev. Lett.*, **80**, 249 (1998).

[Ates2007] C. Ates, T. Pohl, T. Pattard, and J. M. Rost. Many-body theory of excitation dynamics in an ultracold Rydberg gas. *Phys. Rev. A*, **76**, 013413 (2007).

[Augusiak2010] R. Augusiak, F. M. Cucchietti, F. Haake, and M. Lewenstein. Quantum kinetic Ising models. *New Journal of Physics*, **12**, 025021 (2010).

[Bak1982] P. Bak and R. Bruinsma. One-Dimensional Ising Model and the Complete Devil's Staircase. *Phys. Rev. Lett.*, **49**, 249 (1982).

[Bloch2008] I. Bloch, J. Dalibard, and W. Zwerger. Many-body physics with ultracold gases. *Rev. Mod. Phys.*, **80**, 885 (2008).

[Bombin2006] H. Bombin and M. A. Martin-Delgado. Topological Quantum Distillation. *Phys. Rev. Lett.*, **97**, 180501 (2006).

[Brekke2008] E. Brekke, J. O. Day, and T. G. Walker. Four-wave mixing in ultracold atoms using intermediate Rydberg states. *Phys. Rev. A*, **78**, 063830 (2008).

[Breuer2002] H.-P. Breuer and F. Petruccione. *The Theory of Open Quantum Systems* (Oxford University Press, Oxford, 2002).

[Breuer2007] H.-P. Breuer. Non-Markovian generalization of the Lindblad theory of open quantum systems. *Phys. Rev. A*, **75**, 022103 (2007).

[Brion2007] E. Brion, K. Mølmer, and M. Saffman. Quantum Computing with Collective Ensembles of Multilevel Systems. *Phys. Rev. Lett.*, **99**, 260501 (2007).

[Dennis2002] E. Dennis, A. Kitaev, A. Landahl, and J. Preskill. Topological quantum memory. *J. Math. Phys.*, **43**, 4452 (2002).

[Diehl2008] S. Diehl, A. Micheli, A. Kantian, B. Kraus, H. P. Büchler, and P. Zoller. Quantum states and phases in driven open quantum systems with cold atoms. *Nature Phys.*, **4**, 878 (2008).

[Duan2003] L.-M. Duan, E. Demler, and M. D. Lukin. Controlling Spin Exchange Interactions of Ultracold Atoms in Optical Lattices. *Phys. Rev. Lett.*, **91**, 090402 (2003).

[Feynman1982] R. P. Feynman. Simulating physics with computers. *Int. J. Theo. Phys.*, **21**, 467 (1982).

[Fisher1989] M. P. A. Fisher, P. B. Weichman, G. Grinstein, and D. S. Fisher. Boson localization and the superfluid-insulator transition. *Phys. Rev. B*, **40**, 546 (1989).

[Fisher1998] M. E. Fisher. Renormalization group theory: Its basis and formulation in statistical physics. *Rev. Mod. Phys.*, **70**, 653 (1998).

[Fleischhauer2005] M. Fleischhauer, A. Imamoglu, and J. P. Marangos. Electromagnetically induced transparency: Optics in coherent media. *Rev. Mod. Phys.*, **77**, 633 (2005).

[Fölling2005] S. Fölling, F. Gerbier, A. Widera, O. Mandel, T. Gericke, and I. Bloch. Spatial quantum noise interferometry in expanding ultracold atom clouds. *Nature*, **434**, 481 (2005).

[Gallagher1994] T. F. Gallagher. *Rydberg Atoms* (Cambridge University Press, Cambridge, 1994).

[Gils2009] C. Gils, S. Trebst, A. Kitaev, A. W. W. Ludwig, M. Troyer, and Z. Wang. Topology-driven quantum phase transitions in time-reversal-invariant anyonic quantum liquids. *Nat Phys*, **5**, 834 (2009).

[Goldenfeld1992] N. Goldenfeld. *Lectures on Phase Transitions and the Renormalization Group* (Perseus Books, Reading, 1992).

[Gorshkov2008] A. V. Gorshkov, L. Jiang, M. Greiner, P. Zoller, and M. D. Lukin. Coherent Quantum Optical Control with Subwavelength Resolution. *Phys. Rev. Lett.*, **100**, 093005 (2008).

[Gottesman1996] D. Gottesman. Class of quantum error-correcting codes saturating the quantum Hamming bound. *Phys. Rev. A*, **54**, 1862 (1996).

[Greiner2002] M. Greiner, O. Mandel, T. W. Esslinger, T. Hänsch, and I. Bloch. Quantum phase transition from a superfluid to a Mott insulator in a gas of ultracold atoms. *Nature*, **415**, 39 (2002).

[Heidemann2007] R. Heidemann, U. Raitzsch, V. Bendkowsky, B. Butscher, R. Löw, L. Santos, and T. Pfau. Evidence for coherent collective Rydberg excitation in the strong blockade regime. *Phys. Rev. Lett.*, **99**, 163601 (2007).

[Heidemann2008a] R. Heidemann. *Rydberg Excitation of Bose-Einstein Condensates: Coherent Collective Dynamics*. Ph.D. thesis, University of Stuttgart (2008).

[Heidemann2008b] R. Heidemann, U. Raitzsch, V. Bendkowsky, B. Butscher, R. Low, and T. Pfau. Rydberg Excitation of Bose-Einstein Condensates. *Phys. Rev. Lett.*, **100**, 033601 (2008).

[Hermele2004] M. Hermele, M. P. A. Fisher, and L. Balents. Pyrochlore photons: The $U(1)$ spin liquid in a $S = \frac{1}{2}$ three-dimensional frustrated magnet. *Phys. Rev. B*, **69**, 064404 (2004).

[Honer2010] J. Honer, H. Weimer, T. Pfau, and H. P. Büchler. Collective many-body interaction in Rydberg dressed atoms. *arXiv:1004.2499* (2010).

[Huang1987] K. Huang. *Statistical Mechanics* (John Wiley and Sons, New York, 1987).

[Jackeli2009] G. Jackeli and G. Khaliullin. Mott Insulators in the Strong Spin-Orbit Coupling Limit: From Heisenberg to a Quantum Compass and Kitaev Models. *Phys. Rev. Lett.*, **102**, 017205 (2009).

[Jaksch1998] D. Jaksch, C. Bruder, J. I. Cirac, C. W. Gardiner, and P. Zoller. Cold Bosonic Atoms in Optical Lattices. *Phys. Rev. Lett.*, **81**, 3108 (1998).

[Jaksch2000] D. Jaksch, J. I. Cirac, P. Zoller, S. L. Rolston, R. Côté, and M. D. Lukin. Fast Quantum Gates for Neutral Atoms. *Phys. Rev. Lett.*, **85**, 2208 (2000).

[Johnson2008] P. R. Johnson, E. Tiesinga, J. V. Porto, and C. J. Williams. Effective three-body interactions and decoherence of coherent atom states in optical lattices. *arXiv:0812.1387* (2008).

[Kitaev2003] A. Y. Kitaev. Fault-tolerant quantum computation by anyons. *Ann. Phys*, **303**, 2 (2003).

[Kitaev2006] A. Y. Kitaev. Anyons in an exactly solved model and beyond. *Ann. Phys*, **321**, 2 (2006).

[Klein1974] D. J. Klein. Degenerate perturbation theory. *J. Chem. Phys.*, **61**, 786 (1974).

[Kleinert1989] H. Kleinert. *Stresses and Defects: Differential Geometry, Crystal Melting*, volume II of *Gauge fields in condensed matter* (World Scientific, Singapore, 1989).

[Kogut1979] J. B. Kogut. An introduction to lattice gauge theory and spin systems. *Rev. Mod. Phys.*, **51**, 659 (1979).

[Kosterlitz1973] J. M. Kosterlitz and D. J. Thouless. Ordering, metastability and phase transitions in two-dimensional systems. *J. Phys. C*, **6**, 1181 (1973).

[Kraus2008] B. Kraus, H. P. Büchler, S. Diehl, A. Kantian, A. Micheli, and P. Zoller. Preparation of entangled states by quantum Markov processes. *Phys. Rev. A*, **78**, 042307 (2008).

[Kübler2010] H. Kübler, J. P. Shaffer, T. Baluktsian, R. Löw, and T. Pfau. Coherent excitation of Rydberg atoms in micrometre-sized atomic vapour cells. *Nature Photon.*, **4**, 112 (2010).

[LeRoy1974] R. J. LeRoy. Long-Range Potential Coefficients From RKR Turning Points: C_6 and C_8 for $B(3\Pi^+_{Ou})$-State Cl_2, Br_2, and I_2. *Can. J. Phys.*, **52**, 246 (1974).

[Levin2005] M. Levin and X.-G. Wen. Colloquium: Photons and electrons as emergent phenomena. *Rev. Mod. Phys.*, **77**, 871 (2005).

[Lloyd1996] S. Lloyd. Universal Quantum Simulators. *Science*, **273**, 1073 (1996).

[Löw2009] R. Löw, H. Weimer, U. Krohn, R. Heidemann, V. Bendkowsky, B. Butscher, H. P. Büchler, and T. Pfau. Universal scaling in a strongly interacting Rydberg gas. *Phys Rev. A*, **80**, 033422 (2009).

[Lukin2001] M. D. Lukin, M. Fleischhauer, R. Côté, L. M. Duan, D. Jaksch, J. I. Cirac, and P. Zoller. Dipole Blockade and Quantum Information Processing in Mesoscopic Atomic Ensembles. *Phys. Rev. Lett.*, **87**, 037901 (2001).

[Merzbacher1970] E. Merzbacher. *Quantum Mechanics* (Wiley, New York, 1970).

[Müller2009] M. Müller, I. Lesanovsky, H. Weimer, H. P. Büchler, and P. Zoller. Mesoscopic Rydberg gate based on electromagnetically induced transparency. *Phys. Rev. Lett.*, **102**, 170502 (2009).

[Nelson2007] K. D. Nelson, X. Li, and D. S. Weiss. Imaging single atoms in a three dimensional array. *Nature Phys.*, **3**, 556 (2007).

[Ni2008] K.-K. Ni, S. Ospelkaus, M. H. G. de Miranda, A. Pe'er, B. Neyenhuis, J. J. Zirbel, S. Kotochigova, P. S. Julienne, D. S. Jin, and J. Ye. A High Phase-Space-Density Gas of Polar Molecules. *Science*, **322**, 231 (2008).

[Nielsen2000] M. A. Nielsen and I. L. Chuang. *Quantum computation and quantum information* (Cambridge University Press, Cambridge, 2000).

[Olmos2009] B. Olmos, R. González-Férez, and I. Lesanovsky. Collective Rydberg excitations of an atomic gas confined in a ring lattice. *Phys. Rev. A*, **79**, 043419 (2009).

[Ovchinnikov2003] A. A. Ovchinnikov, D. V. Dmitriev, V. Y. Krivnov, and V. O. Cheranovskii. Antiferromagnetic Ising chain in a mixed transverse and longitudinal magnetic field. *Phys. Rev. B*, **68**, 214406 (2003).

[Pritchard2009] J. D. Pritchard, A. Gauguet, K. J. Weatherill, M. P. A. Jones, and C. S. Adams. Cooperative optical non-linearity due to dipolar interactions in an ultra-cold Rydberg ensemble. *arXiv:0911.3523* (2009).

[Qaqish2003] B. F. Qaqish. A family of multivariate binary distributions for simulating correlated binary variables with specified marginal means and correlations. *Biometrika*, **90**, 455 (2003).

[Raitzsch2008] U. Raitzsch, V. Bendkowsky, R. Heidemann, B. Butscher, R. Löw, and T. Pfau. Echo Experiments in a Strongly Interacting Rydberg Gas. *Phys. Rev. Lett.*, **100**, 013002 (2008).

[Raitzsch2009] U. Raitzsch, R. Heidemann, H. Weimer, B. Butscher, P. Kollmann, R. Löw, H. P. Büchler, and T. Pfau. Investigation of dephasing rates in an interacting Rydberg gas. *New J. Phys.*, **11**, 055014 (2009).

[Robicheaux2005a] F. Robicheaux. Ionization due to the interaction between two Rydberg atoms. *J. Phys. B*, **38**, S333 (2005).

[Robicheaux2005b] F. Robicheaux and J. V. Hernández. Many-body wave function in a dipole blockade configuration. *Phys. Rev. A*, **72**, 063403 (2005).

[Rokhsar1988] D. Rokhsar and S. Kivelson. Superconductivity and the Quantum Hard-Core Dimer Gas. *Phys. Rev. Lett.*, **61**, 2376 (1988).

[Sachdev1999] S. Sachdev. *Quantum Phase Transitions* (Cambridge University Press, Cambridge, 1999).

[Saffmanto be published] M. Saffman, T. G. Walker, and K. Mølmer. Quantum information with Rydberg atoms. *Rev. Mod. Phys.* (to be published). ArXiv:0909.4777.

[Schachenmayer2010] J. Schachenmayer, I. Lesanovsky, A. Micheli, and A. J. Daley. Dynamical crystal creation with polar molecules or Rydberg atoms in optical lattices. *arXiv:1003.5858* (2010).

[Schempp2010] H. Schempp, G. Günter, C. S. Hofmann, C. Giese, S. D. Saliba, B. D. DePaola, T. Amthor, M. Weidemüller, S. Sevinçli, and T. Pohl. Coherent Population Trapping with Controlled Interparticle Interactions. *Phys. Rev. Lett.*, **104**, 173602 (2010).

[Shor1995] P. W. Shor. Scheme for reducing decoherence in quantum computer memory. *Phys. Rev. A*, **52**, R2493 (1995).

[Singer2004] K. Singer, M. Reetz-Lamour, T. Amthor, L. G. Marcassa, and M. Weidemüller. Suppression of Excitation and Spectral Broadening Induced by Interactions in a Cold Gas of Rydberg Atoms. *Phys. Rev. Lett.*, **93**, 163001 (2004).

[Singer2005] K. Singer, J. Stanojevic, M. Weidemüller, and R. Côté. Long-range interactions between alkali Rydberg atom pairs correlated to the ns ns, np np and nd nd asymptotes. *J. Phys. B*, **38**, S295 (2005).

[Sørensen1999] A. Sørensen and K. Mølmer. Spin-Spin Interaction and Spin Squeezing in an Optical Lattice. *Phys. Rev. Lett.*, **83**, 2274 (1999).

[Stanley1996] M. H. R. Stanley, L. A. N. Amaral, S. V. Buldyrev, S. Havlin, H. Leschhorn, P. Maass, M. A. Salinger, and H. E. Stanley. Scaling behaviour in the growth of companies. *Nature*, **379**, 804 (1996).

[Stokes1991] K. D. Stokes, C. Schnurr, J. R. Gardner, M. Marable, G. R. Welch, and J. E. Thomas. Precision position measurement of moving atoms using optical fields. *Phys. Rev. Lett.*, **67**, 1997 (1991).

[Stuhler2005] J. Stuhler, A. Griesmaier, T. Koch, M. Fattori, T. Pfau, S. Giovanazzi, P. Pedri, and L. Santos. Observation of Dipole-Dipole Interaction in a Degenerate Quantum Gas. *Phys. Rev. Lett.*, **95**, 150406 (2005).

[Tong2004] D. Tong, S. M. Farooqi, J. Stanojevic, S. Krishnan, Y. P. Zhang, R. Côté, E. E. Eyler, and P. L. Gould. Local Blockade of Rydberg Excitation in an Ultracold Gas. *Phys. Rev. Lett.*, **93**, 063001 (2004).

[Trotzky2008] S. Trotzky, P. Cheinet, S. Folling, M. Feld, U. Schnorrberger, A. M. Rey, A. Polkovnikov, E. A. Demler, M. D. Lukin, and I. Bloch. Time-Resolved Observation and Control of Superexchange Interactions with Ultracold Atoms in Optical Lattices. *Science*, **319**, 295 (2008).

[Vidal2009] J. Vidal, S. Dusuel, and K. P. Schmidt. Low-energy effective theory of the toric code model in a parallel magnetic field. *Phys. Rev. B*, **79**, 033109 (2009).

[Vogt2006] T. Vogt, M. Viteau, J. Zhao, A. Chotia, D. Comparat, and P. Pillet. Dipole Blockade at Förster Resonances in High Resolution Laser Excitation of Rydberg States of Cesium Atoms. *Phys. Rev. Lett.*, **97**, 083003 (2006).

[Walker2008] T. G. Walker and M. Saffman. Consequences of Zeeman degeneracy for the van der Waals blockade between Rydberg atoms. *Phys. Rev. A*, **77**, 032723 (2008).

[Walls1994] D. F. Walls and G. J. Milburn. *Quantum Optics* (Springer, Berlin, 1994).

[Weimer2008a] H. Weimer, R. Löw, T. Pfau, and H. P. Büchler. Quantum critical behavior in strongly interacting Rydberg gases. *Phys. Rev. Lett.*, **101**, 250601 (2008).

[Weimer2008b] H. Weimer, M. Michel, J. Gemmer, and G. Mahler. Transport in anisotropic model systems analyzed by a correlated projection superoperator technique. *Phys. Rev. E*, **77**, 011118 (2008).

[Weimer2010] H. Weimer, M. Müller, I. Lesanovsky, P. Zoller, and H. P. Büchler. A Rydberg quantum simulator. *Nature Phys.*, **6**, 382 (2010).

[West2004] G. B. West and J. H. Brown. Life's Universal Scaling Laws. *Phys. Today*, **57**, 36 (2004).

[Whitlock2009] S. Whitlock, R. Gerritsma, T. Fernholz, and R. J. C. Spreeuw. Two-dimensional array of microtraps with atomic shift register on a chip. *New J. Phys.*, **11**, 023021 (2009).

[Younge2009] K. C. Younge, A. Reinhard, T. Pohl, P. R. Berman, and G. Raithel. Mesoscopic Rydberg ensembles: Beyond the pairwise-interaction approximation. *Phys. Rev. A*, **79**, 043420 (2009).

Acknowledgments